YTU FEN EDEBİYAT FAKÜLTESİ

2023-2024 Spring Semester Physics Department

Innovative Approaches and Recycling Technologies in the Nuclear Fuel Cycle

ŞEVİN ULUSOY

PROF. DR. AYBEN KARASU UYSAL

ABSTRACT

This study examines the nuclear waste cycle and innovative approaches to recycling. It considers the challenges of the current fuel cycle and the potential of innovative recycling technologies. The advantages and disadvantages of these approaches are discussed, and their environmental and economic impacts are analysed. The recycling technologies developed for the waste of uranium and plutonium, which are the main nuclear fuels used, are also discussed. The importance of recycling transuranium elements is investigated, along with the potential for recycling them. The potential risks associated with the use of plutonium in nuclear weapons have been highlighted, along with the importance of rigorous inspections for nuclear safety. The potential benefits of meeting the world's energy demand through nuclear energy rather than through existing energy production sources have been explored.
.

INTRODUCTION

Nuclear power has been a vital component of the global energy system since its inception in the mid-20th century, providing a substantial portion of low-carbon electricity. Despite its benefits, nuclear power also presents significant challenges, including the generation of high-level radioactive waste that requires careful management and disposal. Traditional once-through fuel cycles, commonly used in the United States and other countries, result in the direct disposal of spent nuclear fuel without reprocessing, leading to significant environmental and safety concerns.

Reprocessing of spent nuclear fuel has emerged as a promising solution to mitigate these concerns by recycling valuable fissile materials, thereby reducing the volume and toxicity of nuclear waste. The PUREX process, developed in the 1960s, remains the predominant method for reprocessing spent nuclear fuel. This process involves the separation of uranium and plutonium from fission products and minor actinides, significantly reducing the radiotoxicity and heat load of the remaining waste. However, PUREX and other traditional reprocessing techniques face challenges such as proliferation risks and high costs.

Advanced reprocessing technologies have been developed to address these issues. For instance, the DIAMEX and SANEX processes are designed to selectively separate minor actinides and lanthanides from high-level liquid waste, further reducing long-term radiotoxicity and enhancing proliferation resistance. Similarly, pyrochemical processes, which involve the use of molten salts and metals at high temperatures, offer benefits such as compact plant design, shorter cooling periods for spent fuel, and reduced transuranic waste.

The role of advanced nuclear reactors and innovative fuel cycles is also critical in achieving a sustainable nuclear energy system. Advanced reactors, including fast reactors and accelerator-driven systems, are capable of utilizing reprocessed fuel more efficiently and with greater safety. These reactors, combined with advanced reprocessing techniques, form a synergistic approach to managing nuclear waste, enhancing resource utilization, and reducing environmental impact.

Transformation Process

$$UO_3 + 2H_2 \rightarrow 3UO_2 + 2H_2O \qquad \Delta H = -109 \frac{kJ}{mol} \qquad \text{(Equ.1)}$$

or

$$UO_3 + H_2 \rightarrow UO_2 + H_2O \qquad \Delta H = -109 \frac{kJ}{mol} \qquad \text{(Equ.2)}$$

This reduced oxide is then reacted with gaseous hydrogen fluoride (HF) to form uranium tetrafluoride (UF_4).

$$UO_2 + 4HF \rightarrow UF_4 + 2H_2O \qquad \Delta H = -176 \frac{kJ}{mol} \qquad \text{(Equ.3)}$$

It is then fed with gaseous fluorine in the reactor or flame tower to produce UF6.

$$UF_4 + F_2 \rightarrow UF_6 \qquad \qquad \text{(Equ.4)}$$

RESULT & CONCLUSION

Traditional methods such as PUREX, although widely used, pose significant proliferation risks and environmental concerns. In contrast, advanced reprocessing methods such as DIAMEX, SANEX and pyroprocessing offer promising solutions to mitigate these problems by improving safety, reducing waste volumes and improving resource utilisation.

The integration of advanced nuclear reactors with innovative fuel cycles represents a major step towards a sustainable and efficient nuclear energy system. These reactors, including fast reactors and accelerator-driven systems, can make more effective use of reprocessed fuel, thereby reducing the environmental impact and increasing the sustainability of nuclear power. In addition, the development of partitioning and transmutation (P&T) technologies for nuclear waste has the potential to modify the radioactive properties of waste, thereby minimising its long-term hazard.

Our analysis also underlines the critical role of nuclear power in meeting future global energy needs while tackling climate change. With its low carbon emissions, nuclear power is positioned as an essential component of the energy mix needed to meet global decarbonisation targets. However, the transition to a more nuclear-dependent energy system needs to be carefully managed to address public concerns and ensure safety and security.

In conclusion, innovative recycling technologies and advanced reactors are key to overcoming the challenges posed by traditional nuclear fuel cycles. By continuing to invest in and develop these technologies, we can ensure that nuclear energy remains a safe, reliable and environmentally friendly source of energy for the future.
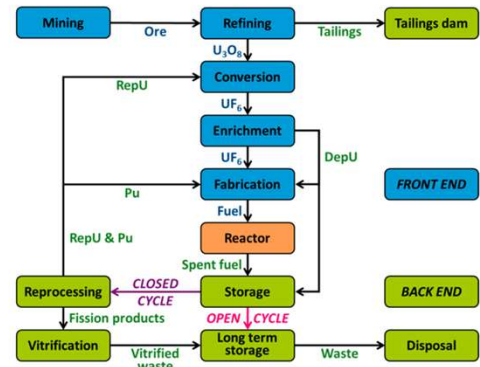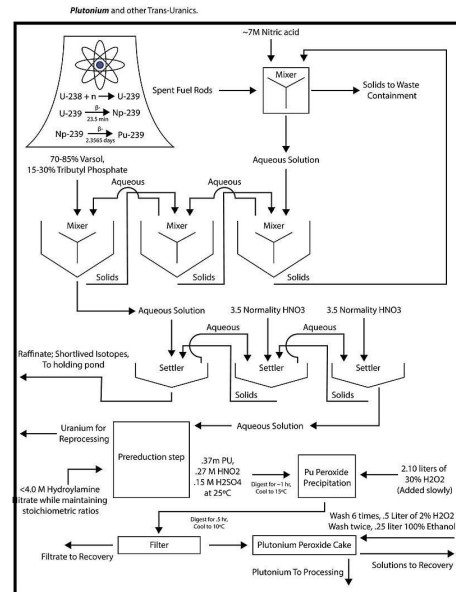

Figure 1. nuclear fuel cycle

Figure 2. Recycling Techniques of Plutonium and Trans-Uranics

Aqueous methods	Non-Aqueous methods
PUREX	LiCl-KCl
UREX	NaCl-KCl
TRUEX	Flouride volatility
DIAMEX	FLUOREX
SANEX	Pyro-A
UNEX+	Pyro-B

Table 1. Aqueous and Nonaqueous Methods

REFERENCES

[1] Allen, T., Busby, J., Meyer, M., & Petti, D. (2010). Materials challenges for nuclear systems. *Materials today*, 13(12), 14-23.
[2] Aruquipa, W., Velasquez, C. E., Pereira, C., Veloso, M. A. F., Costa, A. L., & Barros, G. D. P. (2017). Reprocessing techniques of LWR spent fuel for reutilization in hybrid systems and IV generation reactors.
[3] Taylor, R., Mathers, G., & Banford, A. (2023). The development of future options for aqueous recycling of spent nuclear fuels. *Progress in Nuclear Energy*, 164, 104837.

LAZERLER

İlayda GÜVEN 18022073

Danışman: Doç. Dr. Mehmet KILIÇ

ÖZET

Lazer teknolojisi uyarılmış ışınlardan meydana gelir. Bunu tarihte ilk olarak 191 yılında Albert Einstein dile getirmiştir. 1960 yılında ise Theodore Maiman ilk olarak optik lazer ışınını uygulamaya geçirmiş ve yakut lazeri keşfetmiştir. Bu tez çalışmasında lazerlerin temel bileşenleri, çalışma prensibi ve lazer çeşitlerinin neler olduğunu açıklamak amaçlanmıştır.

GİRİŞ

Lazer (İngilizce: Laser) ışığın uyarılmış radyasyon ile yükseltilmesini sağlayan bir optik düzenektir. İsmini "Light Amplification by Stimulated Emission of Radiation" kelimelerinin baş harflerinden alır ve bu, "ışığın uyarılmış ışıma ile yükseltilmesi" anlamına gelir. Basit şekilde açıklarsak: Akımla uyarılmış olan ışık partikülleri (fotonlar) ışık şeklinde enerji yayarlar. Bu ışık ışın olarak demetlenir. Böylece lazer ışını oluşmuş olur.

Sıradan bir ışık kaynağı tarafından üretilen sıcak beyaz ışık, odaklanmamış yaygın bir ışıma yapar. İnsan gözü ile görünebilir ve renk tayfı içerisindeki pek çok rengin toplamından oluşmaktadır. Öte yandan lazerler dar ve yoğun bir eş-faz ve tek renkli ışık ışını üreten aygıtlardır ve bu nedenle lazerlerden çıkan ışık, bildiğimiz ışıktan tamamıyla farklı özelliklere sahiptir.

LAZERLERİN ÇALIŞMA PRENSİBİ

Lazerlerin çalışma prensibini anlamak için enerjileri E1 ve E 2 olan iki enerji seviyesini göz önüne alalım. Etrafımızda gördüğümüz ışığın neredeyse tamamı, yüksek enerji seviyesindeki (E2) elektronların düşük enerji (E1) seviyesine geçerken fazla enerjilerini (E2-E1) ışık olarak yayması sonucu oluşur. Elektronların yüksek enerji seviyesinden düşük enerji seviyesine geçişi "kendiliğinden" ve "gelişigüzel" olduğu için aynı geçişi yapan her bir elektronun yaydığı ışık, diğer elektronların yaydığı ışıkla uyumlu olmadığı gibi yönleri de farklı ve gelişigüzeldir.

Elektronlardan oluşan böyle bir sisteme dışarıdan ışık gönderilirse, fotonlar enerjilerini düşük enerji seviyesindeki elektronlara aktararak elektronları yüksek enerji seviyesine çıkarır. Bunun sonucunda da ışık "soğurulur" ve fotonlar yok olur. Bu süreç ancak fotonların enerjisi, elektronların bulunduğu enerji seviyeleri arasındaki farka (E2-E1) eşitse gerçekleşebilir.
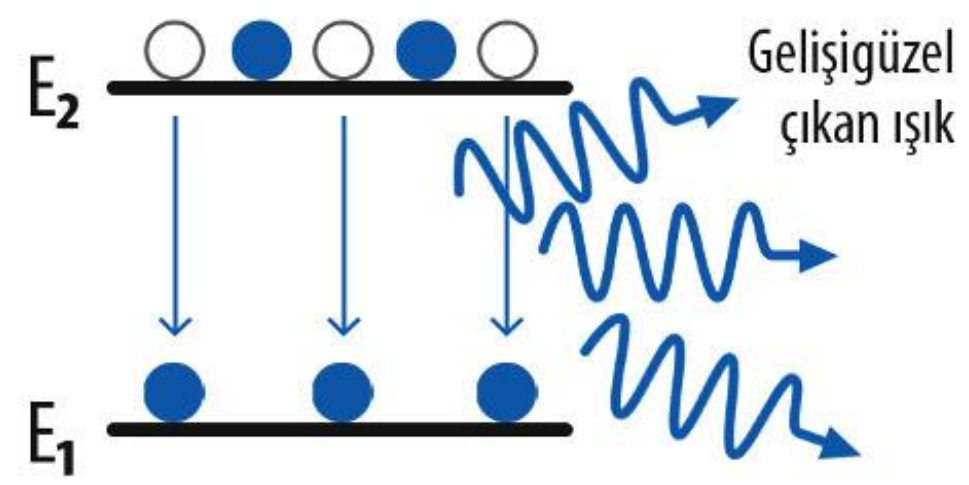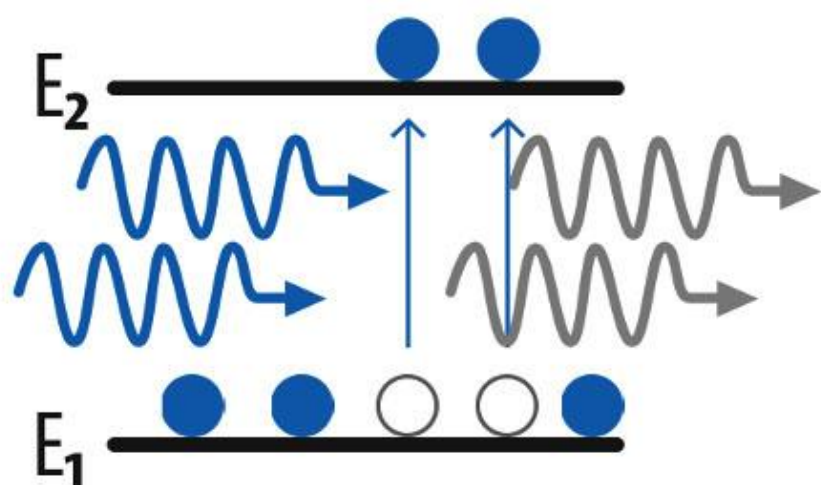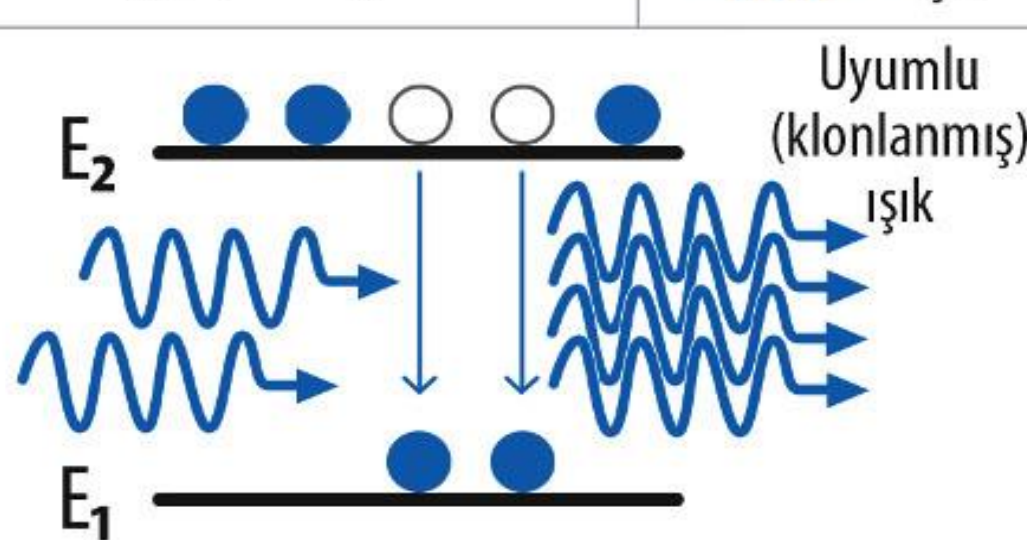

Einstein, elektronların yüksek enerji seviyesinde bulunduğu bir sisteme dışarıdan ışık gönderilirse ışığın elektronları düşük enerji seviyesine inmeye zorlayacağını, bu geçişin sonucunda da yüksek enerji seviyesinden düşük enerji seviyesine inen elektronların yayacağı ışığın elektronları aşağı inmeye zorlayan ışık ile aynı özelliklere sahip olacağını ispatladı. Bu mekanizma, soğurma sürecinin tersi olup "uyarılmış geçiş" olarak adlandırılır. Yani uyarılmış geçişte ışık soğurulmadığı gibi tam tersine kendini klonlayarak güçlenmiş olarak dışarı çıkar.


Lazerler, yüksek enerji seviyedeki elektronların kendiliğinden geçişle normal ışık üretmesini ve düşük enerji seviyesindeki elektronların ışığı soğurarak daha yüksek enerji seviyelerine çıkmasını zorlaştırarak, uyarılmış geçişteki elektron sayısının fazla olmasını sağlayan düzeneklerdir.

LAZERLERİN TEMEL ELEMANLARI

Lazer cihazı ,elektrik enerjisini ışık enerjisine dönüştüren bir apareydir ve üç temel komponenti vardır:
1- Aktif lazer ortamı (Katı,sıvı,gaz formunda olabilir)
2- Optik rezonatör (Aktif ortamın koherent olmayan fotonlarına yeniden yön veren ve çok parlak, doğrusal, tek renkli ve koherent ışık oluşturan kısımdır. Genellikle bir tanesi ışığı hem yansıtan hem de geçiren iki içbükey aynadan oluşur)
3- Aktif lazer ortamının atomlarını uyaran başlangıç enerji kaynağı
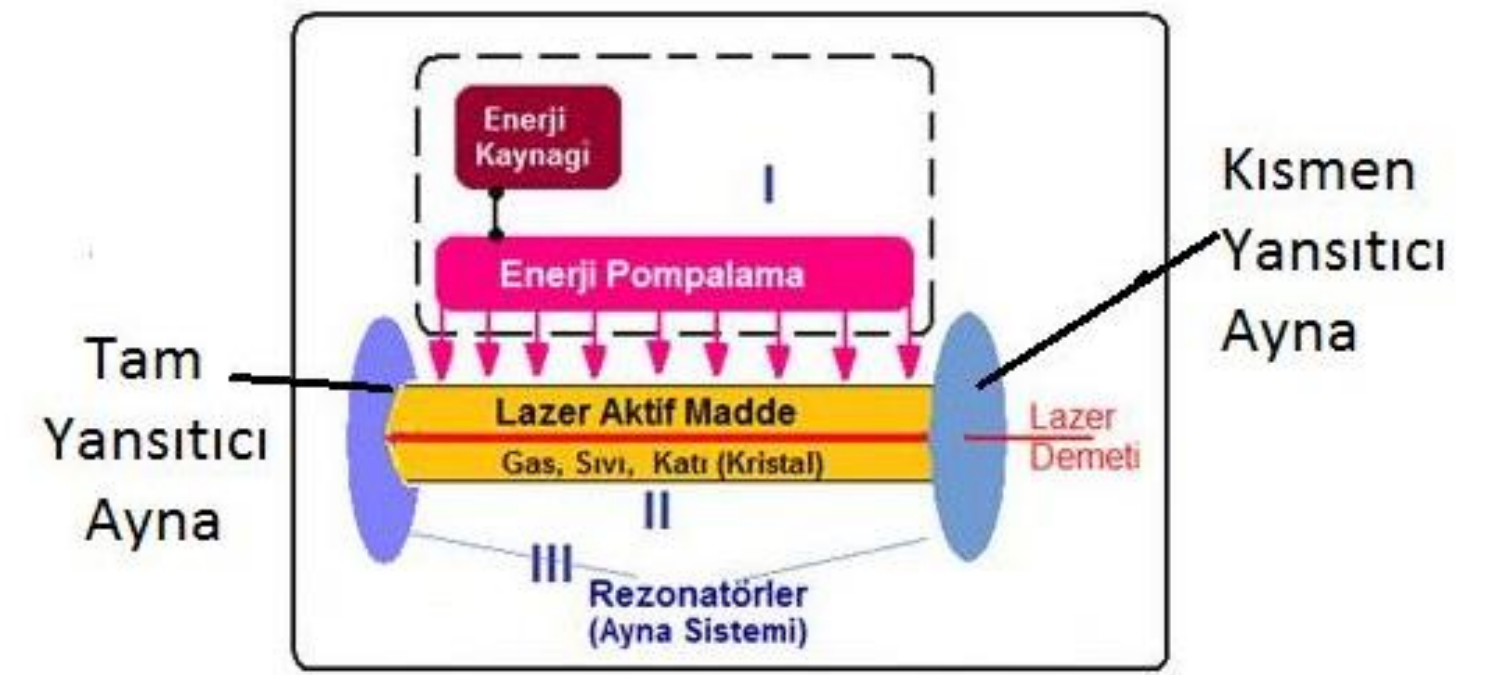
Aktif ortam, evirme işlemini üretmek için harici enerji kaynağı (pompa kaynağı) tarafından uyarılır. Kazanç ortamında, fotonların kendiliğinden ve uyarılmış emisyonu gerçekleşir, bu da optik kazanç veya amplifikasyon yayılımına yol açar.

Yarı iletkenler, organik boyalar, gazlar (He, Ne, CO_2, vb.), Katı malzemeler (YAG, safir (yakut) vb.) genellikle lazer malzemeleri olarak kullanılır ve genellikle lazerler bir ortam olarak kullanılan bileşenler için adlandırılır.

Uyarma kaynağı, pompa kaynağı, evirme işlemi için gerekli olan enerjiyi sağlar ve sisteme salınımı uyarır. Pompalama iki yolla yapılabilir – elektriksel deşarj yöntemi ve ya optik yöntem.

Pompa kaynaklarının örnekleri elektrik deşarjları, flaş lambalar, ark lambaları, başka bir lazerden gelen ışık, kimyasal reaksiyonlar vb.

Rezonatör kılavuzu temel olarak simüle edilmiş emisyon prosesi hakkında bize yön sağlar. Yüksek hızlı fotonlar tarafından tetiklenir. Ardından da bir lazer ışını üretilir.

Sistemlerin çoğunda iki aynadan oluşur. Bir ayna tamamen yansıtıcı olarak kullanılır ve diğeri kısmen yansıtıcı olarak kullanılır. Her iki ayna da birbirine paralel olarak optik eksende ayarlanır.

Aktif ortam, her iki ayna arasındaki optik boşlukta kullanılır. Bu düzenleme sadece eksen boyunca gelen fotonları filtreler ve diğerleri aynalar tarafından yansıtılmış emisyon ile çoğaltılabildiği ortama geri yansır.

LAZER TÜRLERİ

Farklı amaçlar için mevcut birçok lazer türü vardır. Kaynaklara bağlı olarak katı hal lazerler, sıvı lazerler, gaz lazerler olarak sınıflandırılabilirler.

Bazı katı hal lazerler;
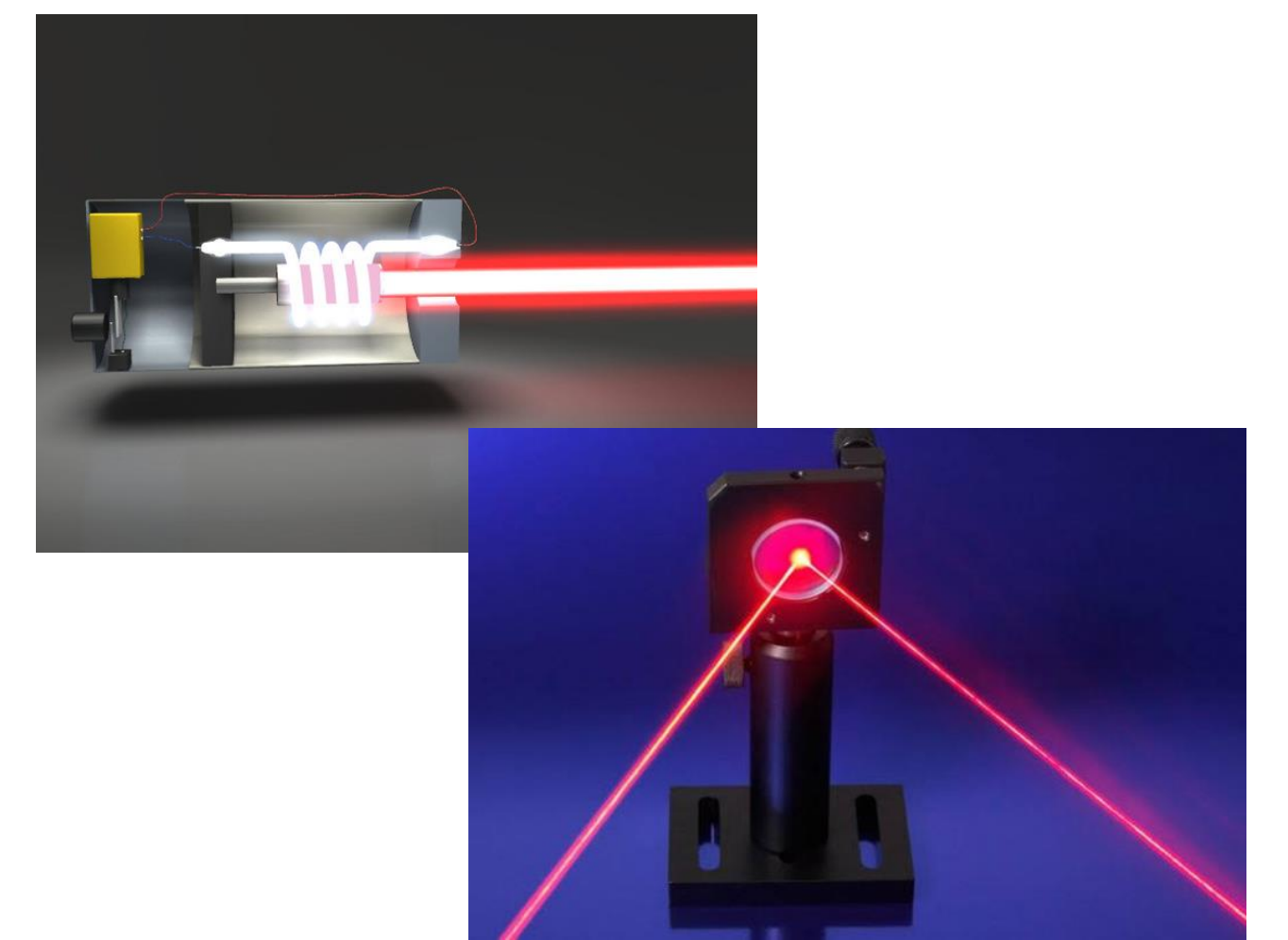-Yakut Lazeri
-ND-Yag Lazeri
-Ti-Safir Lazeri

Sıvı lazerler;
-Boya Lazerleri

Gaz Lazerler;
Atom Lazerler
-Helyum-Neon Lazeri
Molekül Lazerler
-CO2 Lazeri
-Nitrojen Lazeri
-Uzak kızıl-altı Lazeri
İyon Lazerler
-Bakır Buharı Lazeri
-Altın Buharı Lazeri

LAZERLERİN KULLANIM ALANLARI

Günümüzde lazer ışını endüstriyel süreçlerde, mühendislik alanında, tıpta, bilimsel araştırmalarda, meteorolojide, fiber optik iletişim, holografide ve savunma donanımlarında kullanılmaktadır. Lazerler, kullanışlı aletlere bürünerek her geçen gün hayatımızda daha fazla yer ediniyor ve bilimsel araştırmalarda daha fazla kullanılıyor. Lazerlerin gelecekte özellikle kuantum bilgisayarlarının önemli bir parçası olacağı öngörülüyor.

KAYNAKÇA

[1] Wolfgang Demtröder, Atoms Molecules and Photon, Almanya, 2005.
[2] https://acikders.tuba.gov.tr/pluginfile.php/1077/mod_resource/content/1/Bolum-15.pdf

YTU FEN EDEBİYAT FAKÜLTESİ

2023-2024 Spring Semester PHYSICS

DEPARTMENT

A DFT Study on structural,electronic and optical properties of hexagonal monolayer MoS2

SELVİ YAREN SEVİMSİZ-19022072

SUPERVISOR:ASSOCIATE PROF. DR. MURAT ÇALIŞKAN

ABSTRACT: In this study, we have created a drawing of hexagonal, semiconductor MoS2 using VESTA. We calculated the ground state energies of the structure based on the Density Functional Theory Method and VASP Program. By varying the lattice parameters of the atoms, we examined the effects on the surface area of the ground state energies. This allowed us to observe the electrical, optical, and magnetic properties of our hexagonal MoS2 structure

MoS2(MOLYBDENUM DISULFIDE)

Figure 1 Molybdenum [1]   **Figure 2 Sulfur [2]**   **Figure 3 Molybdenium Disülfide [3]**

Molybdenum has a hard structure and a color similar to a silvery-gray hue. It is found in nature indirectly, often forming compounds with other elements.[1] MoS2 (2H phase) is a semiconductor with an indirect band gap of 1.2 eV. Monolayer MoS2 has a band gap of ~1.8 eV.[4] Molybdenum Disulfide is used for example as a photodetector and transistor. The layers are stacked together via van der Waals interactions and can be exfoliated into thin 2D layers. MoS2 belongs to the group-VI transition metal dichalcogenides (TMDC)[4]
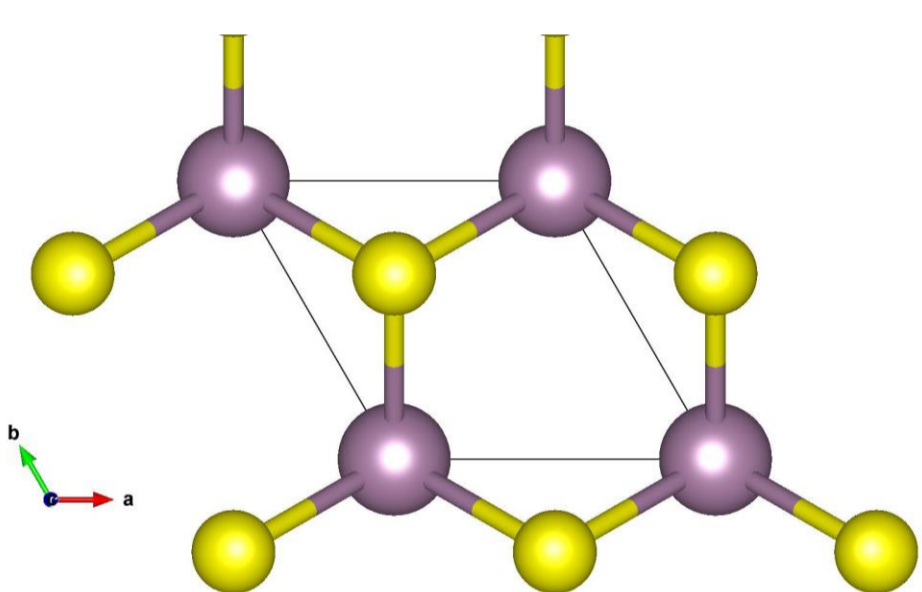
UNIT AND SUPER CELL HEXAGONAL MONOLAYER MoS2

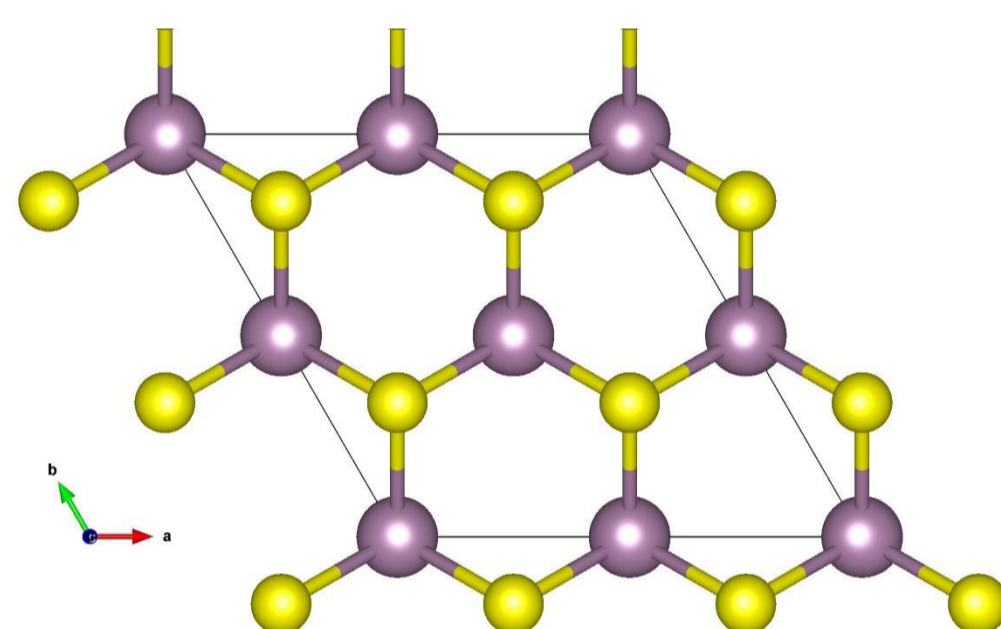**Figure 4 Unit Cell Hexagonal Monolayer MoS2**   **Figure 5 Super Cell Hexagonal Monolayer MoS2**

In the development of the density functional theory used in this study, there are multiple equations and the influence of various theories

1)Schrodinger Equation:
To calculate some features of our structure using DFT, we needed to solve the Schrödinger equation. [5]

$$\hat{H}\Psi(\{\vec{R}_\alpha\};\{\vec{r}_i\}) = \varepsilon\Psi(\{\vec{R}_\alpha\};\{\vec{r}_i\})$$

$$\hat{H} = -\sum_\alpha \frac{h^2}{2M_\alpha}\nabla_\alpha^2 - \sum_i \frac{h^2}{2m}\nabla_i^2 + \frac{e^2}{2}\sum_{\alpha,\beta}\frac{Z_\alpha Z_\beta}{|\vec{R}_\alpha - \vec{R}_\beta|}$$

$$+\frac{e^2}{2}\sum_{i,j}\frac{1}{|\vec{r}_i - \vec{r}_j|} - \frac{e^2}{2}\sum_{i,\alpha}\frac{Z_\alpha}{|\vec{R}_\alpha - \vec{r}_i|}$$

Figure 6 Schrödinger Equation [6]

Actually, solving the time-independent Schrödinger equation is not an easy task. This is due to the fact that the components of the equation have electrostatic correlations among themselves.[5]

2)Hohenberg-Kohn Theorems:
Hohenberg and Kohn developed Density Functional Theory based on two fundamental principles. These principles state that the external potential and energy distribution can be expressed as a functional of the electron density. [5]

3)Kohn-Sham Equations:
The density of states of the non-interacting system, which is the effective potential. and the ground state density of the interacting system are equal to each other. [5]
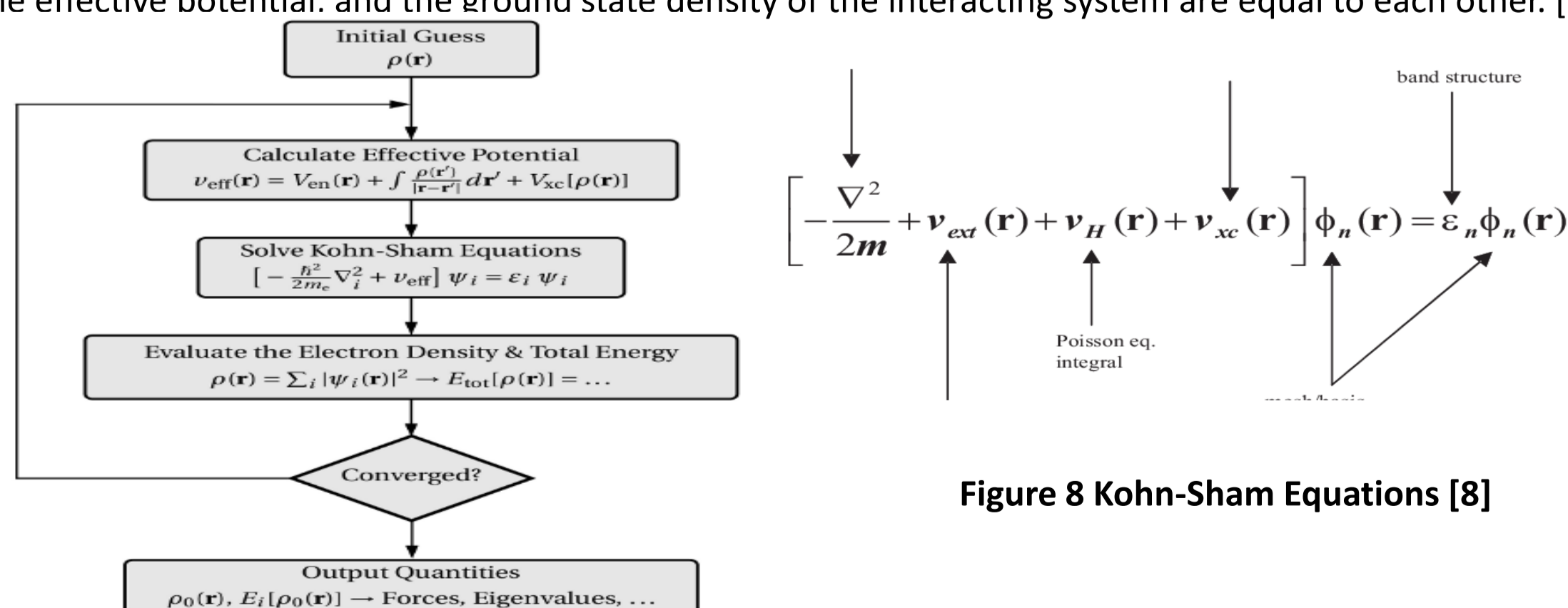

$$\left[-\frac{\nabla^2}{2m} + v_{ext}(\mathbf{r}) + v_H(\mathbf{r}) + v_{xc}(\mathbf{r})\right]\phi_n(\mathbf{r}) = \varepsilon_n\phi_n(\mathbf{r})$$

Figure 8 Kohn-Sham Equations [8]

Figure 7 Kohn-Sham Equation interacting and non-interacting system [7]

As seen from the **Figure 7**, Kohn-Sham equations yield the same solution for both interacting and non-interacting systems.

The calculations are performed using VASP (The Vienna Ab initio Simulation Package: atomic scale materials modelling from first principles), which is based on a plane-wave basis and projected augmented wave (PAW) potentials. We used a plane-wave basis with an energy cut-off 520eV and Monkhorst-Pack k-point mesh 8x8x1. In relaxation calculation interaction force between atoms $0.01\ eV/A^o$ were satisfied.

DENSITY FUNCTIONAL THEORY

In 1927, Thomas and Fermi conducted energy calculations related to electron distribution. Density Functional Theory reduced the electron wave function to electron density, simplifying the calculations. Thomas and Fermi's work on electron distribution was the first significant advancement in the development of Density Functional Theory. [9]
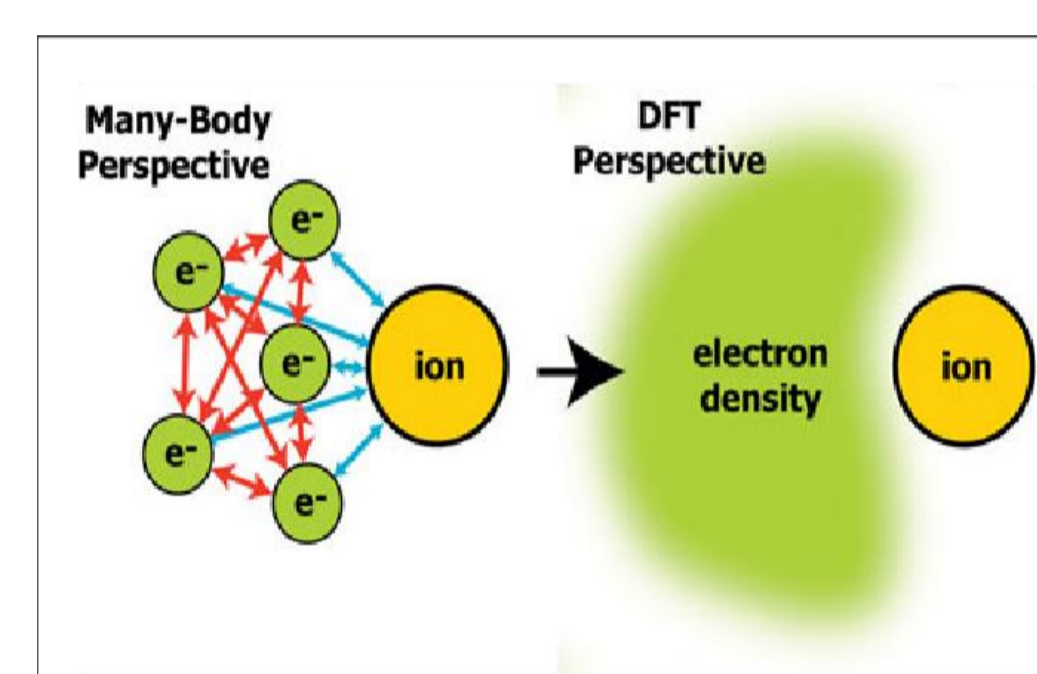

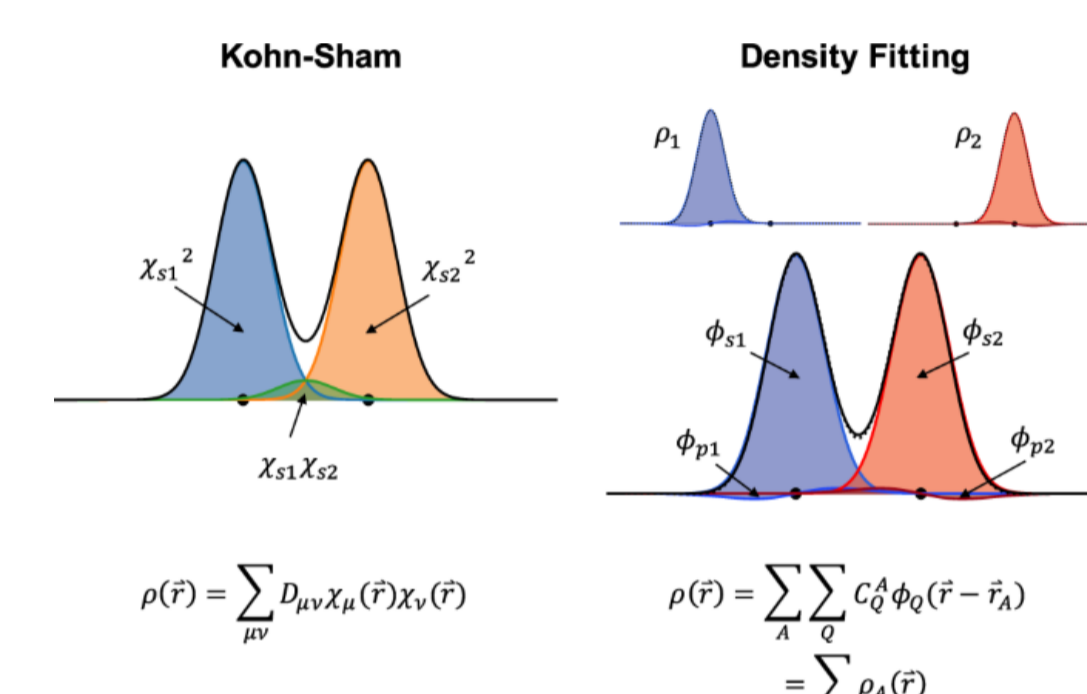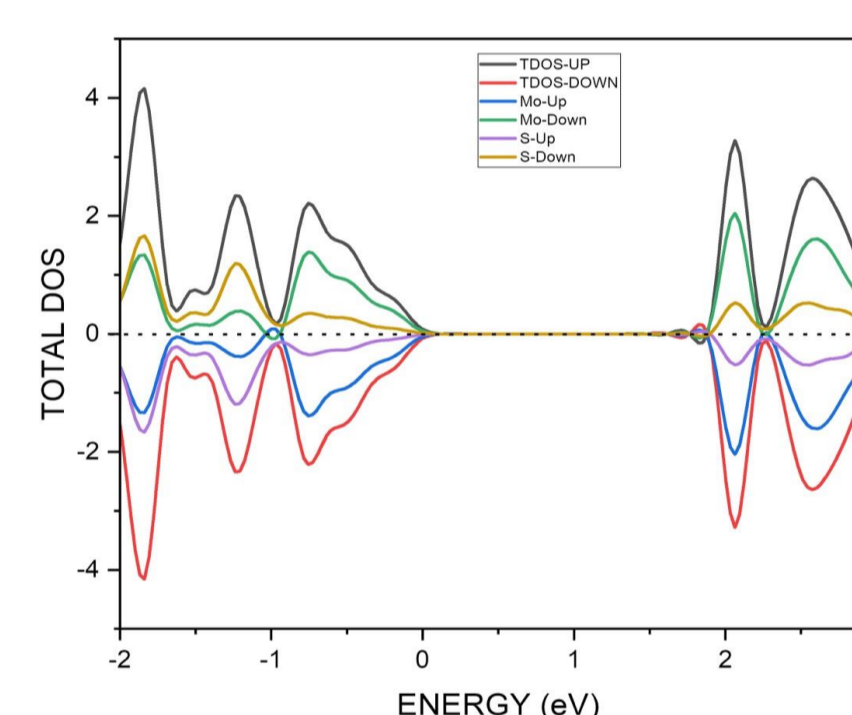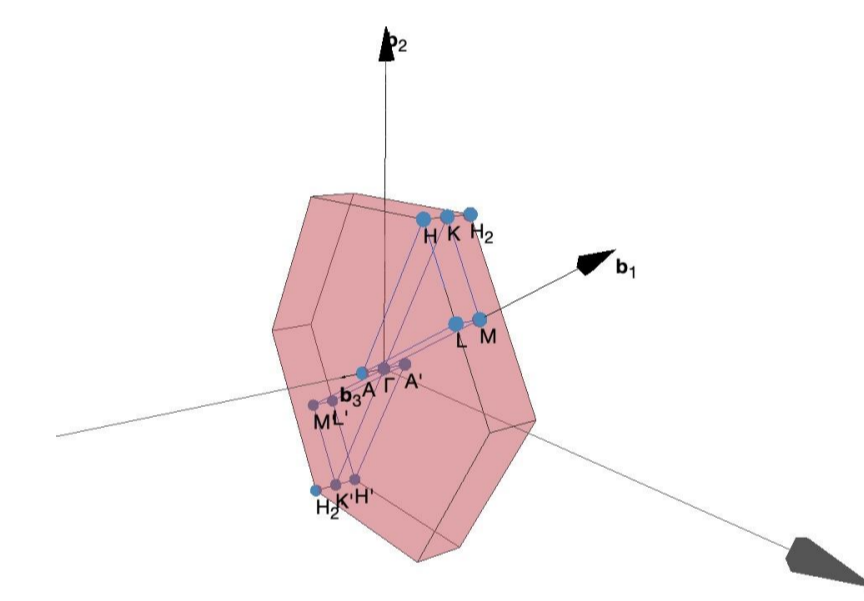**Figure 9 Many Body Persperctive and DFT Perspective [9]**   **Figure 10 Pure non-local machine learned DFT for electron correlation [10]**

In Density Functional Theory, correlation effects are neglected, resulting in a total energy expression that only includes the Hartree Energy and an external potential.

(a)   **(b)**

Figure 11a Total Dos and Partial DOS graph of Hegzagonal Monolayer MoS2 structure.
11.b Reciprocal Lattice of Hexagonal MoS2 monolayer

Table 1:MoS₂ is an INDIRECT BAND GAP Semiconductor

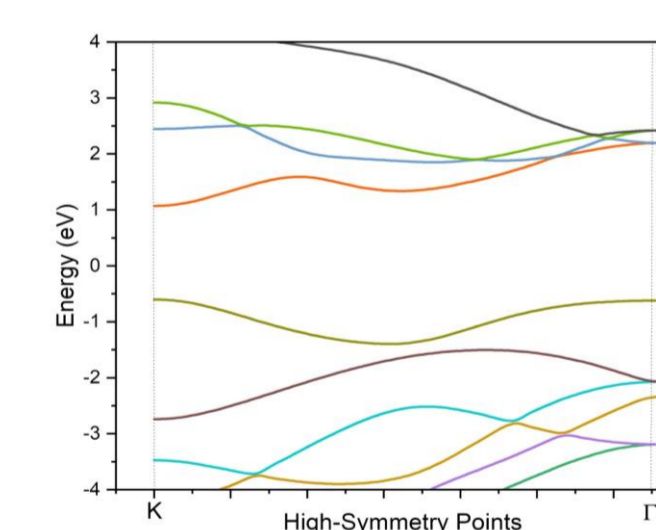| Spin Ch	Cannel:	<UP>	<DOWN>	<TOTAL>
Band Gap	(eV):	1.6737	1.6737	1.6736
Eigenvalue of VBM	(eV):	-2.0534	-2.0535	-2.0534
Eigenvalue of CBM	(eV):	-0.3797	-0.3798	-0.3798
Fermi Energy	(eV):	-1.4502	-1.4502	-1.4502

Figure 12 Band Diagram of Hegzagonal Monolayer MoS2 Structure

VASP(Vienna Ab initio Simulation Package)

VASP clarifies the concepts of single-electron orbitals, electronic charge density, and potential using fundamental wave sets.[11]The VASP program consists of 4 files. These are INCAR, POSCAR, POTCAR, and KPOINTS

1-INCAR: The INCAR file, being the primary input file of VASP, specifies both the tasks to be performed and the methodologies to be employed

2-POSCAR: It is a file containing the lattice geometry and positions of ionic crystals.

3-POTCAR: gives the pseudopotential for each type of atom used

4-KPOINTS: This file defines the Bloch vectors (k points) utilized for sampling the Brillouin zone[12]

CONCLUSION: By using Computational Theoretical Physics, we were able to obtain the optical, electrical, and magnetic properties of our MoS2 semiconductor. In my opinion, the field of Computational Theoretical Physics is leading the way in many areas today and will be highly beneficial for both experimental and theoretical scientists in the future. This was the main motivation behind choosing this topic for this study.

REFERENCES
[1] https://zormetal.com/products/molibden/
[2] https://www.makaleler.com/kukurt-nedir-nerelerde-kullanilir
[3] https://www.hqgraphene.com/MoS2.php
[4] Investigation of the Effect of Solvent and Heat Treatment Process on Structural Properties of MoS2 Thin Films Burak Kıvrak 1,2* , Mustafa Akyol 1 Araştırma Makalesi/Research Article DOI:10.21205/deufmd.2022247009 Atıf şekli/ How to cite: KIVRAK, B., AKYOL, M.(2022). Çözücü ve Isıl İşlem Sürecinin MoS2 İnce Filmlerinin Yapısal Özelliklerine Etkisinin İncelenmesi.DEUFMD, 24(70),81-90.
[5] DOKUZ EYLÜL UNIVERSITY GRADUATE SCHOOL OF NATURAL AND APPLIED SCIENCES ELECTRONIC STRUCTURE OF PARABOLIC CONFINING QUANTUM WIRES WITH RASHBA AND DRESSELHAUS SPIN-ORBIT COUPLING IN A PERPENDICULAR MAGNETIC FIELD
[6] https://www.maths.tcd.ie/~bmurphy/thesis/thesisse6.html
[7] https://iue.tuwien.ac.at/phd/goes/dissse14.html
[8] https://www.researchgate.net/figure/Some-of-the-choices-made-in-a-Kohn-Sham-calculation-The-treatment-can-be-nonrelativistic_fig2_1839487
[9] https://www.researchgate.net/figure/Density-functional-theory-DFT-abandons-the-manyparticle-electron-reality-in-favor-of_fig2_259406317[
[10] https://www.nature.com/articles/s41467-020-20471-y
[11] https://cmp.univie.ac.at/research/vasp/
[12][https://acikders.ankara.edu.tr/pluginfile.php/160913/mod_resource/content/1/Ders6.pdf

![YTU FEN EDEBİYAT FAKÜLTESİ logo]

2023-2024 Spring Semester PHYSICS DEPARTMENT

Organic Scintillator Signal Analysis with Machine Learning

Uğur GENÇER 19022062

Supervisor: Lect. PhD Özgür AKÇALI

ABSTRACT

Organic scintillators are crucial in neutron detection and spectrometry due to their high efficiency and rapid response. The ability to distinguish between neutron and gamma-ray signals in these detectors is essential for accurate measurements. This study explores the application of artificial neural networks (ANN) in enhancing neutron/gamma discrimination using organic scintillator data. Synthetic signals were generated to simulate real-world detection scenarios, incorporating parameters such as rise and fall times and normalization factors. The ANN model developed in this research achieved a 99% accuracy rate in differentiating proton, neutron, and photon signals. This high accuracy demonstrates the model's potential to improve the precision and speed of radiation detection systems. The findings suggest that integrating machine learning techniques with traditional scintillator data analysis can significantly enhance the performance of particle detection systems, providing valuable insights for both scientific research and practical applications in various industries.

INTRODUCTION

Organic scintillators have been widely used in neutron detection and spectrometry due to their short decay time, high detection efficiency, and excellent neutron/gamma (n/γ) discrimination performance. Neutrons are always accompanied by gamma rays, and since organic scintillators are sensitive to both, it is essential to discriminate between these two types of radiation. The scintillation light of organic scintillators comprises fast and slow components, with the latter originating from the excitation of long-lived triplet states of π-electrons [1]. Neutron-induced events have a higher proportion of the slow component compared to gamma-ray-induced events, as neutrons induce protons that excite more π-electrons into triplet states. Consequently, neutron pulses exhibit flatter falling edges, enabling n/γ discrimination through pulse shape discrimination (PSD) [1][2]PSD can be implemented in both time and frequency domains. Time domain PSD algorithms include the charge comparison method (CCM), zero-crossing method, and pulse gradient analysis, while frequency domain PSD algorithms encompass frequency gradient analysis, power spectrum analysis, and wavelet transform [3]. These algorithms achieve discrimination by analyzing different pulse shape parameters (PSP), which are determined by the shape rather than the amplitude of the pulse. By accumulating pulse numbers according to their PSP intervals, a double-peak distribution emerges, allowing the calculation of the figure of merit (FoM) to evaluate discrimination performance [2]. Recent developments in machine learning (ML) have introduced new methods for n/γ discrimination. ML algorithms such as artificial neural networks (ANN), clustering, and deep learning have been employed, each using different evaluation indicators compared to traditional methods. Instead of FoM, metrics such as discrimination error ratio (DER), gamma-ray rejection ratio, and classification accuracy are used to quantify discrimination performance. Nonlinear support vector machines (SVM) are also applied in conjunction with other algorithms, including moment analysis, nonnegative matrix factorization, and continuous wavelet transform, with DER and generalization error being calculated and the probabilities of new particles analyzed [2][3].

In this study, the focus is on the development of artificial neural network (ANN) models for use in organic scintillators. Using synthetic signals and the Figure of Merit (FoM) method, we have developed an ANN model with a high degree of accuracy. This model has demonstrated the ability to distinguish between proton, neutron, and photon signals with an accuracy rate of 99%. Achieving this level of success is significant as it enables more accurate and rapid analysis of nuclear events. The enhanced precision and speed provided by this ANN model hold the potential to significantly improve the performance and application of radiation detectors in various scientific and industrial contexts.

METHODOLOGY

The Figure of Merit (FoM) is essential in evaluating signal discrimination efficacy in scintillation detection systems. FoM, calculated as the ratio of the tail integral to the total integral of the signal waveform, highlights differences in decay characteristics between various particle types. The tail integral captures the lingering part of the signal, aiding in differentiating between electrons, photons, and neutrons, while the total integral represents the entire event energy. This ratio emphasizes temporal distinctions, enhancing the neural network model's discrimination power. Thus, FoM is crucial for both signal processing and the success of the machine learning model in this study.

Ionizing radiation detection by scintillators can be split into two main steps. Initially, the absorption of the energy of the incoming particle by the scintillator material and emitting multiple photons by shifting the wavelength to the visible range of the spectrum. Next, the produced visible light is amplificated by a photo multiplier tube (PMT). While the first step is a function of scintillator material, the second is a function resulting from PMT electronics. In this study, a two-part discrete function is used to simulate the signal of a complete event. The suggested function have a semi Gaussian form fort the rising part of the signal and an exponential decay thereafter. A Python function (3.1) is defined to generate signals; the input parameters of the function are s_r as rise time, s_f as fall time, N as normalization factor, t_0 as the transition point of the signal (i.e., the time when the exponential decay begins), and t represents time. The mathematical form of the function is defined as:

$$f(t, t_0, s_r, s_f, N) = \begin{cases} N \cdot e^{-\frac{1}{2}\left(\frac{t-t_0}{s_r}\right)^2}, & t < t_0 \\ N \cdot e^{-\frac{t-t_0}{s_f}}, & t > t_0 \end{cases} \quad (3.1)$$

To achieve realistic synthetic data, the normalization factor (N) was randomized between 50 and 600 to reflect the potential intensities of the detected signals. The standard deviation of the rise time (s_r) was set at 6 ns, allowing for a fluctuation (error) of ±0.5 ns. The fall time factor (s_f) was determined to be 25 ± 2 ns for protons, 50 ± 2 ns for neutrons, and 100 ± 2 ns for photons. These values were chosen to enable discrimination between different types of particles. Additionally, the time variable (t) was divided into 1024 discrete parts ranging from 0 to 400 ns to obtain a simulation comparable with the experimental equipment. The transition point (t_0) value was randomly assigned between 30 and 300 ns to replicate the variable nature of the event timing within the system. Utilizing the parameters described above, random signals were generated. To each created signal, a random white noise of 5 ± 3 units was added to mimic real-life signals. To approximate real-world conditions, a linear regression was employed to identify certain characteristic points of each signal. In order to determine the rise and fall time of the signal, a 10% low level and a 90% high level threshold with respect to N, is used. The time coordinate values are calculated by interpolation as the signal crosses the selected thresholds. Time coordinate marks presented by sub indices ranging from 1 to 4 are used in pairs as 1 and 2 to calculate the rise time and 3 and 4 for fall time.The interpolated threshold crossing points were used as the boundaries of the total and tail integrals, computations facilitated by the quadratic integration method of the SciPy library. For every individual signal, the Figure of Merit (FoM) was derived by dividing the tail integral, spanning from t_3 to t_4, by the total integral, which spans from t_1 to t_4. This ratio serves as a critical metric for evaluating the performance and discrimination capabilities of the detection system. (Figure 4)

RESULTS & CONCLUSION

In this section, we first present the synthetic signals generated for this study. Figure 7 displays signals with identical t_0 and N parameters but different fall times s_f ; where the blue signal represents a charged particle, the red signal represents a photon, and the green signal represents a neutron. Similarly, Figure 8 illustrates signals with the same t_0 but varying N values. For each type of signal, 50,000 instances were generated.(Figure12)Subsequently, the discriminative power of these parameters was evaluated. As shown in Figure 9, the discrimination capability of the N values is assessed through the Figure of Merit (FoM). Data visualization was enhanced by employing scatter plots and the Gaussian Kernel Density Estimation (KDE) method. Figure 10 investigates whether distinctions in FoM values correspond to differences in tail integral values, using the same visualization approach. Lastly, Figure 11 explores the discriminability between tail integral and total integral values.The visualized data confirm the presence of discriminable features, which were then utilized to create datasets for Artificial Neural Network (ANN) modeling.

In this study, we developed various deep learning models using the Keras framework to predict and classify scintillation signal data.

Regression Model: We created a regression model to predict continuous outputs related to the rise and fall times of signals indicative of particle interactions. The model was trained over 100 epochs with a batch size of 256 and evaluated using mean squared error (MSE) and the coefficient of determination (R² score). The results showed high predictive accuracy, with low MSE and high R² scores on both training and test sets (Table 1).
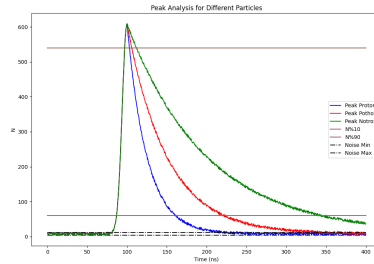
Figure 7: Synthetic Signals with Different Fall Times (s_f) but Identical t_0 and N Parameters
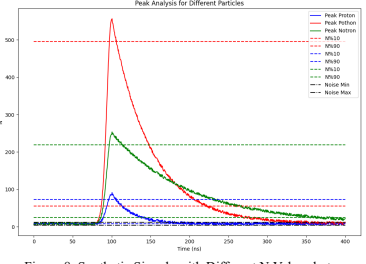
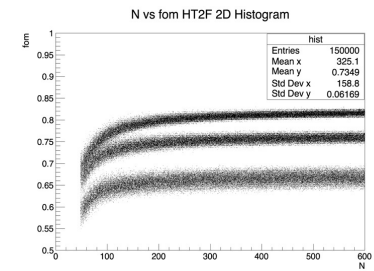Figure 8: Synthetic Signals with Different N Values but Identical t_0

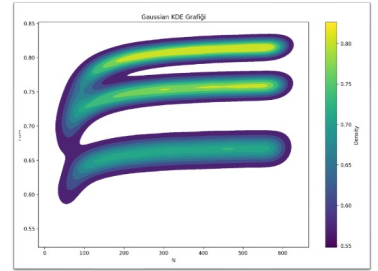Figure 12 : Each point represents a data point.

Figure 9: Discrimination Capability of N Values Evaluated Through Figure of Merit (FoM)
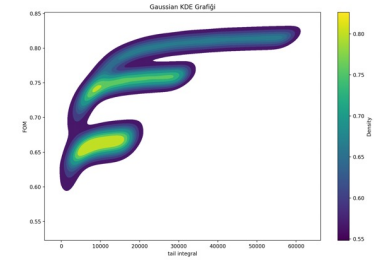
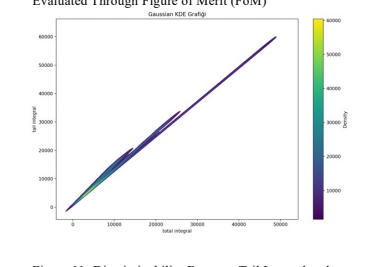Figure 10: Relationship Between FoM Values and Tail Integral Values

Figure 11: Discriminability Between Tail Integral and Total Integral Values

Classification Model: Another deep learning model was developed to classify signal data for three particle types (electrons, neutrons, and photons). The data, sourced from three different parameter files, was combined and labeled for training the artificial neural network (ANN) model. Hyperparameters, including activation function, optimizer, epochs, batch size, and validation split, were optimized through trial and error. The model's performance was assessed using accuracy and a confusion matrix, demonstrating its effective classification capabilities (Tables 2 and 3).

Table 1:Regression Model Performance Metrics

Dataset (Particle)	MSE (s_r)	R² (s_r)	MSE (s_f)	R² (s_f)
Neutron (par100)	0.01854	0.77664	0.04044	0.96968
Photon (par50)	0.01682	0.79854	0.02614	0.98055
Electron (par25)	0.0099	0.88041	0.01459	0.98899

Table 2: Model Evaluation Metrics

Metric	Value
Test Loss	0.0974
Test Accuracy	0.9926

Table 3: Confusion Matrix

Actual\Predicted	Electron	Photons	Neutrons
Electron	14994	0	0
Photons	7	14788	166
Neutrons	0	160	15045

This study utilized synthetic signals to illustrate the distinct decay characteristics of different particle interactions, employing the Figure of Merit (FoM) to emphasize differences in signal structure. The FoM, a ratio of the tail integral to the total signal integral, helped develop accurate artificial neural network (ANN) models with low mean squared error (MSE) and high R² scores. By using synthetic data, we simulated realistic conditions and generated signals that mimic real-world data, enhancing model accuracy. Future work will involve validating these ANN models with real-world data to ensure robustness and applicability in particle detection. This research demonstrates the potential of ANNs in improving data quality and accuracy in particle detection systems.

REFERENCES

1. Pozzi, S. A., Bourne, M. M. & Clarke, S. D. Pulse shape discrimination in the plastic scintillator EJ-299-33. *Nucl. Instrum. Methods Phys. Res. Sect. Accel. Spectrometers Detect. Assoc. Equip.* **723**, 19–23 (2013).

2. Olivieri, A. C. & Escandar, G. M. Analytical Figures of Merit. in *Practical Three-Way Calibration* 93–107 (Elsevier, 2014). doi:10.1016/B978-0-12-410408-2.00006-5.

3. Langeveld, W. G. J., Glenn, A. M., Sheets, S. A., Strellis, D. A. & Zaitseva, N. P. Comparison of pulse shape discrimination performance of stilbene and liquid scintillator under high count-rate active interrogation conditions. *Nucl. Instrum. Methods Phys. Res. Sect. Accel. Spectrometers Detect. Assoc. Equip.* **954**, 161204 (2020).

YTU FEN EDEBİYAT FAKÜLTESİ

2023-2024 Spring Semester

DEPARTMENT OF PHYSICS

ALPHA AND ALPHA CLUSTER DECAY

GÜLİN ERTAŞ 19022061

Supervisior: Prof. Dr. KUTSAL BOZKURT

ABSTRACT

In this thesis, clustering and alpha decay are described. The escape of alpha particles from the nucleus is explicated through quantum tunneling. Furthermore, examples pertaining to clustering have been provided. According to the reviewed results, it can be concluded that among various decay modes occurring in heavy nuclei, alpha decay is superior[1].

GENERAL INFORMATION

Alpha decay occurs as α-particles penetrate nucleus barriers via tunneling[6]. Classically, this tunneling does not occur, but from a quantum mechanical perspective, it does[6].This phenomenon led to the development of quantum mechanics and has found application in almost every technology[6]. Tunneling occurs within the nucleus due to two effective forces: The Coulomb Repulsive Force and The Strong Nuclear Force[6]. When approaching the nucleus's surface, the density decreases and weakens the nuclear force[6]. The α-particle at the surface overcomes the Coulomb force and escapes through quantum tunneling[6]. An alpha particle at the nucleus's surface succeeds in crossing the barrier after approximately 10^{38} attempts and emerges[6]. Sometimes, this event can also be viewed as alpha particle clustering. The investigation of the formation of alpha clusters within the atomic nucleus dates back to the early days of nuclear physics[4]. Alpha clustering can be defined as the grouping of protons and neutrons into a nucleus into α-particle configurations.
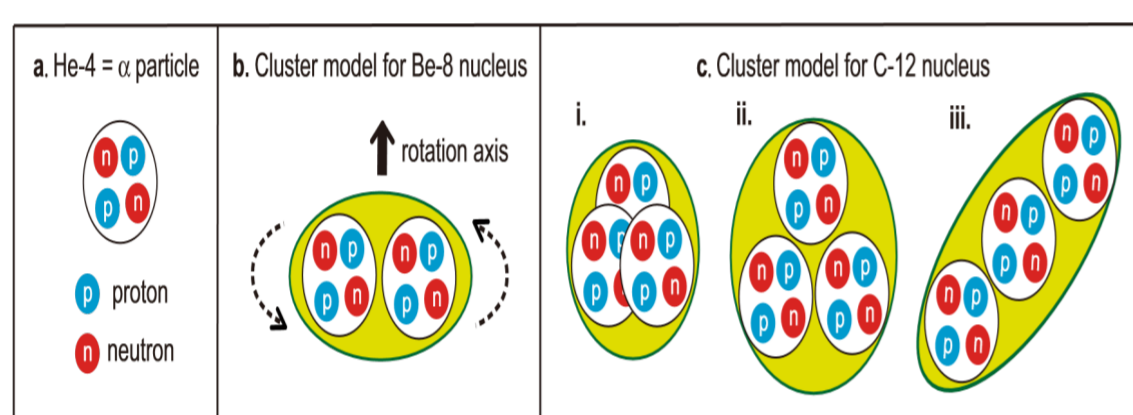

Fig.1 Alpha particle and alpha cluster representation[2]

THEORETICAL MODEL

Alpha Decay

Alpha decay refers to the emission of a ^{4}He nucleus, consisting of 2 n^0 and 2 p^+, from the nucleus of atom.[6]
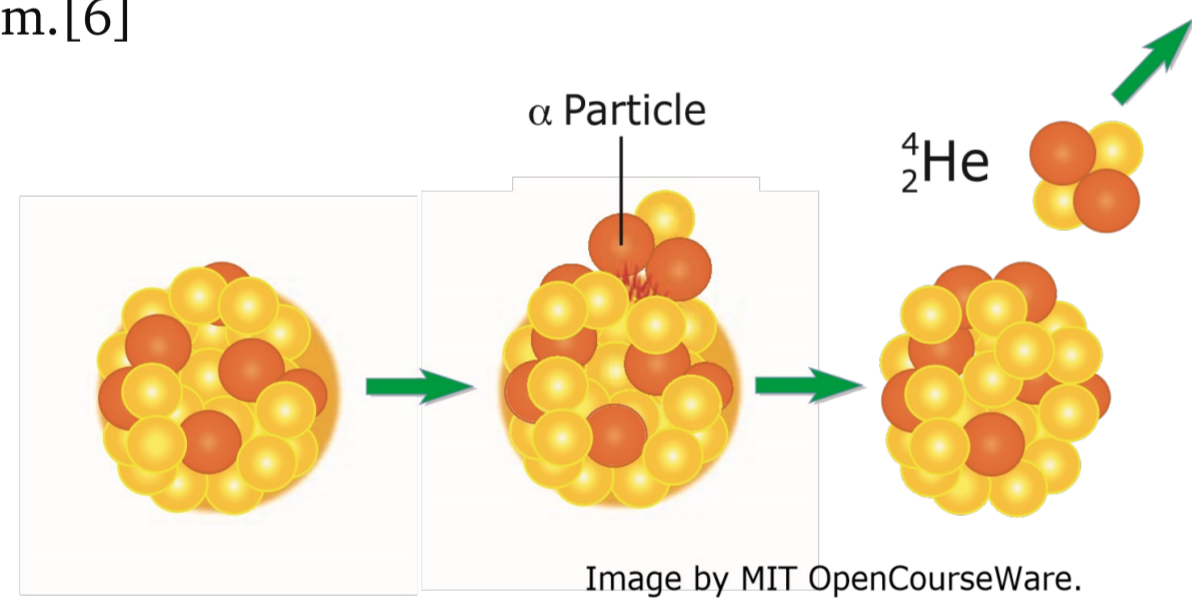

Fig.2 Alpha decay diagram[3]

Alpha decay was discovered by Henri Becquerel in France[1]. Subsequently, the particle produced as a result of decay, the ^{4}He nucleus, Ernest Rutherford was the individual who recognized it.[1]

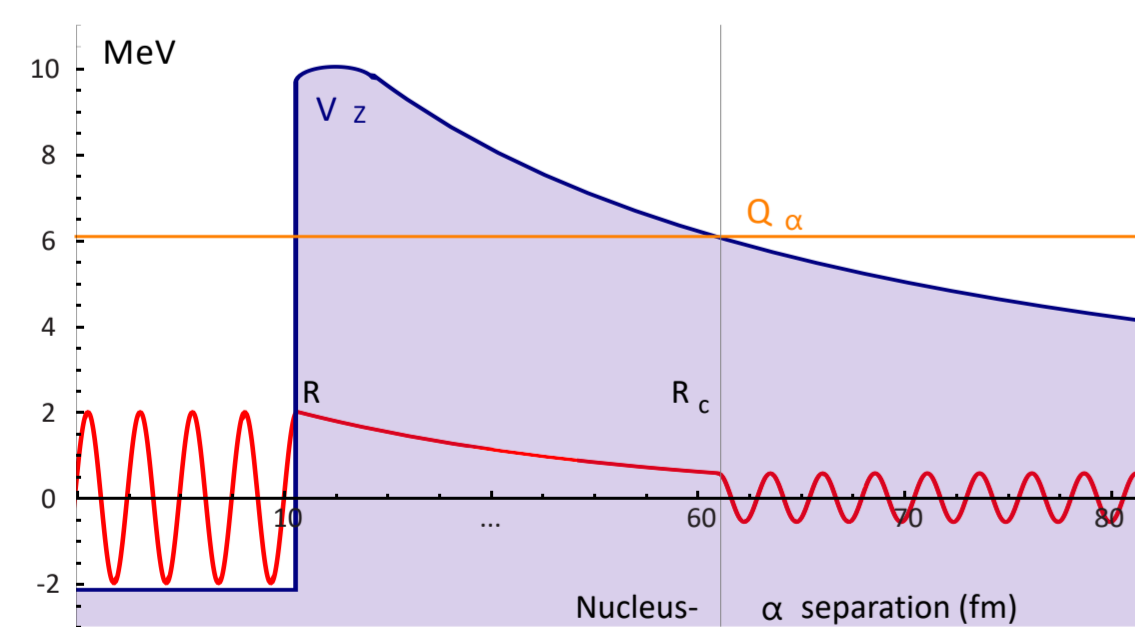### Alpha Particle Escape via Quantum Tunneling

Fig.3 Tunneling model of alpha emission [3]

There are three different regions where the alpha particle can escape by tunneling[6]

At r <R there is a potential well with a depth of $-V_0$. The kinetic energy = $Q+V_0$ (here, Q=Eα).The α-particle cannot escape the Coulomb barrier because there is a very strong nuclear force in this region.[6]

At R< r < R_c the total potential energy is greater than Q (where Q=Eα) When the α-particle precisely reaches R, it creates a hole on the surface of the nucleus and escapes through quantum tunneling. [6]

Within the range of R- R_c the nuclear force decreases, but classically α-particles cannot escape from this region because of their energy. For r >R_c it is the classically allowed region outside the barrier [6]

History of Alpha Cluster

After discovering that an alpha particle is a ^{4}He atom, scientists initially assumed that the nucleus was composed of fixed α-particles[4]. George Gamow proposed this as a nuclear model in the 1930s[4]. However, this model was quickly abandoned following Chadwick's discovery of the neutron in 1932 and new data from nuclear research[4]. Below are tables and diagrams showing the historical development and evolution of nuclear models from Gamow's initial concept to subsequent advancements.[4]
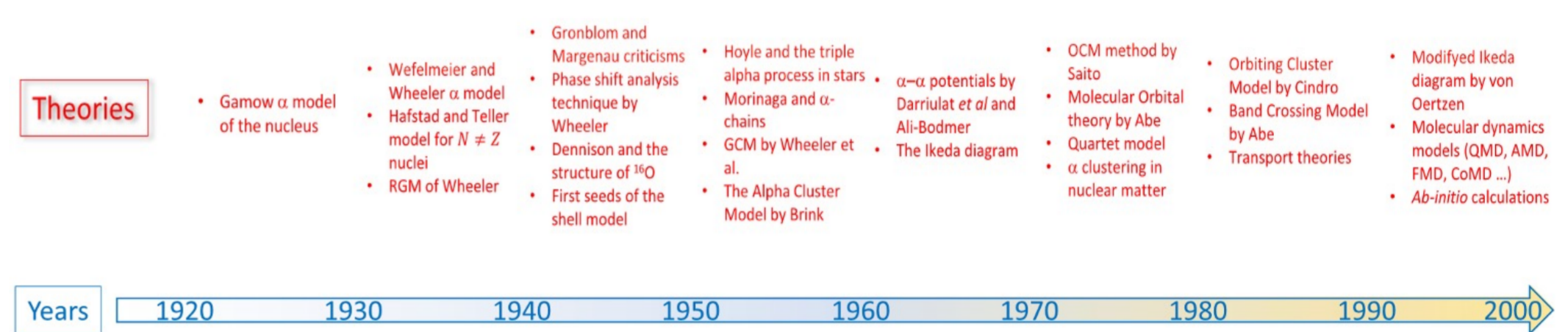

Fig.4 The diagram above demonstrates the developments in the nucleer cluster model of the atomic nucleus between the years 1920 and 2000 [4]
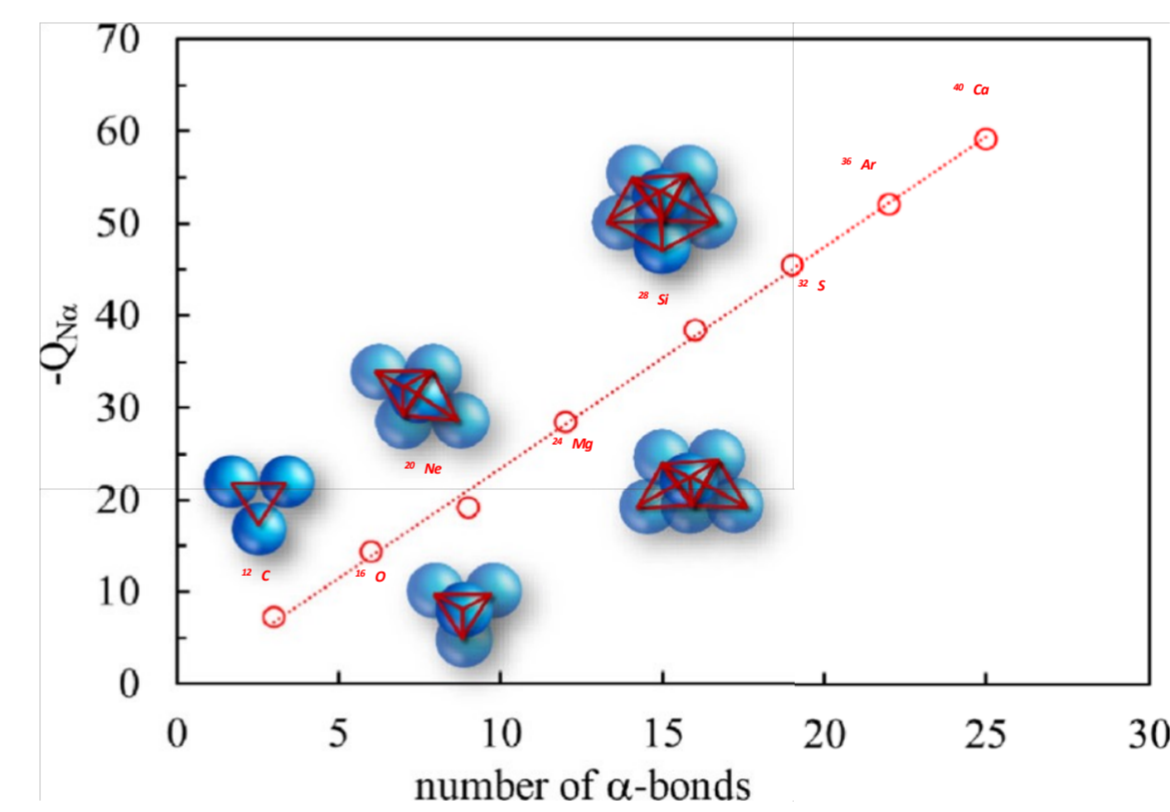

Fıg.5 In the picture, the geometric arrangements in self-conjugated nuclei are shown to be equal to the bonds of α-particles [4],[5]

Astrophysical Perspectives on Clustering

Clustering in nuclear astrophysics is crucial for processes like stellar nucleosynthesis and evolution[4]. One of the prime examples is the formation of ^{12}C through the 3α process[4]. Fred Hoyle suggested in 1953 that this fusion could occur resonantly[4]. If significantly clustered into ^{8}Be +α or 3α for the Hoyle state,the probability of fusion increases.[4]
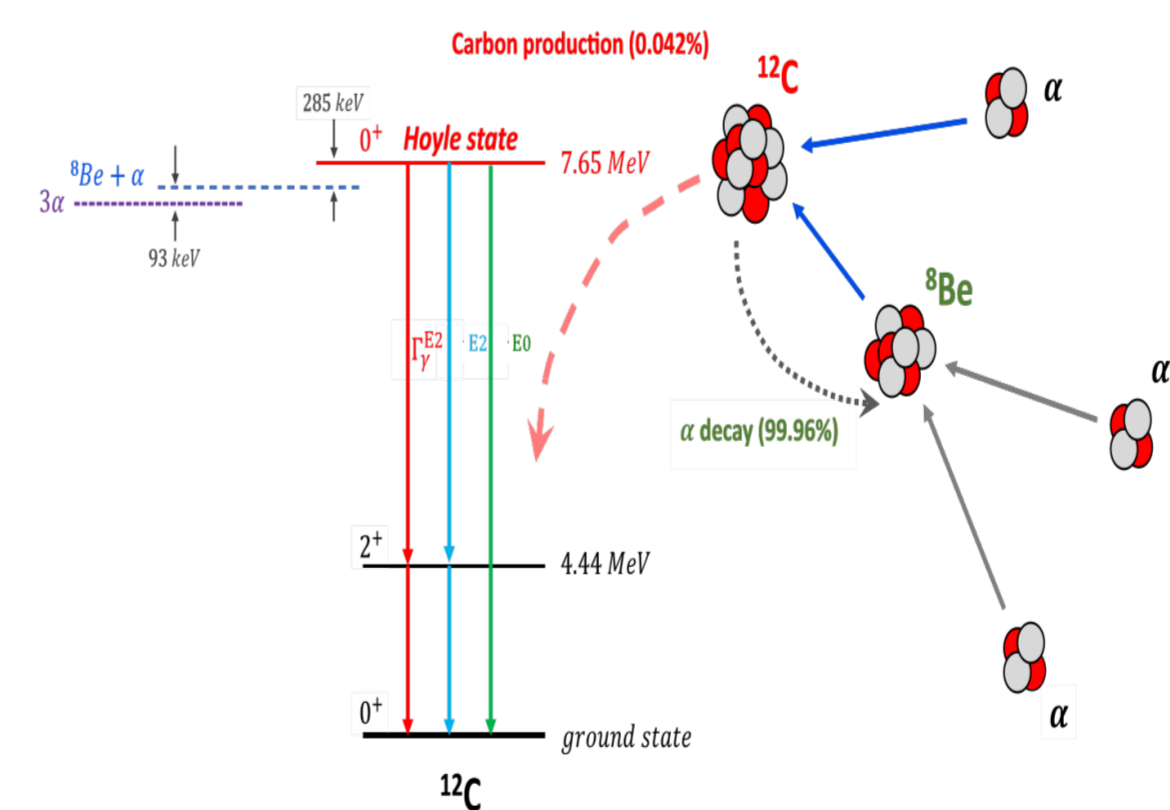

Fig.6 In stars, the triple-alpha process is depicted, with transitions between designated states of ^{12}C shown in different colors [4]

DISCUSSION AND CONCLUSION

As a result of an article analyzed, it can be concluded that as a result of the various decays that occur in heavy nuclei, which can be listed as ternary fission, spontaneous fission, cluster decay, and alpha decay[1]. When comparing the half-life values for all these decay modes, it is indicated that α-decay has the lower values. It is concluded that the nuclei ^{318}126, ^{319}126, ^{320}126 and $^{323-326}$126 , can only be detected via alpha decay.[1]

REFERENCES

[1] H.C. Manjunatha et al.,Science Direct, 2017

[2] T.Otsuka et al.,Nature Communıcatıons,2022

[3] MIT Opencourse Ware , http://ocw.mit.edu ,2012

[4] Ivano Lombardoet al.,Springer,2023

[5] L.Elton,Pitman,1966

[6]Kutsal Bozkurt,Nuclear Lectures Notes,2023

2023-2024 Spring Semester

DEPARTMENT OF PHYSICS
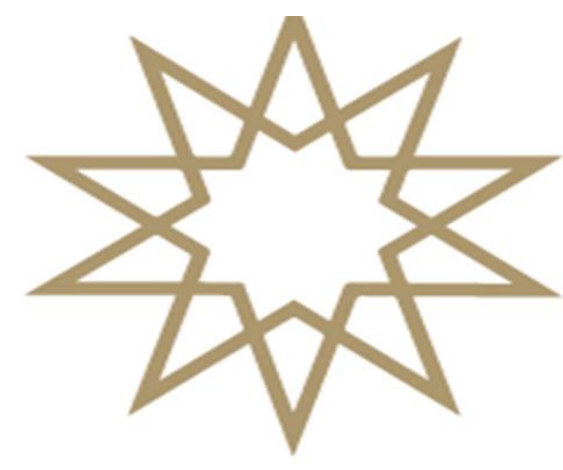
Unveiling the Higgs: Classification of Particle Decays with Advanced Machine Learning Techniques

Student: Mina YAVUZ 20022603 Advisor: Prof. Bora IŞILDAK

Abrsact

This study utilizes a machine learning-based dataset from the ATLAS experiment at CERN's Large Hadron Collider (LHC) to distinguish between background and signal events, specifically focusing on the decay of the Higgs boson into two tau particles (H → ττ). The dataset, derived from ATLAS open data, consists of simulated events from proton-proton collisions. This classification task is framed as a binary classification problem, aiming to accurately separate signal events from background events using various machine learning techniques. Several classification algorithms were employed, including support vector machines (SVM), Logistic regression, k-nearest neighbors (KNN), XGBoost, and AdaBoost. The performance of these classifiers was evaluated using classification reports, Receiver Operating Characteristic (ROC) curves, and Area Under the Curve (AUC) scores. XGBoost achieved the highest accuracy with an AUC score of 0.84, demonstrating its effectiveness in distinguishing signal from background events. The study highlights the potential of machine learning in enhancing high-energy physics research.

DATA ANALYSIS

- **Exploratory Data Analysis:**

We also utilized histograms to visualize these distributions. For each feature, we plotted two overlaid histograms: one for the signalevents and one for the background events. This visualization helped in identifying which features showed significant differences between the signal and background densities, providing insights into which features might be most useful for the classification task.
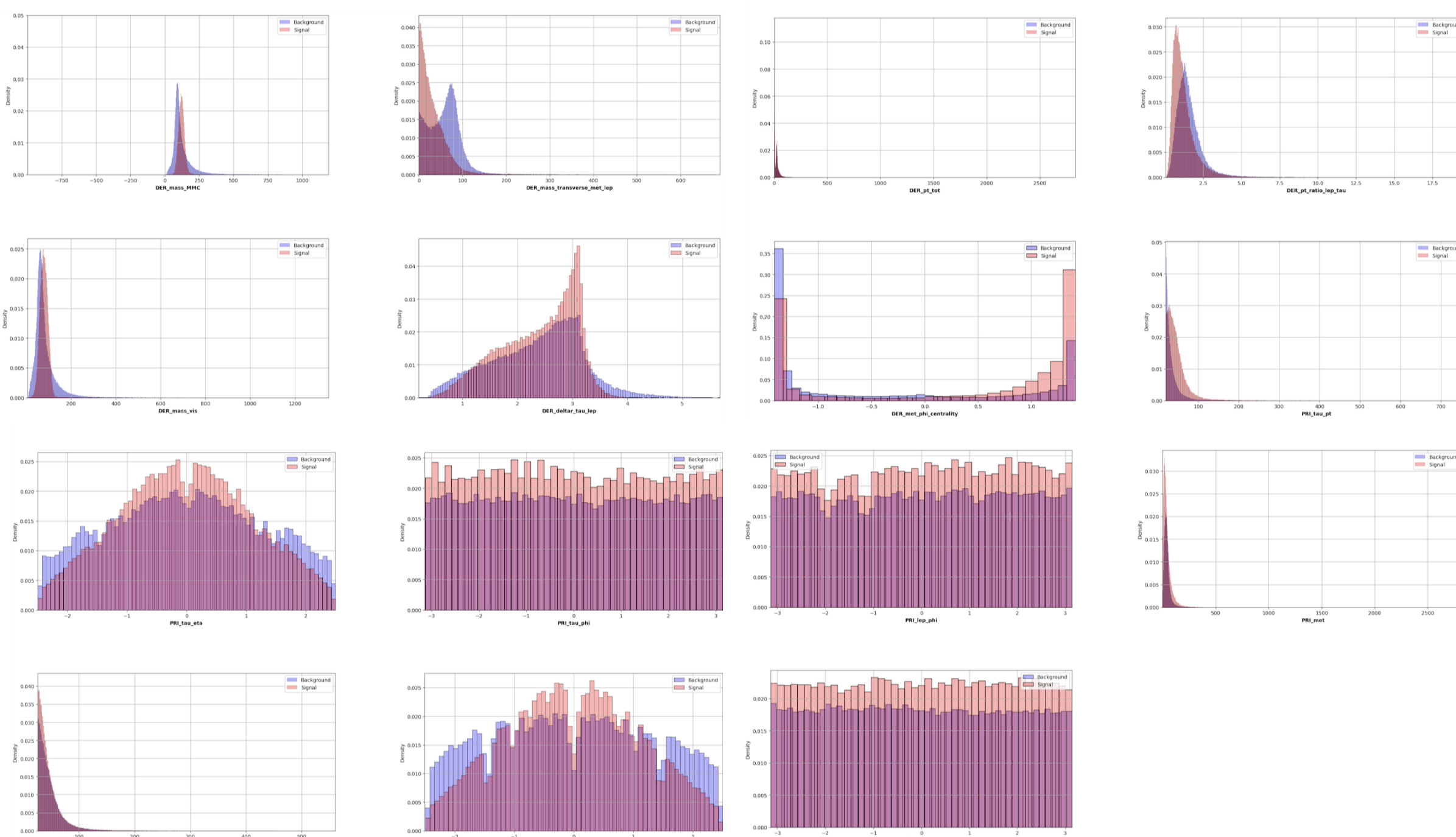
- **Data Pre-Processing:**

Data preprocessing is vital in machine learning, transforming raw data for modeling by ensuring cleanliness and consistency. In our study, we tackled multicollinearity and scaled features via Min-Max Scaling. To spot multicollinearity, we computed the Pearson correlation matrix for numeric features, where a coefficient above 0.75 flagged high correlation. Min-Max Scaling normalized feature ranges to 0-1, aiding algorithms like KNN and SVM in training efficiency and preventing bias from dominant features.
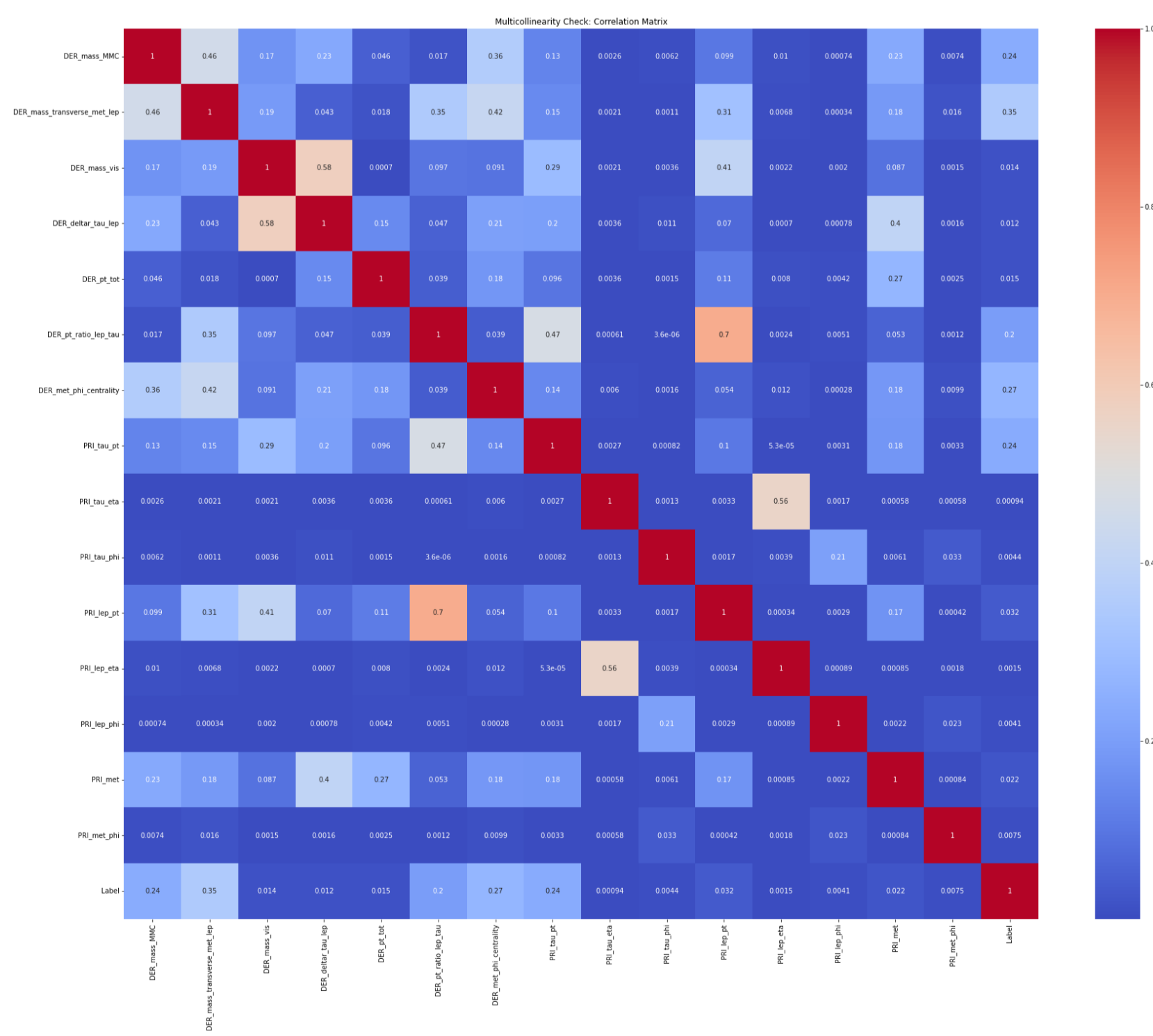
- **Machine Learning Model**

The goal of applying classification algorithms to training data is to group together pre-labeled features that are similar to one another. To achieve this goal, data training is performed using supervised learning algorithms that leverage predefined classifications within the data. This article utilizes the following classification algorithms: Logistic Regression, K-Nearest Neighbors (KNN) (Mucherino, 2009), XGBoost Classifier (Chen & Guestrin, 2016), AdaBoost Classifier, Radial Support Vector Machine (SVM), and Neural Networks. Since the best results were observed with BGBoost, AdaBoost, and radial SVM, the focus of this study was on the outcomes of these methods.
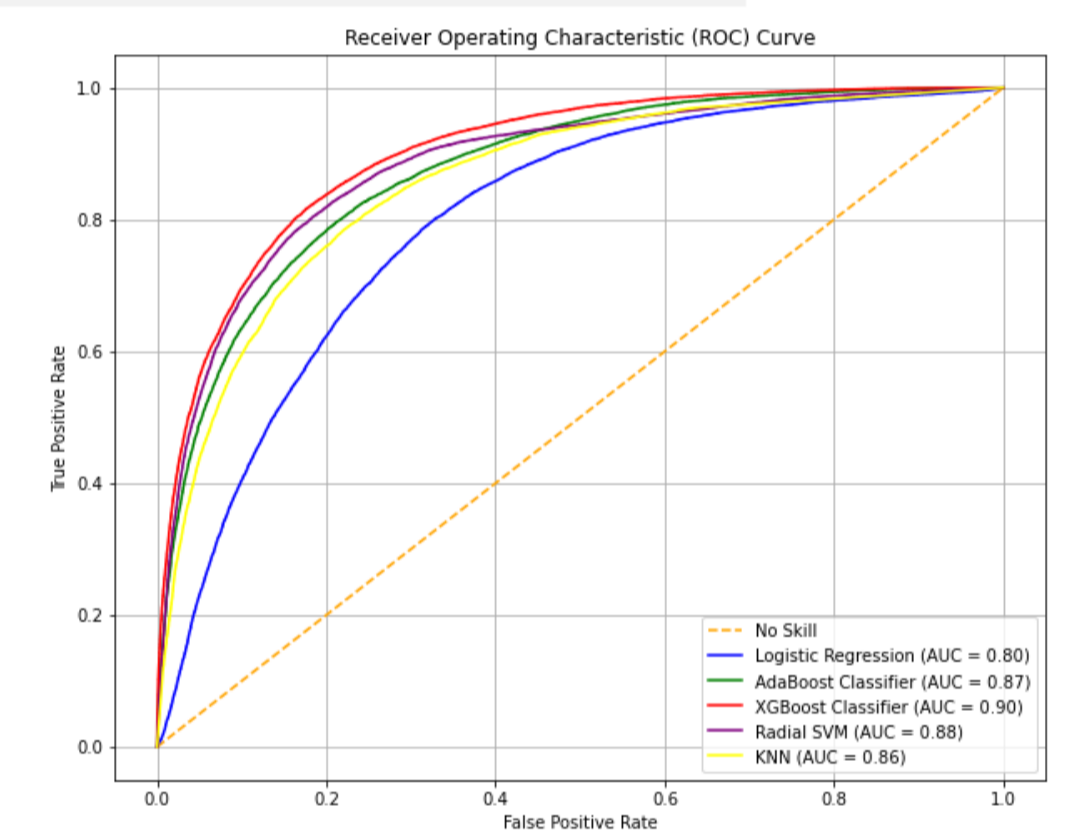
RESULTS

Various classification algorithms, including Radial SVM, Logistic Regression, KNN, XGBoost, and AdaBoost, were tested to distinguish signal from background events. Their performance was assessed using AUC scores, ROC curves, CM, and classification reports. Predictions were made using the predict_proba function from Sklearn, and models were evaluated on separate test and training datasets to check for overfitting. Cross-validation (CV) ensured statistical consistency and prevented overfitting by iteratively testing the model on different sections of the dataset.

XGBoost outperformed other methods with an AUC score **of 0.83±3.13e-3**, followed by AdaBoost and Radial SVM. Detailed performance metrics are presented in Table, separating training and testing values to assess model consistency and reliability.

Model Name	AUC Train	AUC Test	ROC Train	ROC Test	CV Train	CV Test
XGBoost	91.33	90.07	91.33	90.07	0.83±8.24e-4	0.83±3.13e-4
Logistic Reg.	80.06	79.87	80.06	79.88	0.74±2.00e-3	0.74±4.04e-3
Radial SVM	88.84	88.38	88.84	88.39	0.82±9.62e-4	0.82±2.67e-4
KNN	100	85.82	100	85.81	0.80±8.00e-4	0.80±2.61e-4
AdaBoost	87.69	87.46	87.69	87.46	0.81±6.05e-4	0.81±2.70e-4

The figure shows the **ROC curves** for the classifiers. XGBoost is the best-performing model in this study. The True Positive (TP) rate is plotted on the y-axis, while the False Positive (FP) rate is plotted on the x-axis. The area under this curve, known as the AUC value, indicates the classifier's ability to distinguish between classes. The optimal model state is illustrated where the TP rate approaches 1 and the FP rate approaches 0. Classifiers that produce curves closer to the top-left corner perform better, and in this case, the XGBoost classifier excels.

In the final step, we analyzed algorithm outcomes using the **Confusion Matrix (CM)** and classification report. The CM provides insights into TP, FP, FN, and TN results, while the classification report offers precision, recall, and F1-score metrics. Comparing these parameters helps identify models that excel in distinguishing signals from backgrounds. The XGBoost classifier showed superior performance, accurately classifying background events with high TP rates and minimal FN misclassifications. It also exhibited the lowest FP rate, indicating precise recognition of signal events from background noise, along with strong TN values, effectively predicting signals.
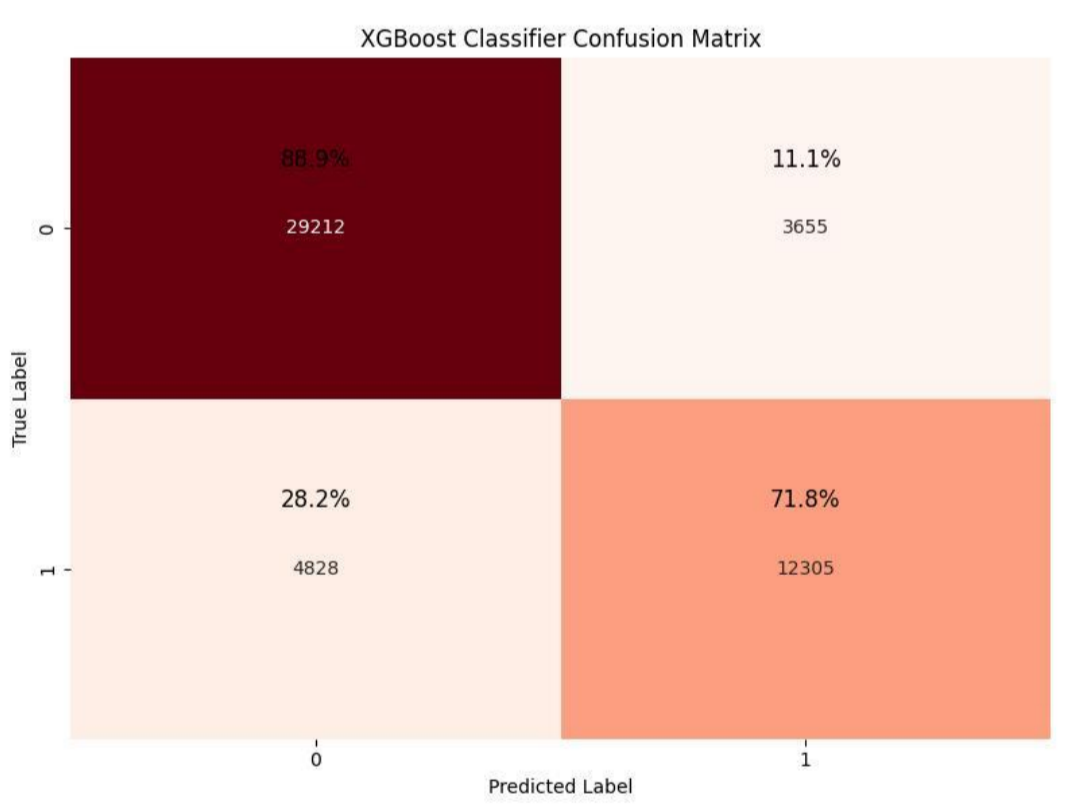
The **classification report**, shown in last Table, outlines the precision, recall, and F1-score for the XGBoost classifier. Precision gauges the accuracy of positive predictions, recall measures sensitivity or the true positive rate, and the F1-score offers a balanced measure of the classifier's performance. The XGBoost classifier excelled among all others in discerning between signal and background events. Its strong AUC score, along with superior results in the ROC curve and classification report, underscores its potent classification capabilities for this task.

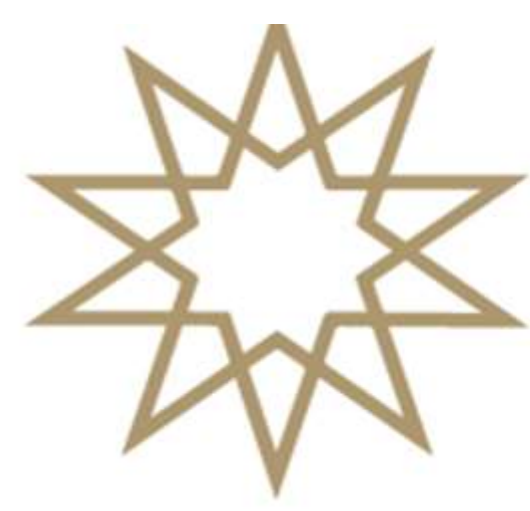|	Precision	Recall	F1-score	support
signal	0.87	0.98	0.88	32867
background	0.79	0.74	0.77	17133

CONCLUTION

This study utilizes a machine learning dataset from the ATLAS experiment to classify background and signal events, particularly focusing on Higgs boson decay into two tau particles. Various ML techniques were tested. Evaluation involved classification reports, ROC curves, and AUC scores. XGBoost emerged as the top performer, achieving the highest accuracy and stability (AUC: 0.83 ± 3.13x10^-3), followed by AdaBoost (AUC: 0.81±2.7x10^-3). This highlights the importance of selecting suitable ML algorithms in high-energy physics analysis and demonstrates XGBoost and AdaBoost's efficacy. The study also assessed models based on TP, FP, FN, and TN metrics, with XGBoost demonstrating superior efficiency in distinguishing signals from background with fewer errors. Overall, the research offers insights into leveraging machine learning for analyzing high-energy physics data.

REFERENCES

[1] Bat, A., (2023), An Educational Approach to Higgs Boson Hunting Using Machine Learning Classification Algorithms on ATLAS Open Data, doi.org/10.28979/jarnas.1242840

[2] ATLAS Collaboration. (2014). Dataset from the ATLAS Higgs Boson Machine Learning Challenge 2014. January 2022 tarihinde opendata. Open Data. Retrived January 16, 2023, from http://opendata.cern.ch/record/328.

[3] Butterworth, J.M., Davison, A.R., Salam, G.P., (2008). Jet Substructure as a New Higgs-Search Channel at the Large Hadron Collider. Phys. Rev. Lett., 100,242001. doi.org/10.1103/PhysRevLett.200.24001

YTU FEN EDEBİYAT FAKÜLTESİ

FİZİK BÖLÜMÜ

HEAVY METAL ADSORPTION WITH ZEOLITE

Muhammet Esat GÖKKAYA 19022027
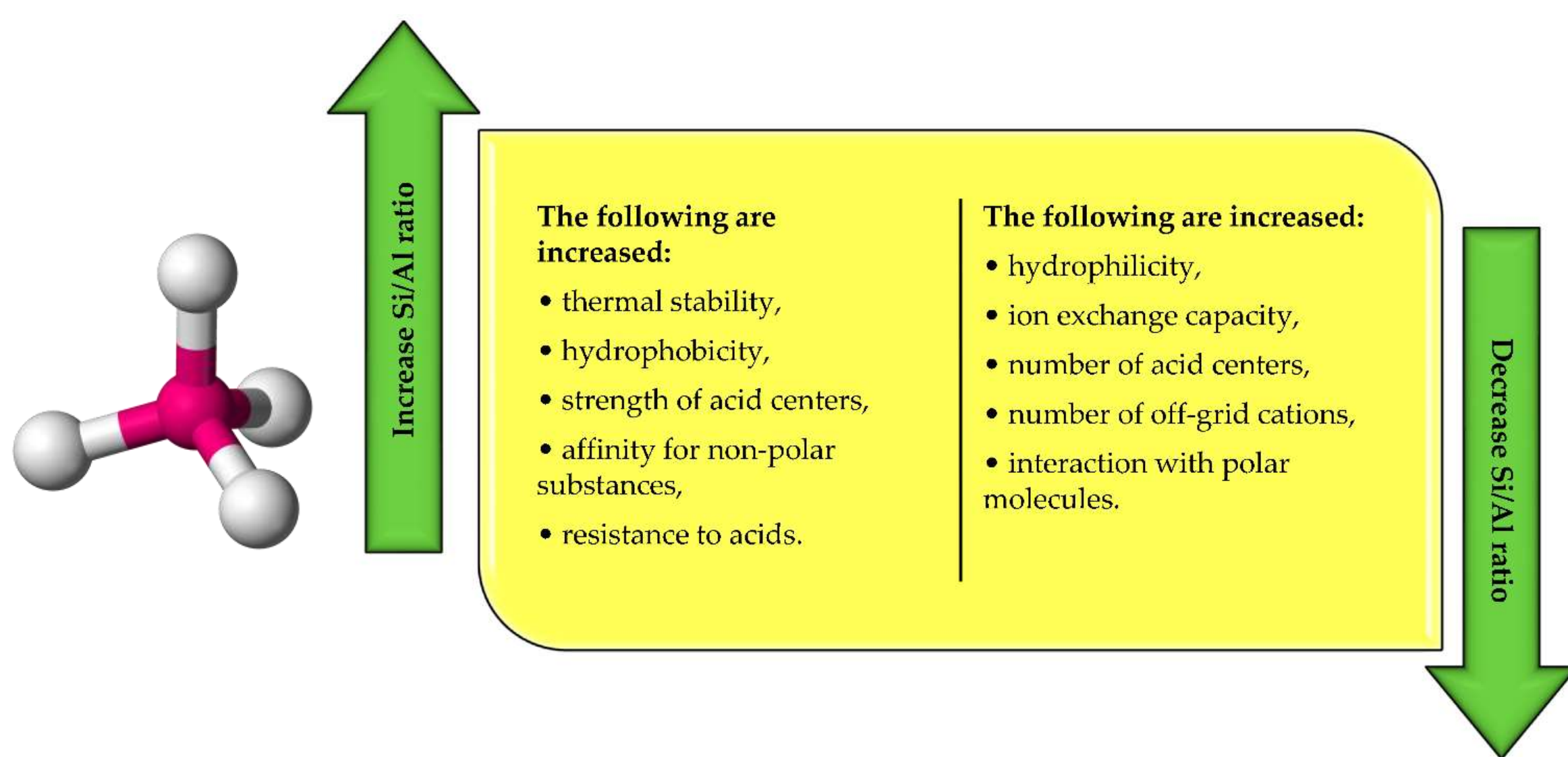
Danışman: Prof. Dr. Çiğdem NUHOĞLU

ABSTRACT

This study examines zeolites in general and the cadmium (Cd) adsorption potential of natural zeolite, known as zeolite clinoptilolite, and evaluates highly sensitive heavy metal detection, especially in liquid media. It has been determined by XRF analysis that zeolite in liquid media containing different amounts of Cd provides Cd adsorption and allows the detection of sensitive heavy metal composition. In the light of our graduation project, which is a preliminary study, it is planned to expand the work with single and multi-component solutions containing various zeolite concentrations as well as amounts of Cd atoms.

INTRODUCTION

Zeolites are volcanic aluminosilicates that are formed by the chemical attraction of volcanic tuff and contain abundant amounts of aluminum and silicon. Zeolites can also have 1A and 2A group elements like sodium, potassium, magnesium, and calcium. There are 170 different types of zeolites on our planet; however not all of them are natural zeolites. Zeolites can simply be modified in laboratories by different techniques, some of which include the alteration of their pore sizes and chemical properties. These modified versions of zeolites are known as synthetic zeolites. Zeolites includes mostly silicium (Si) and aluminum (Al) elements. The ratio of these elements plays a significant role in zeolite's thermal stability, acid resistance and hydrophobicity. The second important factor in zeolites is their framework They are fundamentally built by tetrahedron shapes of SiO_4 and AlO_4 molecules. The bond between SiO_4 and AlO_4 molecules creates an extra negative charge, leading to the attraction of ions to zeolite. Therefore, zeolites can easily absorb some ions such as magnesium (Mg^{2+}), potassium (K^+) and ammonium (NH_4^+)[1]. In this study, it is aimed to investigate ion exchange capacity of clinoptilolite for Cd^{2+} and to evaluate the process low-concentration heavy metal detection.

PHYSICAL AND CHEMICAL PROPERTIES OF ZEOLITE

SiO_4 ve AlO_4 molecules form a tetrahedron shape (a polyhedron consisting of four triangular faces) which is responsible for zeolite's crystal forms. Tetrahedrons build crystal structures as ring shaped oxygen pores. These pores have two different meanings; they can either be used as connected traps (type of absorbance and retainer) or they can be built up into homogenous tunnels. Due to these formations, zeolites are great adsorbance and catalyzer materials.

Increase Si/Al ratio

The following are increased:
• thermal stability,
• hydrophobicity,
• strength of acid centers,
• affinity for non-polar substances,
• resistance to acids.

The following are increased:
• hydrophilicity,
• ion exchange capacity,
• number of acid centers,
• number of off-grid cations,
• interaction with polar molecules.

Decrease Si/Al ratio

With the increase of Si/Al concentration, there is a noticeable improvement in zeolite's thermal stability and hydrophobic abilities. While the zeolites with lower silicon concentration may be affected by 700°C, the zeolites with higher silicon concentration can withstand temperatures up to 1300 °C and are more stable under acid conditions . When Si/Al ratio approaches 1 (indicating maximum aluminum concentration) the ion exchange capacity of zeolite reaches its maximum value [2].
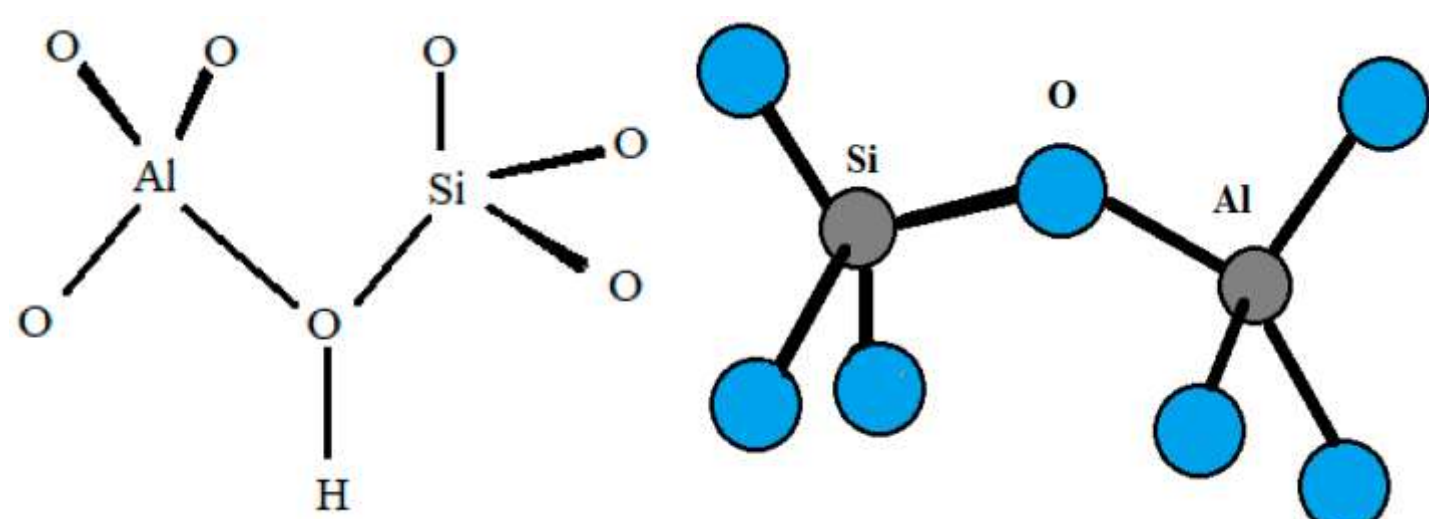

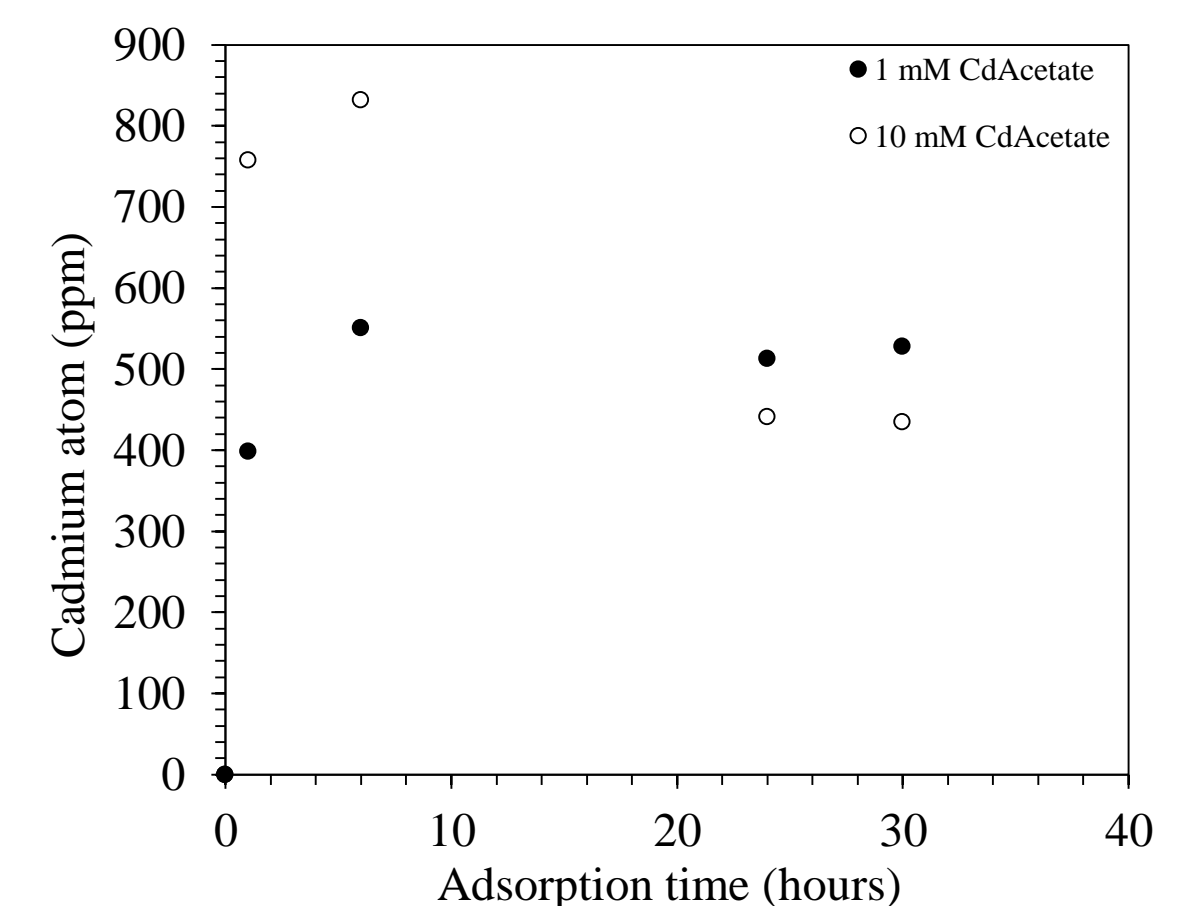## ZEOLITE CLINOPTILOLTE FOR HEAVY METAL REMOVAL

.**Experimental Method:**

Firstly, two distilled water samples of 25 mL each were prepared. Different amounts of cadmium (Cd) were added as 1mM and 10mM(millimolar) in the water solutions. The samples have been mixed at 700rpm in a magnetic stirrer for a couple of minutes in 50mL beakers. After that, 6 grams of zeolites were added to the samples. They stirred for 2 hours to 30 hours. Specific time intervals were selected as 2 hours, 6 hours, 24 hours, and 30 hours. At each of these intervals, 5ml of the solutions were collected from the samples, filtered, dried, and put in tiny tubes. Secondly, after drying process, Total of 8 different examples gathered as 2 hours 6 hours 24 hours and 30 hours for 1mM and 10mM. These examples were put in the pallet press and compressed resulting of zeolite powder pallets. After that, XRF (X-ray Fluorescence) measurements were taken of sorbents in pallets form to investigate cadmium ratio.

Results:

XRD Pattern of pure Zeolite
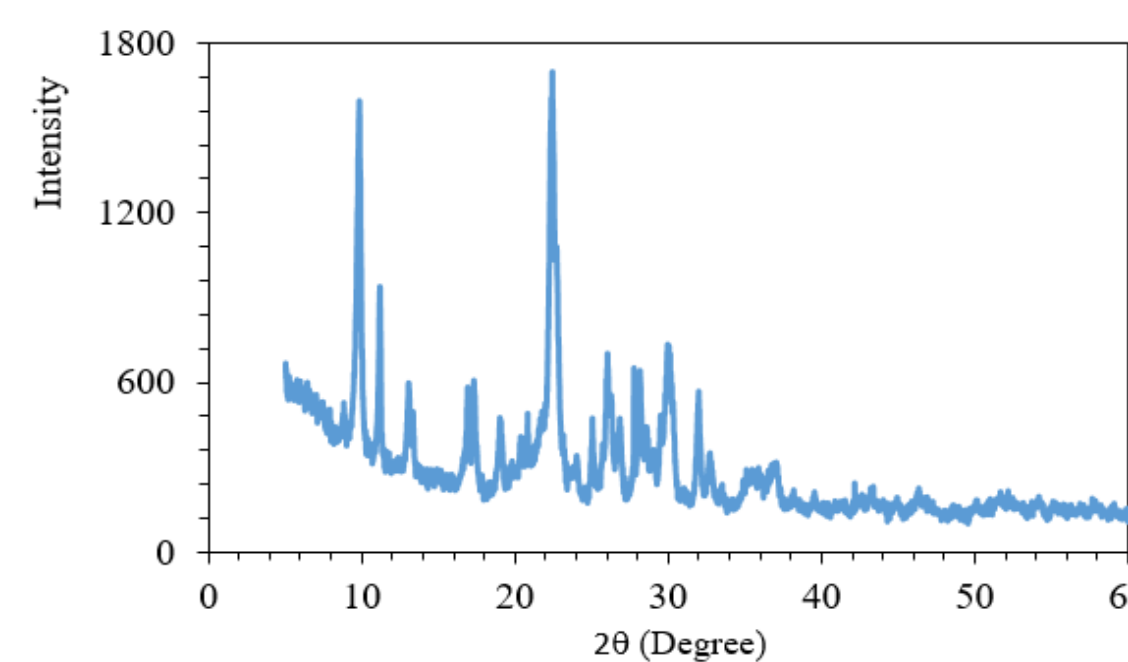
XRF data for zeolite for different cadmium adsorption time

	SiO2	Al2O3	Cd	
			ppm for 1mM	ppm for 10mM
Pure	75.484	10.929	0	0
1h			398.5	758
6h			550.8	832
24h			512.9	441
30h			527.9	435

X-ray fluorescence spectrometry analyzer.

Change in the amount of cadmium atoms attached to the zeolite material kept in 1 and 10 mM cadmium acetate solution with adsorption time
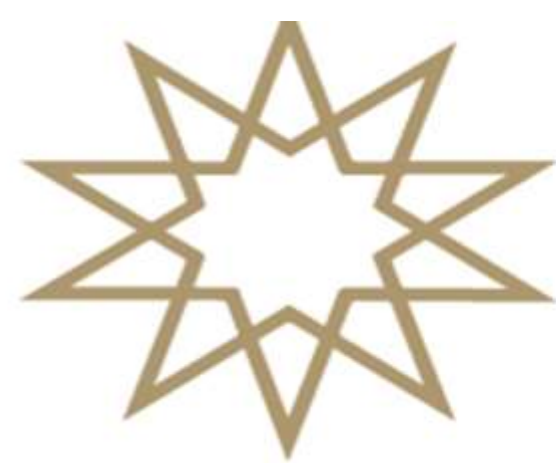
CONCLUSION

Similar to the literature, adsorption for both Cd concentrations in a single component solution was stabilized at approximately 24h about 400-500 ppm Cd [3].
According to our experimental results as a preliminary study, it was determined that this zeolite extracted from the mine in Turkey
1- Provides heavy metal retention,
2- Allows the detection of high and low heavy metal concentrations with a fixed amount of zeolite, has a distinguishing feature
3- Retention develops up to 6h for each maximum concentration, desorption begins in the following process.

REFERENCES

[1] Saltalı, K., Sarı, A., & Aydın, M. Removal of ammonium ion from aqueous solution by natural Turkish (Yıldızeli) zeolite for environmental quality. Journal of Hazardous Materials, 141(1), 258–263. (2007)
[2] Kianfar, E. Zeolites: Properties, applications, modification and selectivity.ResearchGate. (2020).
[3] Comparative and competitive adsorption of cadmium, copper, nickel, and lead ions by Iranian natural zeolite Hajar Merrikhpour • Mohsen Jalali, Clean Techn Environ Policy (2013)

2023-2024 Spring Semester

PHYSICS DEPARTMENT

Evaluation of the Efficiency of Josephson Junctions in Quantum Systems Based On Three Specific Experiments

Tunca Cem Yıldırım 20022008

Prof. Dr. Çiğdem NUHOĞLU

Abstract

Quantum Computer technology, which has been on the rise in recent years, holds great promise for the future, but it is equally important to realize that the physics behind it is not always smooth and innovative so experiments need to be conducted. In this paper, I present this research on the efficiency of Josepshon Junctions, which are critical for the operation and sustainability of quantum computers, using data from experiments tested in various laboratories. Using these data sets and the results of the experiments, the working principles, material specialization, and quantum phenomena of Josepshon Junctions are reinterpreted in terms of their efficiency and improvability on Quantum Processors composed of Josepshon Junctions. Various efficiency methods include, quantum tunneling, lithographic cutting methods and reusability and stability studies for the processors. The effects of electron beams on the processors as well as the efficiency of qubit operation are considered as the most fundamental parameter. Considering the direct performance impact of nanochips and nanoscopic adjustments and refinements in quantum systems, the production of JJs with various materials and the formation of Cooper Pairs as a result of changing the grain boundary structures of these materials with various laser-hardening methods and the reproducibility and reusability of JJs are considered.
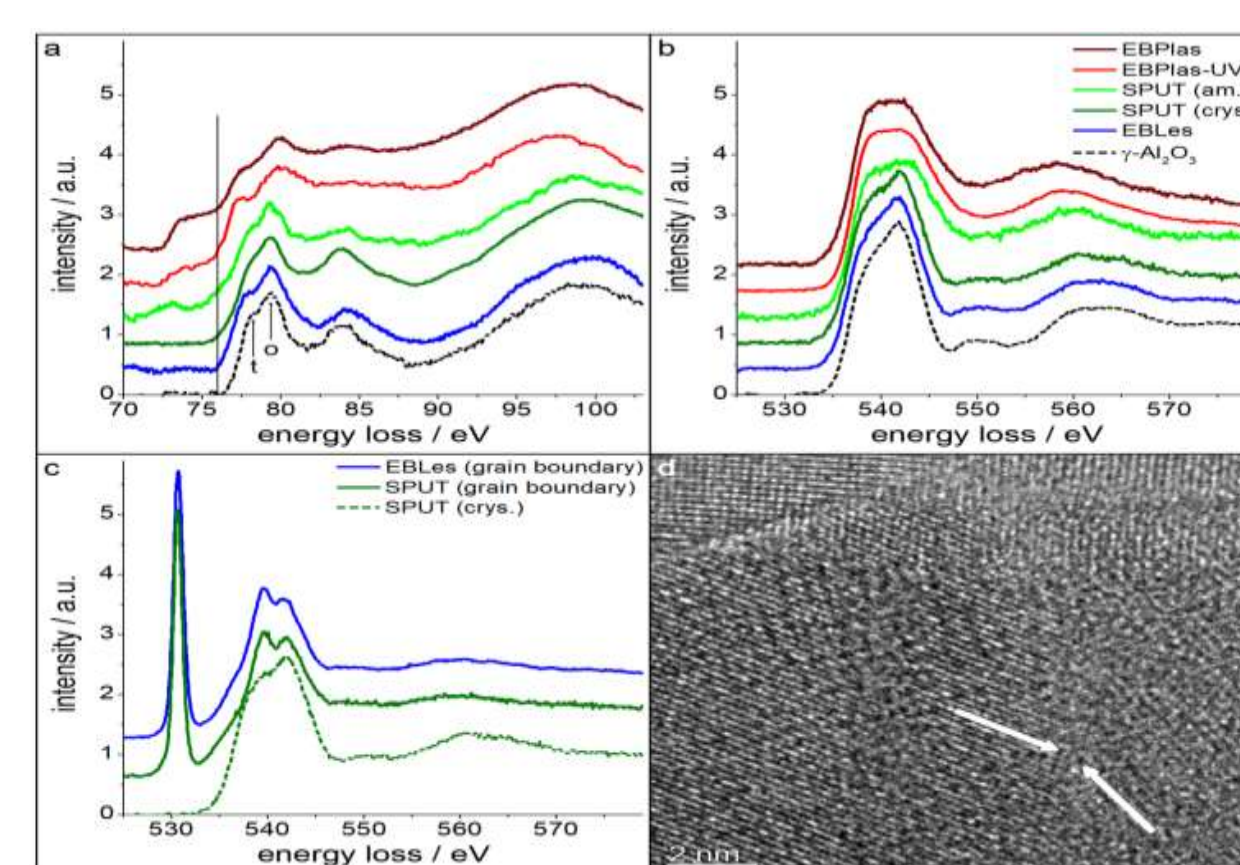
Quantum Computers and Classical Computers

Qbit is the smallest information storage unit of quantum information in quantum computers (Quantum bit). It is the bit equivalent in the classical computer.In the classical case, a bit must be either in state 1 or in state 0.A Qbit is a two-level quantum mechanical systemIt allows two levels of spin up and spin down such that the electron's spin and Qbit can be in a consistent superposition of both states. This is one of the fundamental parameters of quantum computers.
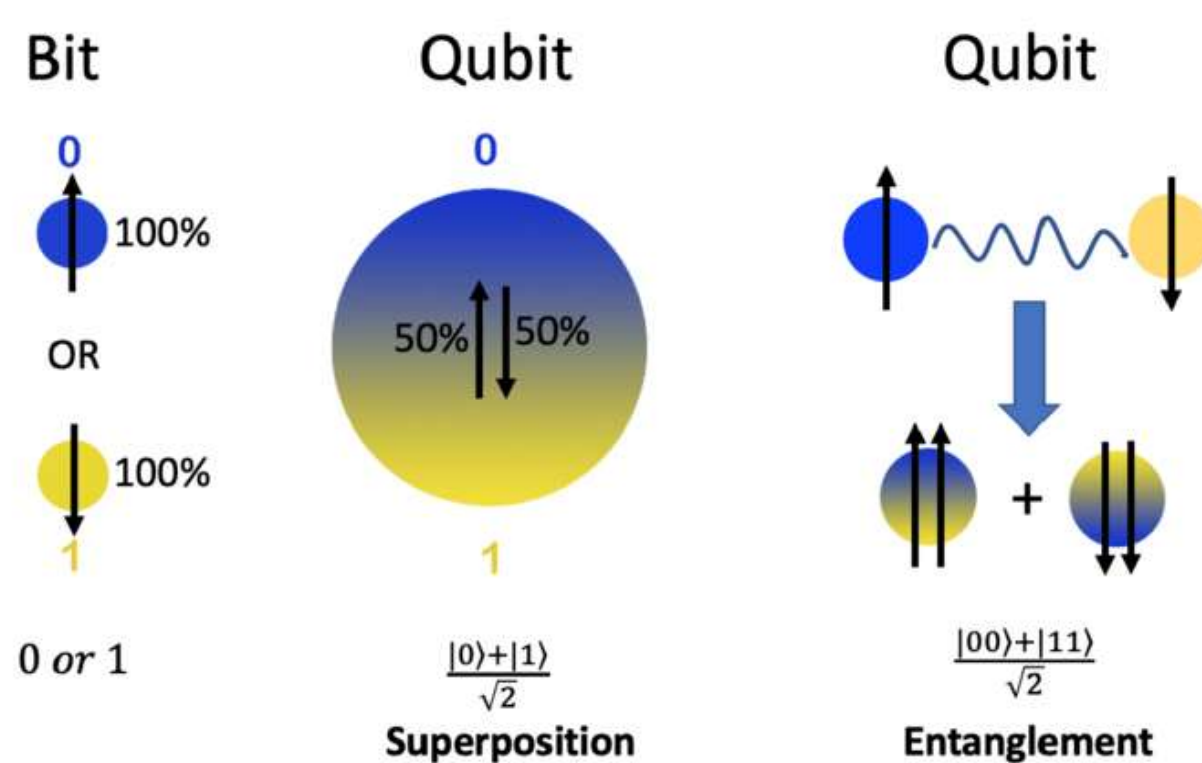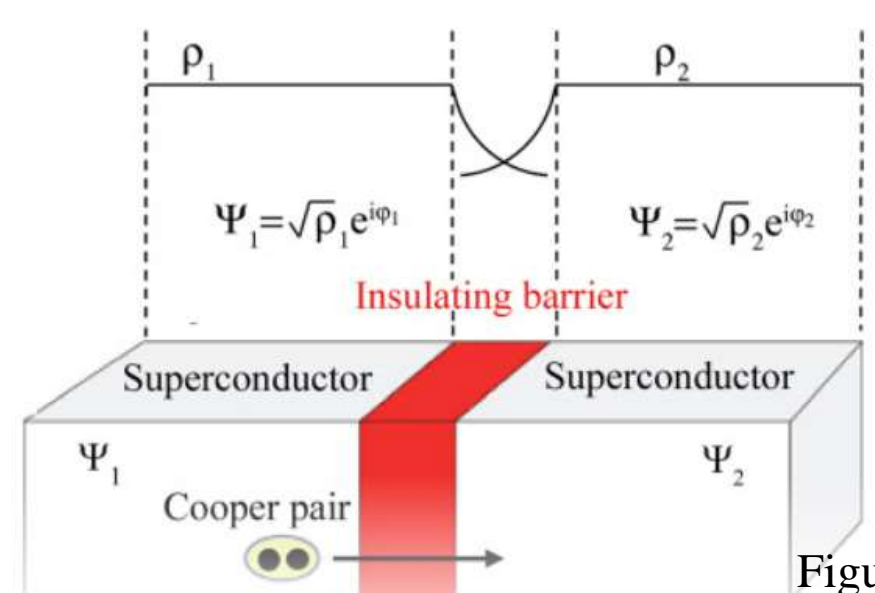
Quantum computing: A taxanomy, systematic review and future directions page 69 figure 1) [5]

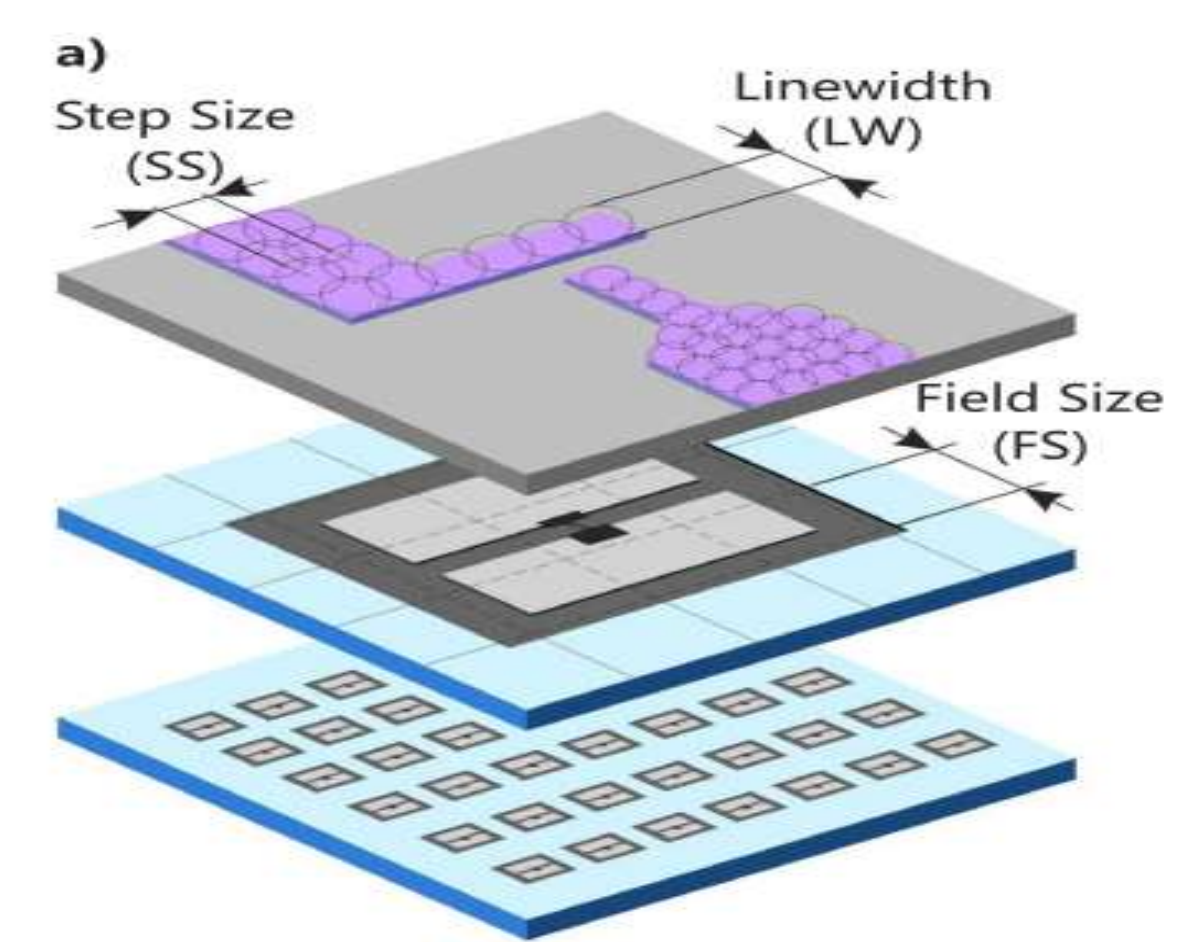## Josephson Effect & Grain Boundary Josephson Junctions

The Josephson effect was discovered by Brian Josephson in 1962. He reported that a supercurrent would occur by the tunneling effect through an insulating barrier separating two superconductors. The Josephson junction schematically consists of two superconductors separated by a thin insulating layer.

Figure Josephson junction diagram [4]

Quantum Tunnelling

Tunneling or overshooting is the phenomenon in which particles with lower excitation or excitation energy in a potential well bypass or penetrate the well. Tunneling is therefore, most pronounced in low-mass particles, such as electrons or protons, which tunnel through microscopically narrow barriers. On the other hand, some experiments have explained the absorption, i.e. the penetration of a wave function only through the barrier without conduction to the other side, which can be described as a tunneling effect, such as tunneling through the walls of a finite potential well.
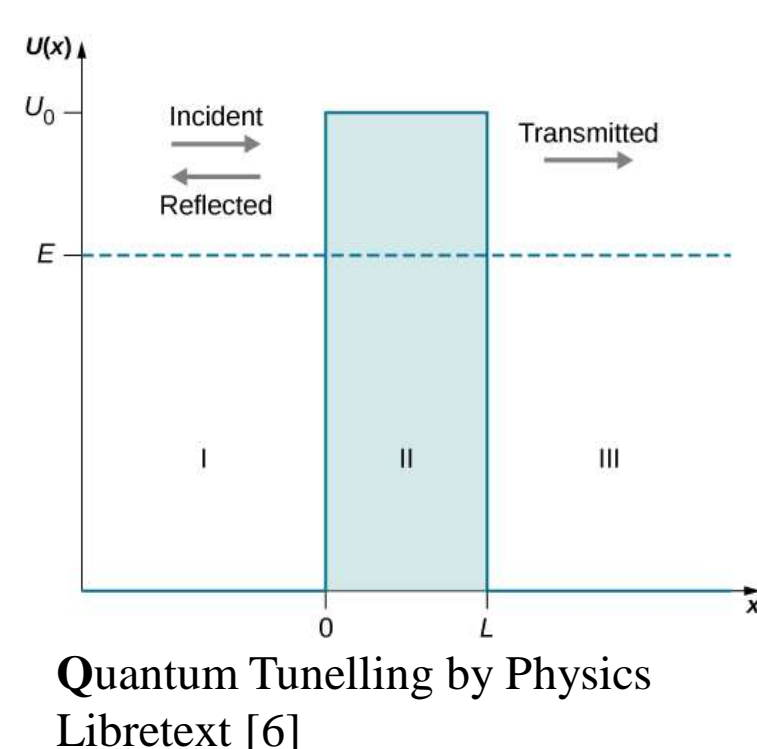
Quantum Tunnelling by Physics Libretext [6]

SQUID (Superconduction Quantum Interference Device)

The SQUID circuit element, which works under the name SQUID Principle, is actually a cyclic structure consisting of two current paths. The current is fed through the loop on one side and collected on the other side. It consists of two Josephson junction structures [7].

SQUID made from double Josepshon Junction

Two examples from R&D studies

In the study by Fritz, S, et al., an Al oxide layer was produced on the Al substrate by electron beam evaporation and sputter deposition method to increase the efficiency of qubit systems by minimizing flux noise in J-junctions and was examined using temperature-dependent dielectric and TEM measurements. In addition, laser (electron beam and electron beam + ultraviolet light) was used to densify the insulation layer during production and its effects on the structural and dielectric properties of the films were examined.

EELS spectra showing the ELNES of the Al-L2,3 and O-K edges in the AlOx-layers of all samples and a γ-Al2O3 reference specimen. Spectra of (a) Al-L2,3 and (b) O-K edges acquired in amorphous (EBPlas, EBPlas-UV and SPUT) and crystalline (EBLes and SPUT) regions. A spectrum of a crystalline γ-Al2O3 reference specimen is included. The edge onset of γ-Al2O3 (DOI:10.1038/s41598-018-26066-4) [1]

The study focuses on the reuse of electrical properties in Josephson Junctions, crucial for qubit structures, using the Ambegaokar-Baratoff formula to examine degradation and incompatibilities. The experiment highlights the impact of fabrication defects on electrical performance in small volumes. Variations in resistance were measured in different fields using $Al/AlO_x/Al$ Josephson Junctions. Evaporation systems were identified as the main obstacle to reusing electrical factors. Tests on non-linear and asymmetric elements in high-speed superconducting transmons were conducted to analyze different fabrication patterns.

$$I_c = \frac{\pi\Delta}{2eR_n}$$

Ambegaokar-Baratoff Formula

$$\sigma_f = \frac{\sigma_r}{2\langle R\rangle}\cdot\langle f\rangle$$

Frequency Deviation

Discussion

The evaluations of the three experiments essentially lead us to the final and fatal flaws for Josephson Junctions: dielectric, resistance and critical current, which depend on these parameters. I_c emphasizes how important this value is for Qubits. Not only these three experiments, but also other quantum system and telecom research, the development of structures at these nanometric sizes is important for both material sciences and lithographic processes for chip structures in order to further increase the efficiency of these systems.In addition, research continues on which laser editing methods should be used in order to make a definitive judgment about which of these quantum phenomena compatible with superconductivity will be the most compatible grain boundary jj.Studies on the main materials and combinations of layers, their nanostructures, their formation methods, and their improvement with post-formation processes have been the focus of great attention in the literature.
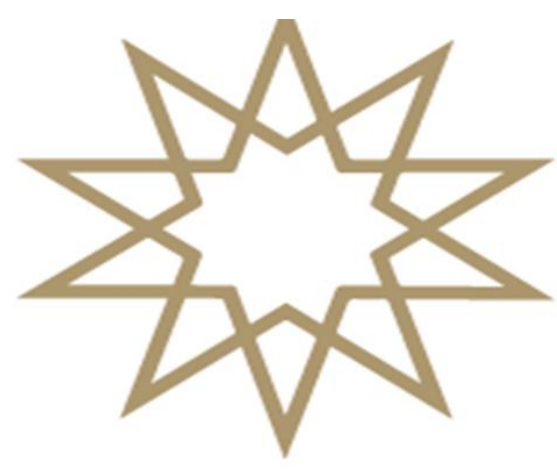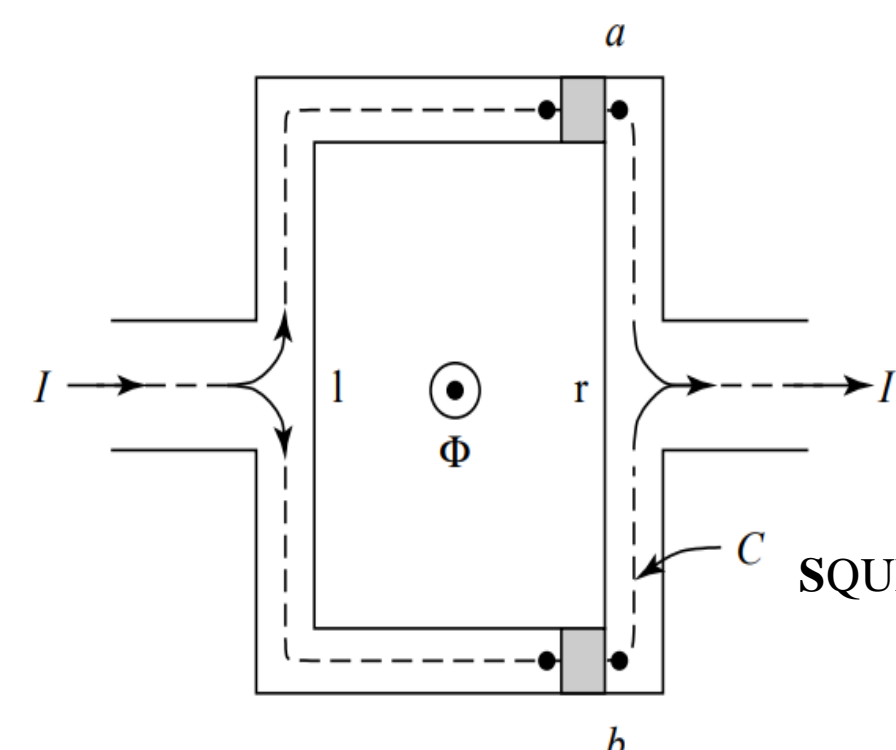
References

[1] Fritz, S., Seiler, A., Radtke, L. et al. Correlating the nanostructure of Al-oxide with deposition conditions and dielectric contributions of two-level systems in perspective of superconducting quantum circuits. Sci Rep 8, 7956 (2018). https://doi.org/10.1038/s41598-018-26066-4

[2] Hertzberg, J.B., Zhang, E.J., Rosenblatt, S. et al. Laser-annealing Josephson junctions for yielding scaled-up superconducting quantum processors. npj Quantum Inf 7, 129 (2021). https://doi.org/10.1038/s41534-021-00464-5

[3] Pishchimova, A.A., Smirnov, N.S., Ezenkova, D.A. et al. Improving Josephson junction reproducibility for superconducting quantum circuits: junction area fluctuation. Sci Rep 13, 6772 (2023). https://doi.org/10.1038/s41598-023-34051-9

[4] Superconducting quantum magnetic sensing Antonio Vettoliere, Paolo Silvestrini, Carmine Granata, Quantum Materials, Devices, and Applications,2023, Pages 43-85

[7] https://www.researchgate.net/figure/Illustration-of-a-bit-and-qubit-Left-A-bit-can-take-a-value-of-0-or-1-with-100_fig5_344971320

[6] https://phys.libretexts.org/Bookshelves/University_Physics/University_Physics_(OpenStax)/University_Physics_III_-_Optics_and_Modern_Physics_(OpenStax)/07%3A_Quantum_Mechanics/7.07%3A_Quantum_Tunneling_of_Particles_through_Potential_Barriers

[7] Kristian Fossheim, Asle Sudboe,Superconductivity: Physics and Applications, John Wiley & Sons, 2005,ISBN 047002643X, 9780470026434

YTU FEN EDEBİYAT FAKÜLTESİ

Department of Physics

NEUTRINO OSCILLATION

Student İbrahim ELÇABUK 19022048

Supervisor: Prof. Dr. Kutsal BOZKURT

Abstract

In the Standard Model, neutrinos are massless, but we have learned that in the last 50 years, through developing technologies and physics, neutrinos have mass [2]. This idea that started with B. Pontecorvo, gained much more importance in 60's [7]. In the following years some experiments have been done [9]. They were supportive to neutrino oscillation. Some of them are Homestake Experiment, Kamiokande and Super-K [8,9]. Nowadays we know that neutrino flavor eigenstates are connected to neutrino mass eigenstates with UPMS Unitary Matrix. While Neutrinos are moving through space, their mass eigenstates oscillate depending on length, energy and flavors [1].

History Of Neutrinos

Neutrinos are massless, ½ spin, chargeless and left-handed particle according to Standard model [1]. But recent 50 years neutrinos were observed that they should have mass even if its mass small [2]. Neutrinos was started to notice after 1900s with discovery of beta decays [3]. In beta decays, electrons have continually energy spectrum. This situation violated the law of conservation of energy without neutrinos hypotheses [4]. In 1930, W. Pauli proposed a massless, uncharged, weakly interacting particle with a spin of ½. Enrico Fermi later named this particle "Neutrino" [5]. In nuclear physics, beta decay occurs as follows:

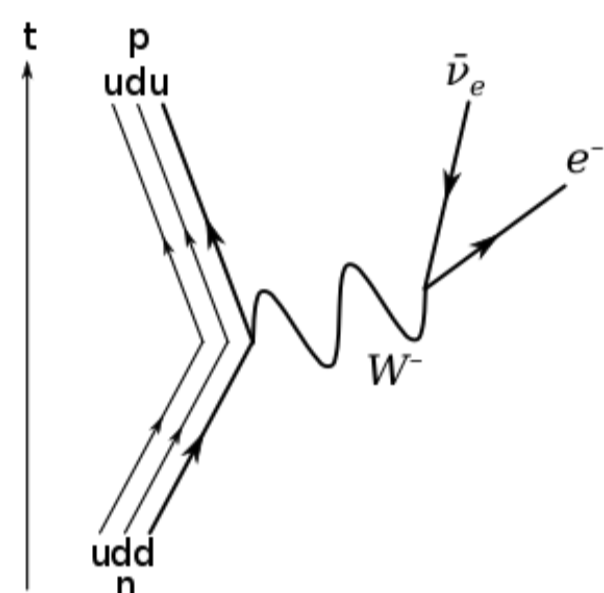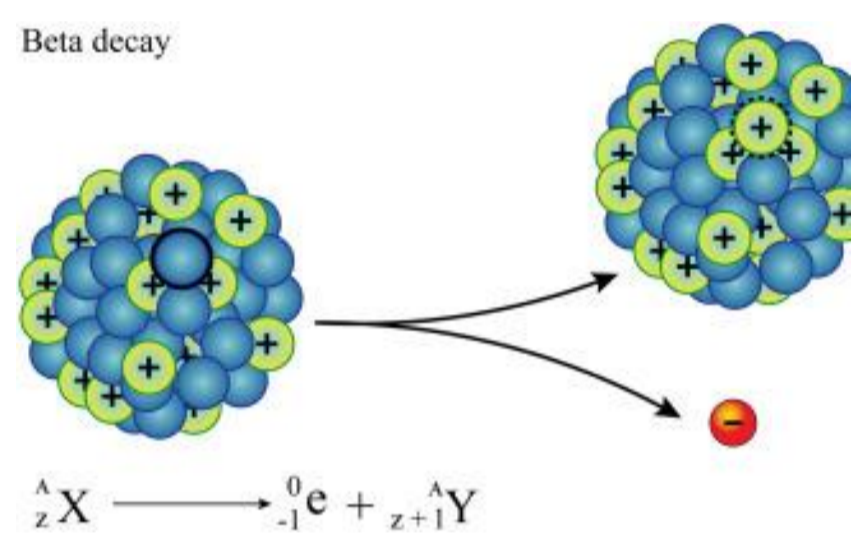Figure 1 Feyman diagram of beta decay [10]

Figure 2 Beta decay in nucleus [11]

How Were Neutrinos Detected?

In the Cowan–Reines neutrino experiment, neutrons and positrons were expected to emerge as a result of the anti-neutrino hitting the proton predicted by the inverse beta decay equation [6].

$$\bar{v} + p \rightarrow n^0 + e^+ \quad (1)$$

The resulting positron combines with an electron and emits 2 Gamma rays with 511 keV's of energy. The neutron combines with the Gd nucleus and emits between one to four gamma rays [6]. The neutrino discovered in the Cowan– Reines Neutrino Experiment was understood to be an electron neutrino due to lepton conservation [7]. Therefore, it is thought that the presence of a muon neutrino in muon decays was required In the early 1960s, muon neutrinos were discovered independently at CERN and Brookhaven National Laboratory [8]
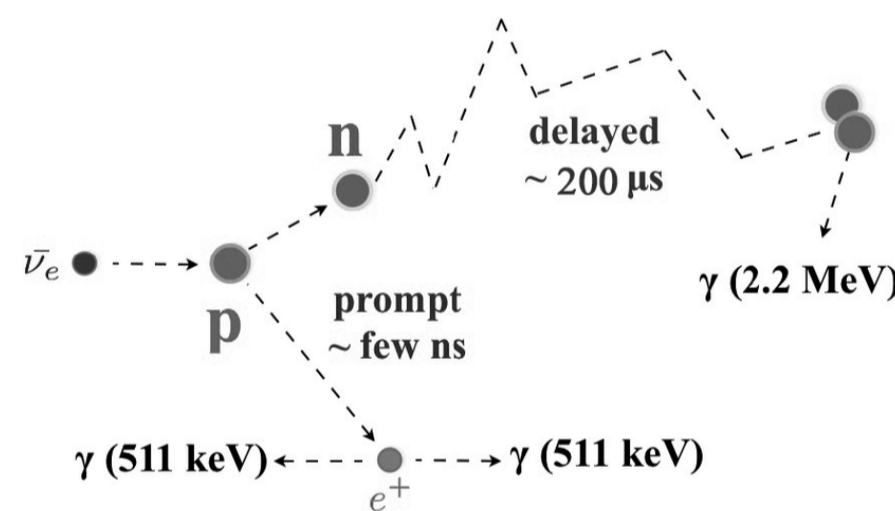
Figure 3 Inverse beta decay [12]

Pion Decay:

$$\pi^+ \rightarrow \mu^+ + v_\mu \quad (2)$$

Muon Decays:

$$\mu^+ \rightarrow e^+ + v_\mu + \bar{v}_e \quad (3)$$
$$\mu^+ \rightarrow e^- + v_\mu + \bar{v}_e \quad (4)$$

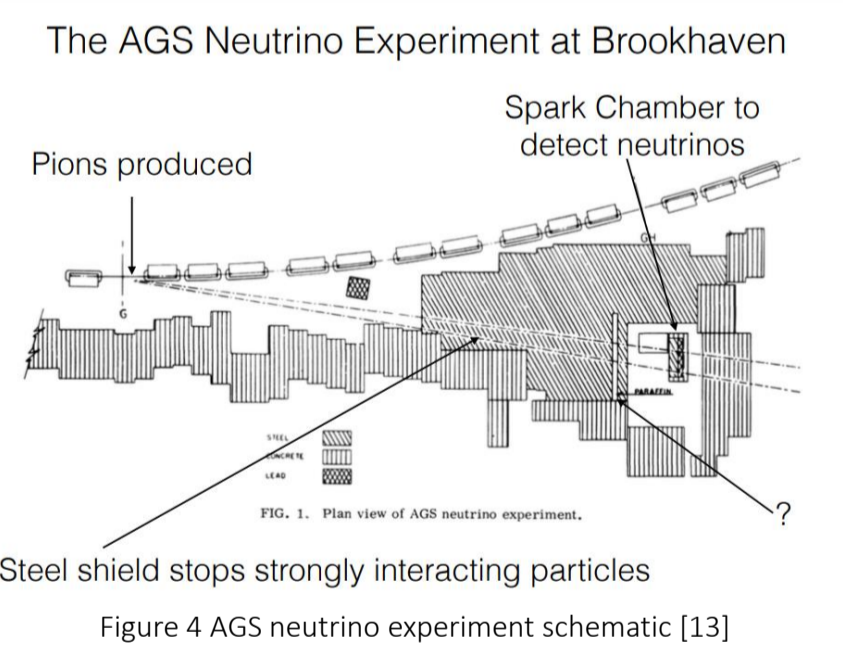The AGS Neutrino Experiment at Brookhaven

Figure 4 AGS neutrino experiment schematic [13]

By 1975, with the discovery of the tau particle in the third lepton family predicted by the Standard model, the existence of a neutrino that would accompany it was accepted. In the 2001 DONUT experiment, the tau neutrino was discovered experimentally [9].

Neutrino Oscillation

Electron neutrinos are released as a result of fusion reactions occurring in the sun. These neutrinos are called solar neutrinos. Neutrino oscillations were first encountered in 1968 when R. Davis measured solar neutrinos with the Chlorine detector. To detect the high amounts of neutrinos formed in the Sun, Davis indirectly measured them with a tank detector filled with chlorine gas installed in the Homestake Mine in South Dakota, USA [5].
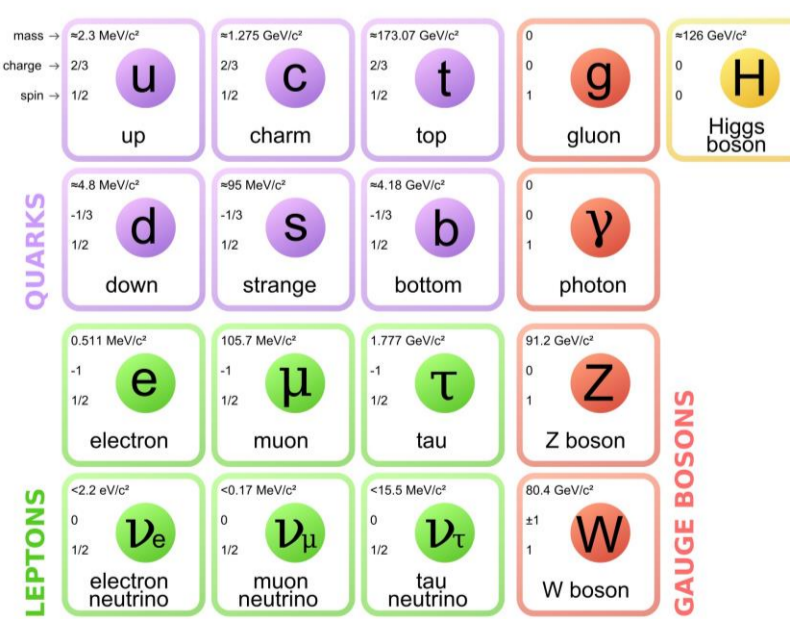
Figure 5 Elemntary particle in Standart Model [14]

The reactions in the Homestake experiment are as follows;

- $Cl^{37} + v_e \rightarrow Ar^{37} + e^- \quad (4)$
- $Ar^{37} \rightarrow Cl^{37} + e^+ + v_e \quad (5)$

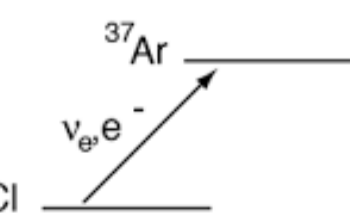Chlorine neutrino reaction as a path to neutrino detection

Figure 6 Homestake Experiment decay chain [15]

The main idea here is to observe the anti-electron.

Only a few Argon atoms were expected to be formed per day.The amount of Argon atoms produced per day were consistently very close to one-third of Bachall's calculations [2].

The results of the Homestake experiment indicated one of three conclusions:

- The experiment was not match.
- The Standard Solar Model was not match.
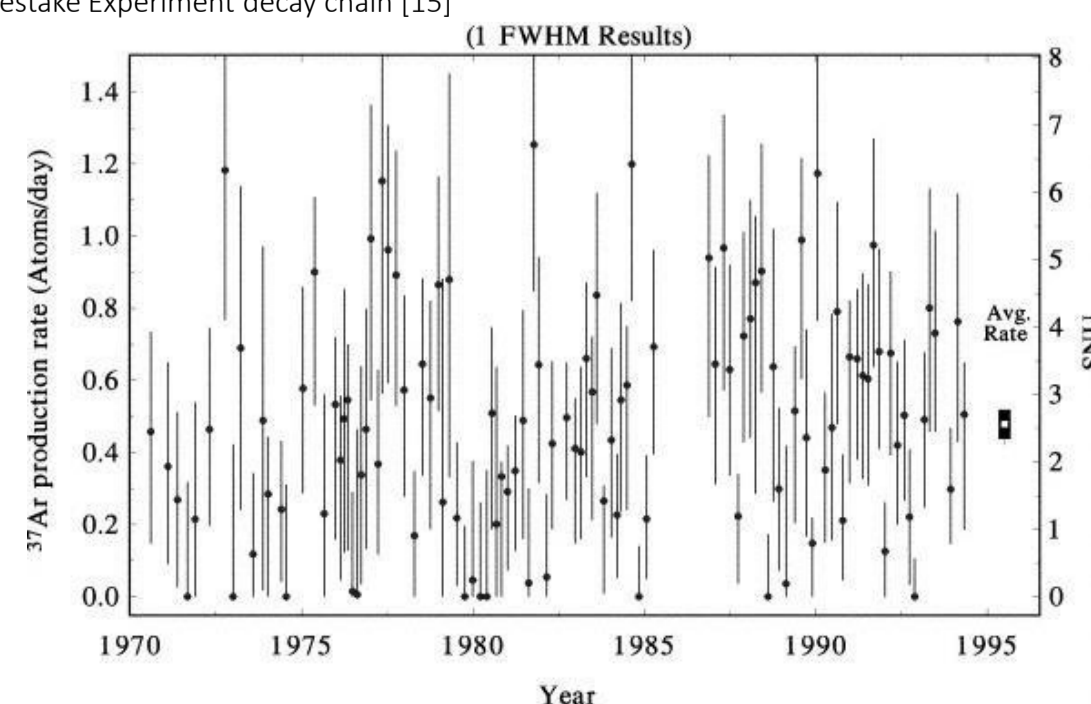- The Standard Model was not match.

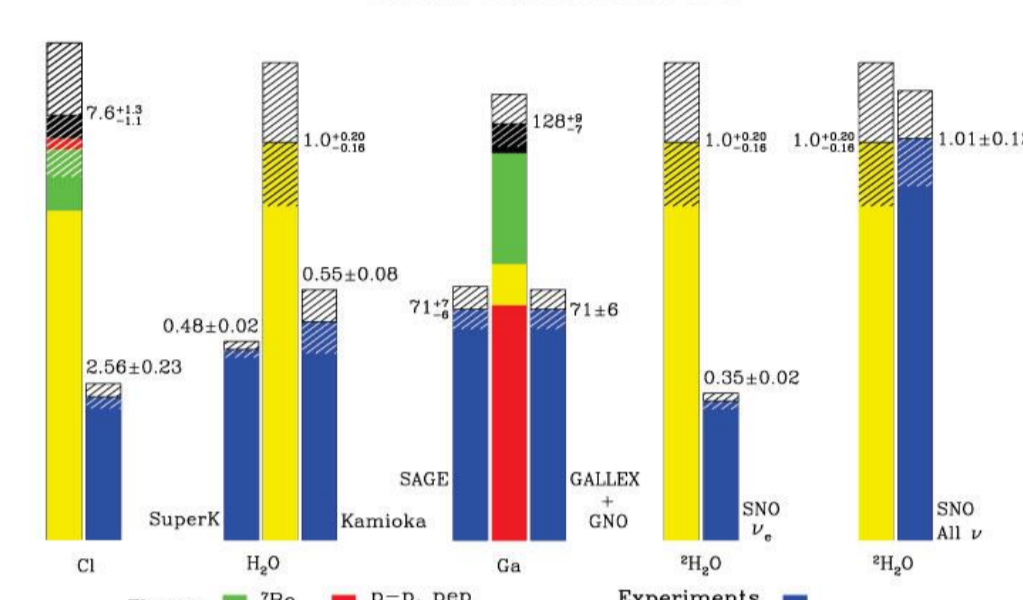Figure 7 Homestake Experimet rate of event per day [15]

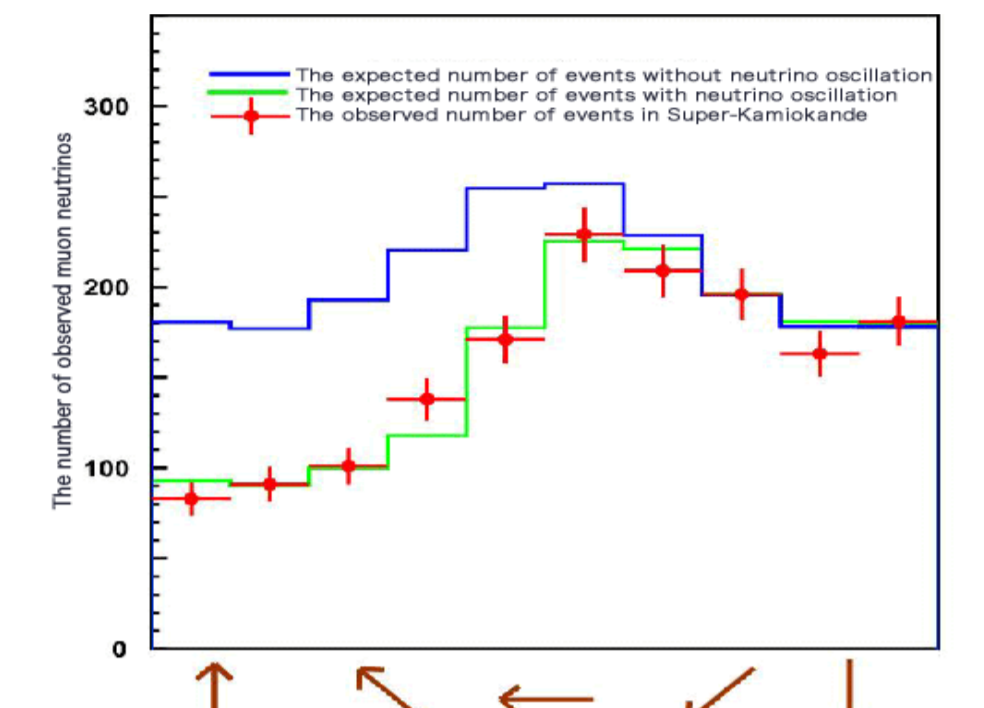Figure 8 Experiments vs theory [sns.ias.edu]

Figure 9 Super – K Experiment results vs theories [Murayama, H. (2006). Origin of neutrino mass]

In 1958, Bruno Pontecorvo introduced the idea of neutrino oscillation. According to Bruno, electron neutrinos were turning into muon neutrinos. Theory-experiment harmony was achieved in the Super-Kamiokande experiments conducted in 1998-2001 [7].

Formulation Of Neutrino Oscillation:
Neutrino Oscillation for the Two-Flavor Case

B. Pontecorvo put forward the idea that neutrinos oscillate just like neutral kaons in 1968. Kaon oscillation can be expressed in short as the following; [7]

$$K^0 \leftrightarrow \bar{K}^0 \quad (6)$$

According to this theory, neutrinos should have mass. However, the Standard Model considers neutrinos to be massless. [1,2]

The eigenstate probability, which we know from quantum mechanics, is given as follows;

$$P = |\langle v_l | v_j \rangle|^2 \begin{cases} i = j & 1 \\ i \neq j & 0 \end{cases} \quad (7)$$

The flavor eigenstates of neutrinos are defined as a linear superposition of their mass eigenstates;

$$|v_\alpha\rangle = \sum_j U_{\alpha j} |v_j\rangle \quad (8) \text{ here is } \alpha = e, \mu, \tau \quad j = 1,2,3$$

$|v_\alpha\rangle$ flavor eigenstate

$|v_j\rangle$ mass eigenstate

U is the unitary mixture matrix. (Pontecorvo–Maki–Nakagawa–Sakata matrix).

$$v_\alpha(t) = cos\theta|v_j(t)\rangle + sin\theta|v_k(t)\rangle \quad (9)$$
$$v_\beta = -sin\theta|v_j\rangle + cos\theta|v_k\rangle \quad (10)$$
$$sin^2\theta \, sin^2((m_k^2 - m_j^2)\frac{L}{4E}) \quad (11)$$

Oscillation probability is between 0 and 2π.
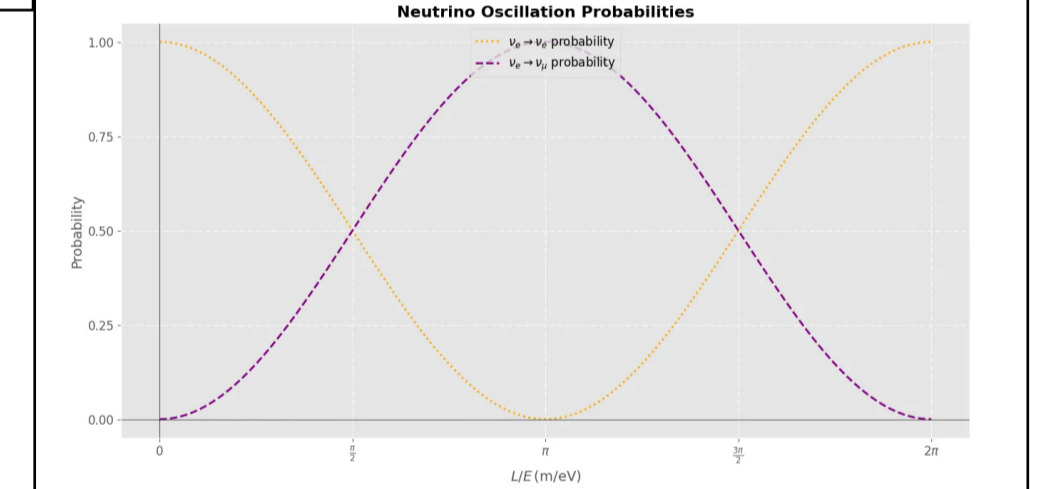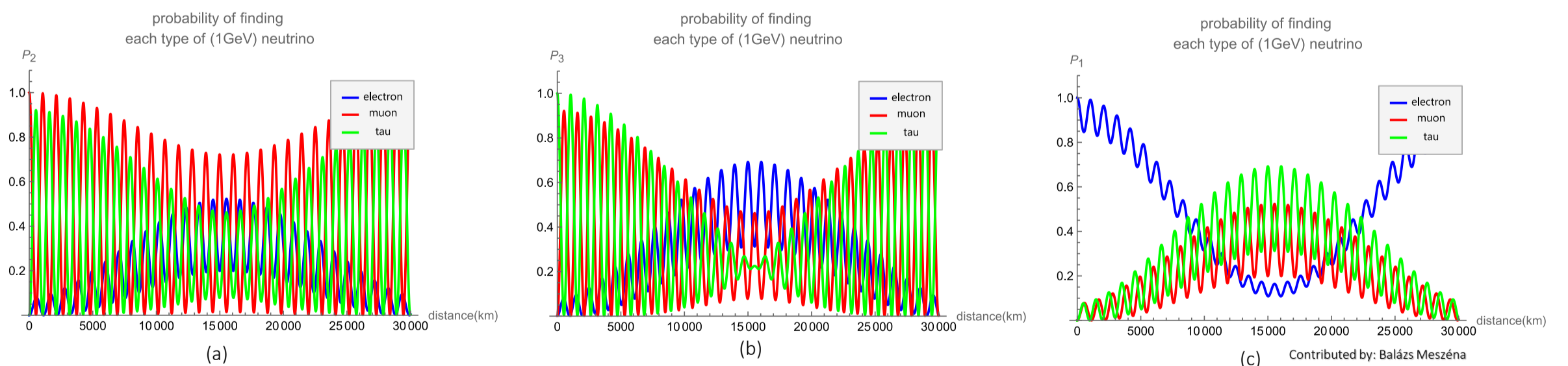
Figure 10 Two flavor neutrino oscillation graphic

Three-Flavor Neutrino Oscillation

$$\begin{pmatrix} v_e \\ v_\mu \\ v_\tau \end{pmatrix} = U_{PMNS} \begin{pmatrix} v_1 \\ v_2 \\ v_3 \end{pmatrix} \quad (12)$$

$$i \neq j \; i,j = 1,2,3 \; c_{ij} = cos\theta_{ij}$$
$$s_{ij} = sin\theta_{ij}$$

$$P(v_\alpha \rightarrow v_\beta) = -4 \sum_{k>j} Re[U_{\alpha k} U_{\beta k}^* U_{\alpha j}^* U_{\beta j}] sin^2(\frac{\Delta m_{kj}^2}{4E} t) \quad (13)$$

$$U_{PMNS} = \begin{pmatrix} c_{12}c_{13} & s_{12}c_{13} & s_{13}e^{-i\delta} \\ -s_{12}c_{23} - c_{12}s_{23}s_{13}e^{i\delta} & c_{12}c_{23} - s_{12}s_{23}s_{13}e^{i\delta} & s_{23}c_{13} \\ s_{12}s_{23} & -c_{12}c_{23} - s_{12}s_{13}e^{i\delta} & c_{23}c_{13} \end{pmatrix} \quad (14)$$

probability of finding each type of (1GeV) neutrino

(a) (b) (c)

Contributed by: Balázs Meszéna
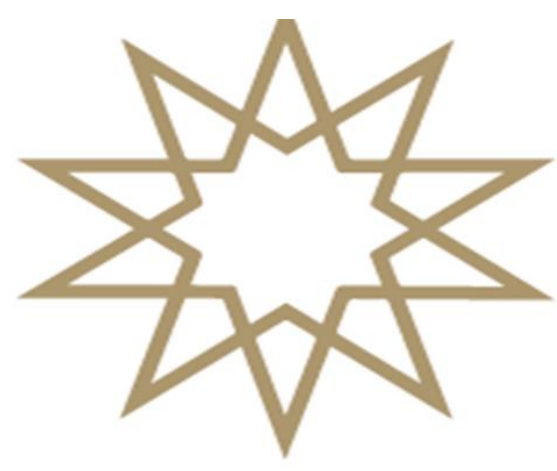
demonstrations.wolfram.com/NeutrinoOscillations

Conclusion

Neutrino oscillations indicate that neutrinos have mass, even if very small, and that their mass eigenstates are related to their flavors through linear superposition with a unitary matrix. As neutrinos travel through empty space, they undergo quantum mechanical oscillations [1]. Neutrinos gained importance in the early 1900s. In 1914, the discovery of beta decay and the continuous distribution of energy suggested a violation of energy conservation [3,4]. This issue was resolved in the 1930s with W. Pauli's proposal of the neutrino [1]. In 1968, R. Davis's Homestake Experiment revealed the "solar neutrino problem," where the measured number of neutrinos from the Sun was significantly lower than theoretical predictions. Davis and his team detected only about one-third of the expected neutrinos, suggesting either incorrect calculations of neutrino production in the Sun or incomplete understanding of neutrino properties. This led to the development of the neutrino oscillation theory, proposing that neutrinos could transform between different types or "flavors" as they traveled, implying they must have mass [2]. In 2001, experiments at Super-Kamiokande resolved the solar neutrino problem by confirming that neutrinos oscillate and have mass [9]. This discovery was a significant milestone in particle physics and cosmology, deepening our understanding of the universe's fundamental building blocks. Neutrinos continue to play a crucial role in the study of dark matter, supernova explosions, and early universe processes [1].

SOURCES

[1] Bilenky, S. M. (2015). Neutrino in Standard Model and beyond. Physics of Particles and Nuclei, 46, 475-496. [2] Murayama, H. (2006). Origin of neutrino mass. Progress in Particle and Nuclear Physics, 57(1), 3-21. [3] Burcham, W. E. (1983). Rutherford and beta decay. Rutherford memorial lecture, 1983. Proc. R. Soc. London, Ser. A.(United Kingdom), 389(1797). [4] Ellis, C. D., & Wooster, W. A. (1927). The continuous spectrum of β-rays. Nature, 119(2998), 563-564. [5] Bilenky, S. M., & Petcov, S. T. (1987). Massive neutrinos and neutrino oscillations. Reviews of Modern Physics, 59(3), 671. [6] Anderson, E. C. (1997). The Reines-Cowan Experiments. Los Alamos Science, 25. [7] Pontecorvo, B. (1968). Neutrino experiments and the problem of conservation of leptonic charge. Sov. Phys. JETP, 26(984-988), 165. [8] Aliu, E., Andringa, S., Aoki, S., Argyriades, J., Asakura, K., Ashie, R., ... & Yamada, S. (2005). Evidence for muon neutrino oscillation in an accelerator-based experiment. Physical Review Letters, 94(8), 081802. [9] Kodama, K., Ushida, N., Andreopoulos, C., Saoulidou, N., Tzanakos, G., Yager, P., ... & DONut Collaboration. (2001). Observation of tau neutrino interactions. Physics Letters B, 504(3), 218-224.[10] Ivanov, A. N., Höllwieser, R., Troitskaya, N. I., Wellenzohn, M., & Berdnikov, Y. A. (2017). Precision theoretical analysis of neutron radiative beta decay to order O (α 2/π 2). Physical Review D, 95(11), 113006. [11] Koreshi, Z. U. (2022). Nuclear Engineering: Mathematical Modeling and Simulation. Academic Press [12] Kumaran, S., Kroon, S. I., Ludhova, L., Penek, Ö., Redchuk, M., & Bagdasarian, Z [13] Schwartz, M. (1989). The first high-energy neutrino experiment. Reviews of Modern Physics, 61(3), 527.[14] cmsexperiment.web.cern.ch [15] hyperphysics.phy-astr.gsu.edu [15] Davis, R. (1994). A review of the Homestake solar neutrino experiment. Progress in Particle and Nuclear Physics, 32, 13-32

PHYSICS DEPARTMENT

OPTIMIZATION OF NiO$_x$ BASED HTL THICKNESS FOR P-I-N TYPE PLANAR CH$_3$NH$_3$PbI$_3$ SOLAR CELLS

Ayşenur ALTAY 19022030

Advisor: Assoc Dr Fatma Pınar CHOI

ABSTRACT This thesis pioneers the investigation of adjusting the thickness for nickel oxide (NiO$_x$) thin films in the perovskite solar cells (PSCs). The research introduces a solution-based, glove-box-free fabrication approach for such solar cells utilizing inorganic nickel oxide hole transport layers. Examining the impact of NiO$_x$ thickness in the PSCs, it was observed that Solution D resulted in higher current densities. In contrast, increasing the thickness of NiO$_x$ exhibited an increase in open-circuit voltage and an improvement in the power conversion efficiency (PCE). These enhancements are suggested to be associated with increased hole concentration and improved lattice integration.

INTRODUCTION

Importance of Perovskite Solar Cells and Charge Transport Layers

Perovskite solar cells, named after the Russian mineralogist Perovski, have gained significance due to their unique crystalline structure, with a general formula ABX$_3$. In 2009 CH$_3$NH$_3$PbI$_3$ perovskites were introduced as light absorbers in solar cells, with modest efficiency ~4%. [1] By 2013, perovskite solar cells achieved PCEs as high as 15% [2] and now boosted to 26.1% [3] earning recognition as one of the top 10 breakthrough technologies.
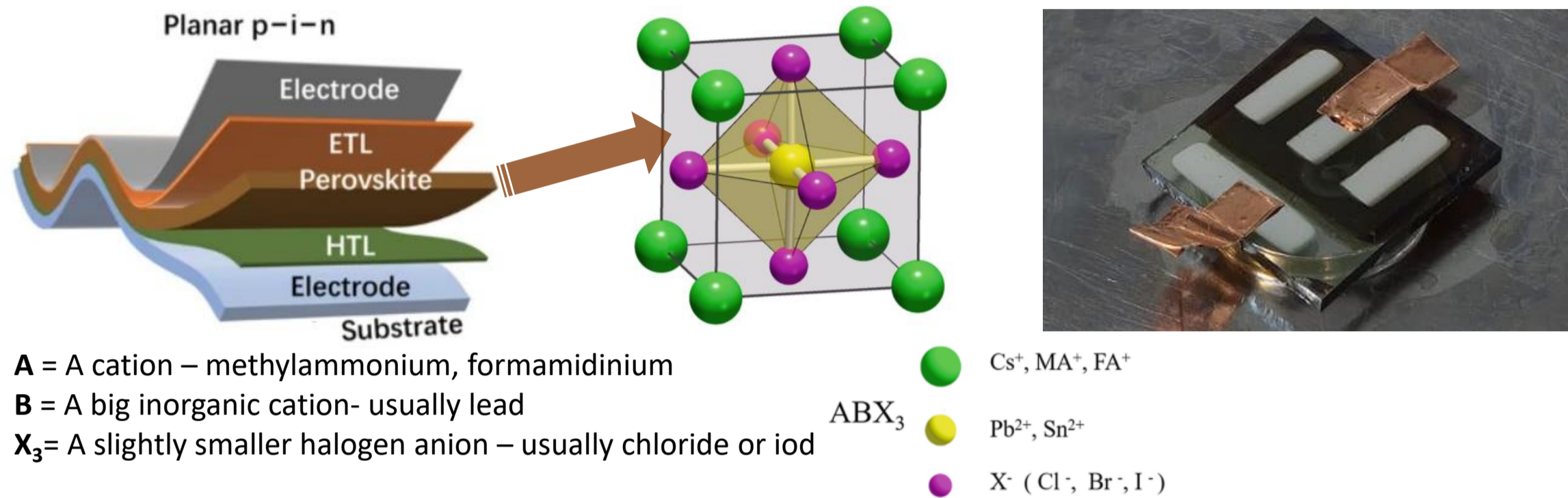
A = A cation – methylammonium, formamidinium
B = A big inorganic cation- usually lead
X$_3$ = A slightly smaller halogen anion – usually chloride or iod

ABX$_3$
Cs$^+$, MA$^+$, FA$^+$
Pb^{2+}, Sn^{2+}
X$^-$ (Cl$^-$, Br$^-$, I$^-$)

Fig. 1 Device structure of a typical PSC and a PSC whose fabrication has been completed [4,5].

Perovskite
- High light absorption, high dielectric constant
- Large carrier mobility, balanced electron-hole mobilities
- Adjustable band gap
- Adaptability to flexible devices & fabrication at low T (<150 °C)
- Low-cost, high-efficiency (PCE) solar cells

Perovskite light absorbers play an important role in solar harvesting, but the success of the solar cell depends on additional layers, such as electron and hole transport layers (HTLs). These layers are essential for the stable and efficient devices. Their effectiveness is related to the crystal structure, chemistry, electronic and optical properties, and compatibility with the perovskite synthesis process. The inclusion of HTLs in perovskite solar cell has played a crucial role in achieving high-performance devices. The key characteristics of an effective HTL are efficient electron blocking and hole extraction, which can have a significant impact on device parameters, such as the open-circuit voltage (V$_{OC}$). So far, various types of materials, including inorganic, polymeric, and small organic molecules, have been investigated and used as HTLS. Significant efforts have been made in the optimization of HTLs for the stability and efficient semiconductor properties. Among these, NiO$_x$ has emerged as the most attractive candidate.

Why NiO$_x$?

Advantages of NiO$_x$
- Low cost
- Chemical &mechanical stability
- High optical transparency
- Wide direct bandgap
- Deep VB :ability to block electron leakage
- Proper work function
- Energy level alignment with CH$_3$NH$_3$PbI$_3$

Disadvantages of NiO$_x$
- Low intrinsic conductivity
- Energy level offset
- Charge recombination
- Require conductivity adjustment

EXPERIMENTAL

Preparation of NiO$_x$ Solution

NiO$_x$ HTLs were fabricated via the sol-gel method. The NiO$_x$ precursor solution was prepared by dissolving 2488.4 mg of nickel salt in 10 ml of ethanol for 15 minutes. Subsequently, 600 μl of diethanolamine (DEA) were added to the mixture. The solution's color transitioned to blue-green upon the addition of DEA at room temperature and then to clear green upon the dissolution of the nickel salt at 70 °C. The solution was stirred at 70 °C for 1 hour.
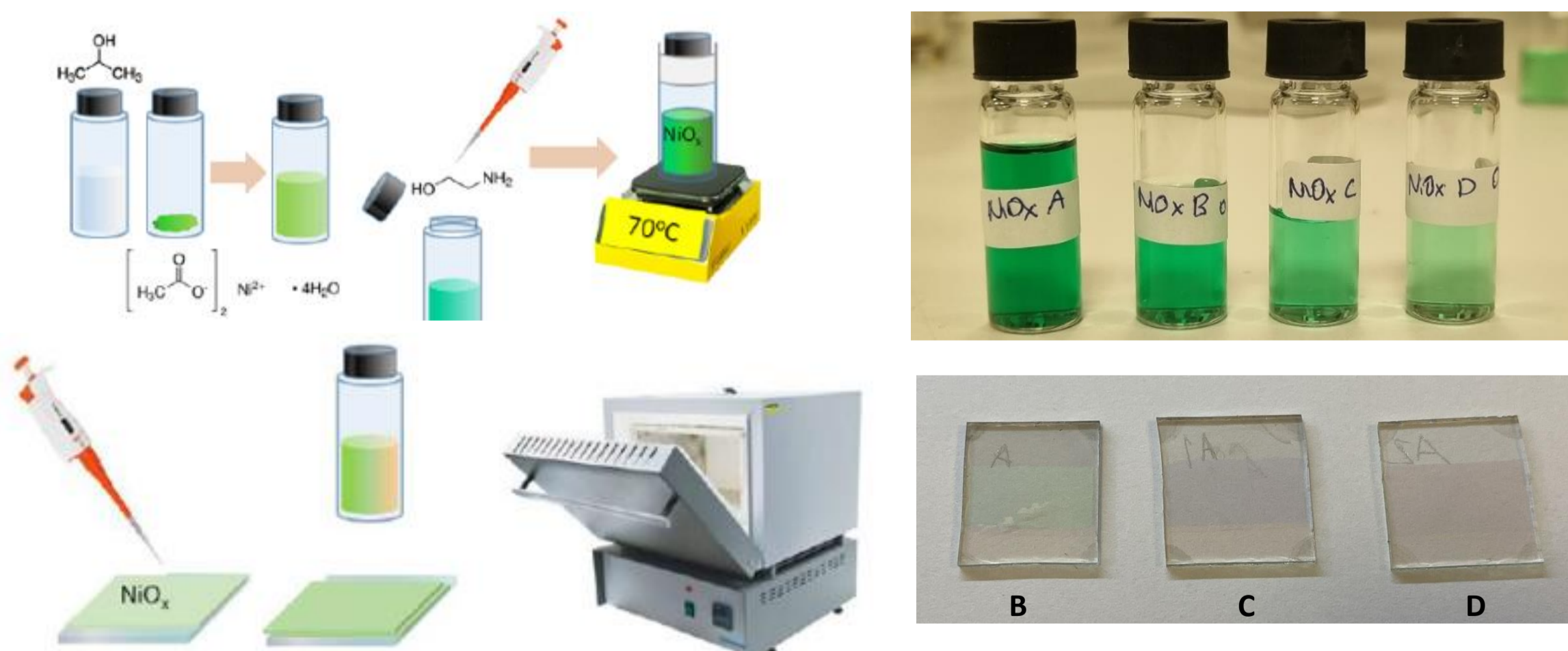
Fig. 2 The production of the NiO$_x$ HTLs

The resulting NiO$_x$ precursor with a 1 M concentration was filtered with 0.45 PVDF syringe filter and denoted as Solution A. Solution A is diluted to obtain lower concentrations. Simply, one volume of Solution A was transferred to another container, and an equal volume of the main solvent (ethanol) was added to obtain a 0.5 molar Solution B. The same procedure was repeated to obtain 0.25 molar Solution C and 0.125 molar Solution D.

Device Fabrication

The filtered solutions are deposited onto cleaned ITO-coated glass substrates using a spin coater at 4000 rpm for 30 s. After the first layer is dried at 70 °C for 90 s, coating is repeated. Finally, samples are annealed in an oven at 450 °C for 30 minutes. For perovskite fabrication; the perovskite solution, held at 90 °C, was deposited onto pre-heated (100°C) NiO$_x$ substrates, at 2000 rpm for 10 s and 4000 rpm for 20 s. After 3 s of the second step, 100 μl of toluene was injected onto the spinning substrate. The substrates were then transferred onto a hot plate kept at 100 °C for a duration of 20 minutes under ambient air conditions. PCBM layers were applied through casting at 1500 rpm for 15 s and subsequently at 2000 rpm for 20 seconds, followed by drying at 90 °C for 90 seconds. Subsequently, a solution of BCP in ethanol was spin-coated at 4000 rpm for 40 seconds. All steps involving sol-gel fabrication were conducted under ambient air conditions, with relative humidity maintained at 50-55% and environmental temperature at 17-19 °C. Finally, all samples were subjected to high vacuum conditions (<5x10^6 Torr), and 110 nm thick Ag back contacts were evaporated through a mask.

RESULTS AND DISCUSSION

UV-visible transmittance spectra are presented in Figure 3 NiO$_x$ HTLs deposited on ITO-coated glass substrates. Notably, all NiO$_x$ layers exhibited excellent optical transmittance exceeding 60% across the visible and near-infrared spectral ranges. The reduction in transmittance of the HTLs with increasing NiO$_x$ thickness holds significance for inverted PSCs, as it correlates with optical losses that may hinder efficient utilization of the solar spectrum and lead to decreased current densities. Solution D exhibits approximately 85% transmittance in the visible spectrum, attributed to its minimal thickness. Therefore, Solution D stands out as the optimal choice among the alternatives for photo-current generation.
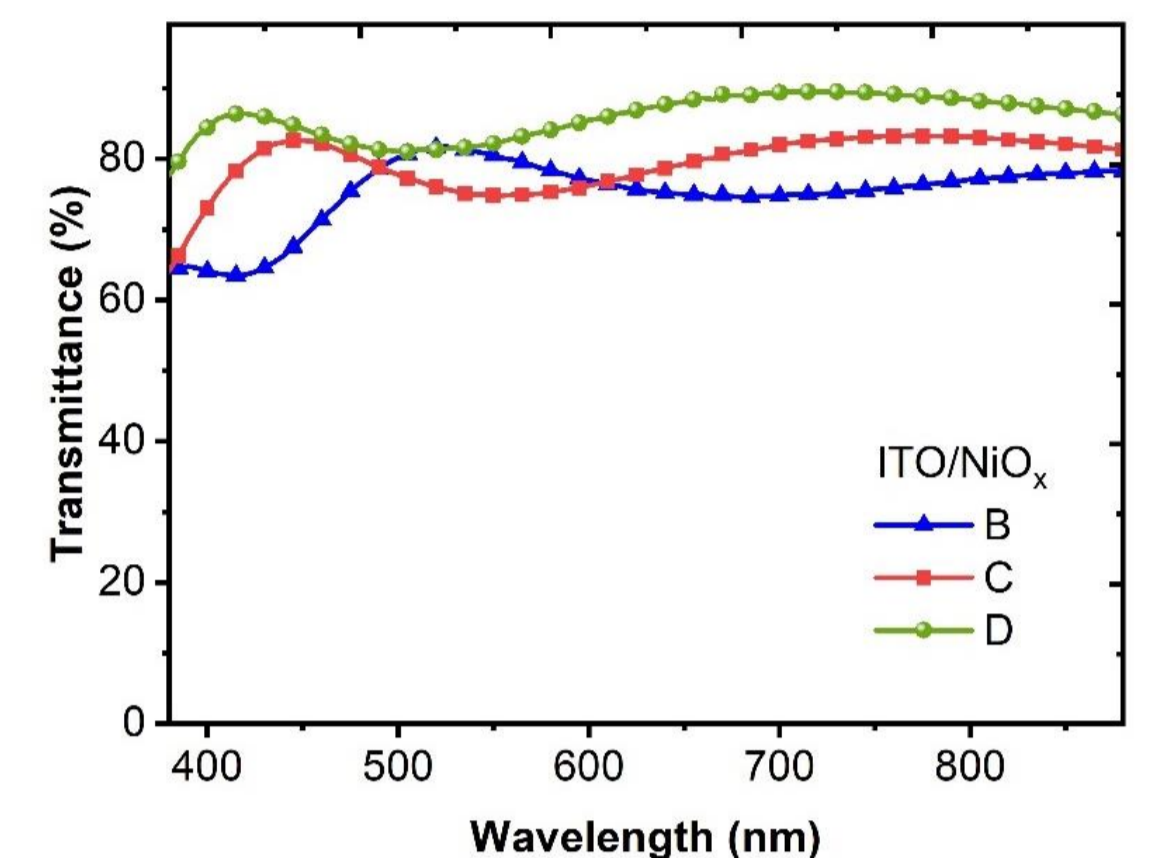
Fig. 3 Optical transmittance curves of NiO$_x$ HTLs

Light J-V curves, recorded under simulated sunlight, are presented in the Fig. 6 for various NiO$_x$ thickness. The current density increases as the NiO$_x$ thickness decreases. The increase from A to B is visibly noticeable, while the difference between C and D is very small.
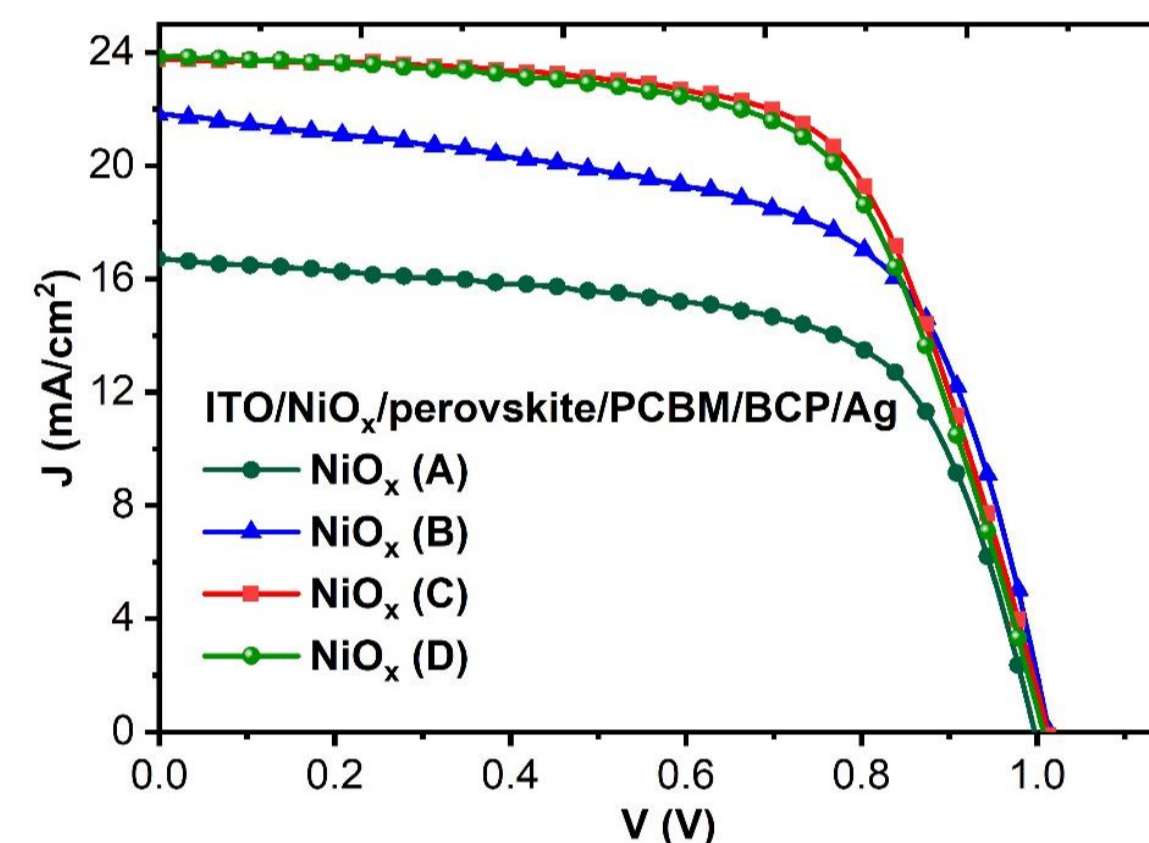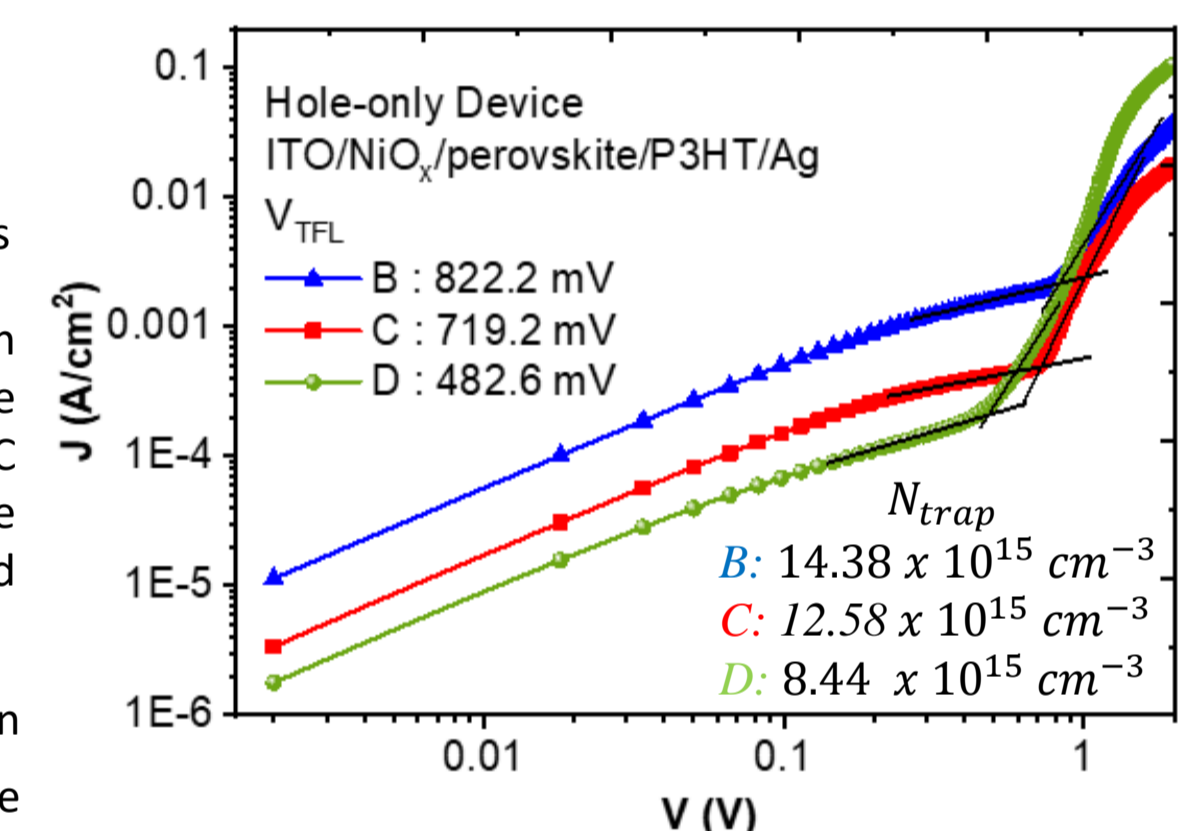
Fig. 4 Illuminated J-V curves of the various HTL employed PSCs

A way to examine defects states and charge dynamics between perovskite and charge transport layers is the space charge limited current (SCLC) method using hole-only devices. SCLC curves usually possess three separate parts that begin with the Ohmic region at low bias, continue with a non-linear trap-filled region, and end with the space-charge limited current region.

Trap-densities can be calculated by $V_{TFL} = \frac{eN_{trap}L^2}{\varepsilon_0\varepsilon_r}$ equation using experimentally extracted the V_{TFL} voltages from the intersection of Ohmic and trap filled regions.

Hole-only Device ITO/NiO$_x$/perovskite/P3HT/Ag
V_{TFL}
B : 822.2 mV
C : 719.2 mV
D : 482.6 mV
N_{trap}
B: 14.38 x 10^{15} cm^{-3}
C: 12.58 x 10^{15} cm^{-3}
D: 8.44 x 10^{15} cm^{-3}

Fig. 5 Dark J-V curves of the hole-only devices.

Fig. 5. shows that solution D exhibited the lowest trap-density and V_{TFL} voltage values for hole-only devices. The observed decrease in N_{trap} and V_{TFL} voltages with decreasing NiO$_x$ thickness suggest an optimal value for defect passivation.

Statistical data was obtained by selecting the samples with the best potential from the measurements made. When the photovoltaic parameters of the solar cells were examined according to the thickness of NiO$_x$, as shown in Fig. 6, it was observed that the decreasing of the NiO$_x$ thickness caused a noticeable change in the photovoltaic parameters.
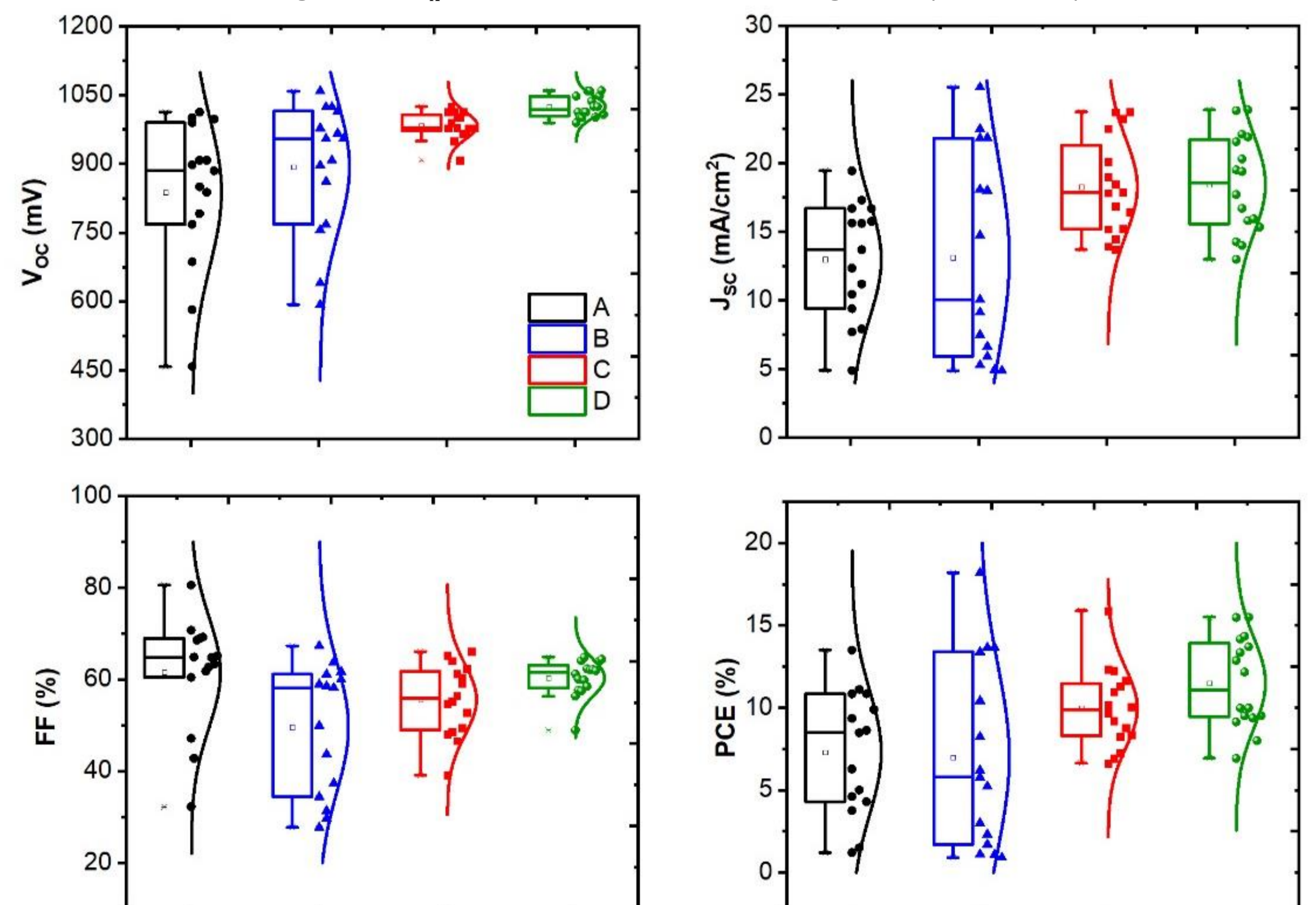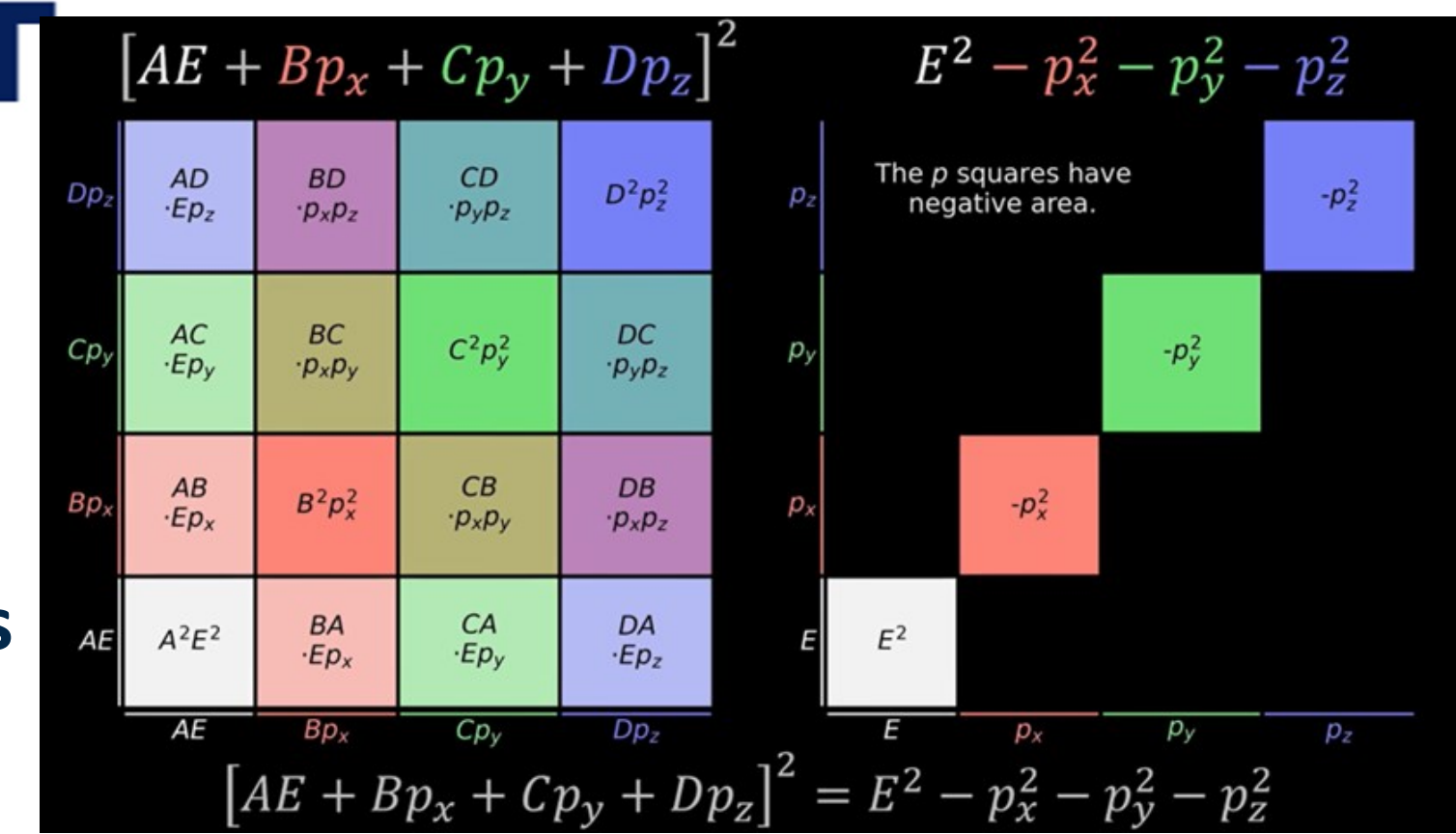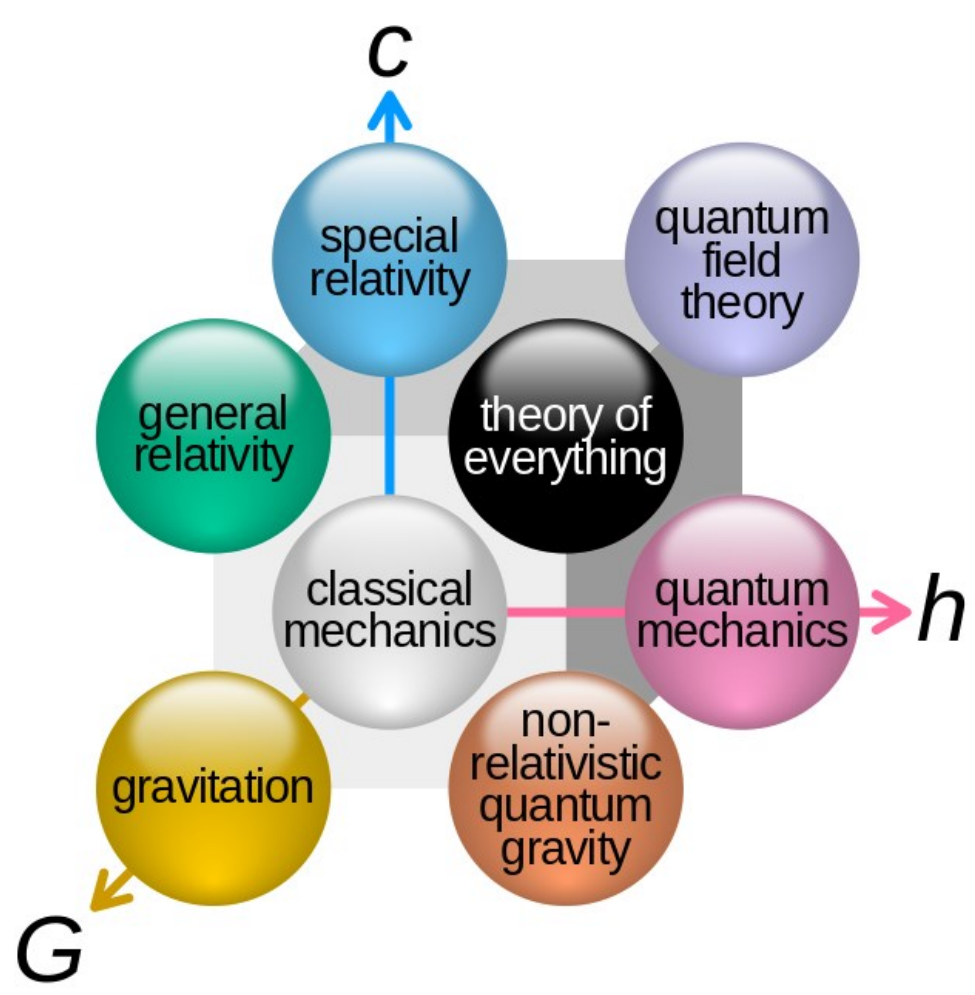
Fig. 6 Statistical photovoltaic parameters for various NiO$_x$ HTL employed PSCs

In summary, we successfully optimized all production conditions for NiO$_x$ HTL thickness-dependent PIN planar PSCs, yielding comparable result. We anticipate that further enhancements in PCEs can be achieved by exploring various perovskite precursors, including other suitable perovskite candidates for NiO$_x$. In conclusion, while the NiO$_x$ HTL layer is a promising HTL candidate for efficient and stable PIN planar PSCs, adjusting the thickness of NiO$_x$ results in a significant improvement in the photovoltaic parameters of the solar cell.

REFERENCES [1] A. Kojima, K. Teshima, Y. Shirai and T. Miyasaka, J. Am. Chem. Soc. 131, 6050 (2009). [2] M. Liu, M. B. Johnston and H. J. Snaith, Nature 501, 395 (2013) [3] Liang, Z., Zhang, Y., Xu, H., Chen, W., Liu, B., Zhang, J., ... & Pan, X. (2023). Homogenizing out-of-plane cation composition in perovskite solar cells. Nature, 624(7992), 557-563 cells. [4] Zhai, X., Huang, Y., Feng, Z., Zhang, X., & Wang, Q. (2020). Cesium Lead Halide Perovskite Quantum Dots in the Limelight: Dynamics and Applications. Quantum Dot Optoelectronic Devices, 175-205. [5] Li, X., Yu, H., Liu, Z., Huang, J., Ma, X., Liu, Y., ... & Wang, M. (2023). Progress and challenges toward effective flexible perovskite solar cells. Nano-Micro Letters, 15(1), 206.

Physics Department

Introduction To Relativistic Quantum Mechanics

Abdulrakeeb Alsarori 17022086

Thesis Supervisor: Lec. PhD. Özgür Akçalı

YTU FEN EDEBİYAT FAKÜLTESİ

$[AE + Bp_x + Cp_y + Dp_z]^2$

$E^2 - p_x^2 - p_y^2 - p_z^2$

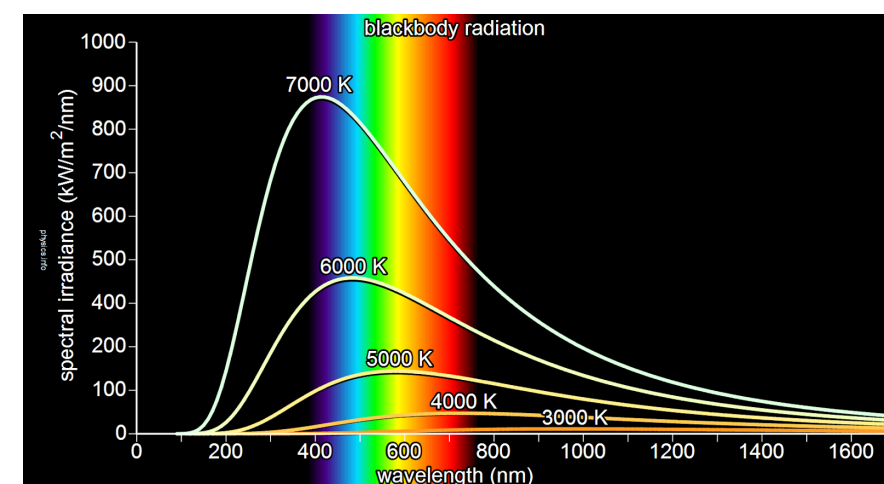$[AE + Bp_x + Cp_y + Dp_z]^2 = E^2 - p_x^2 - p_y^2 - p_z^2$

ABSTRACT

This study has been prepared so as to unite the special theory of relativity and quantum mechanics. At first, a detailed description of Einstein's special relativity is given leading up to the derivation of relativistic energy. Next, quantum mechanics is dealt with by showing proofs of quantization of energy. The two examples mentioned are the black body radiation and the photoelectric effect. Schrodinger's use of position, momentum, and energy operators is introduced. Once these two theories that form the backbone of modern physics have been shown, an attempt to combine them is given by the Klein-Gordon equation where they replace classical energy by relativistic energy resulting in a second order time equation. Because it fails to explain the hydrogen atom, another attempt is made but this time by Dirac who uses matrices and writes the equation in the form of first order derivative of time. Solutions to his equation indicate the existence of antimatter.

Quantum Mechanics

<u>Black body</u> is a body with a surface that has a property of absorbing all of the radiation incident on it and emitting all the radiation it absorbed. Classically, energy was assumed to be continuous, so Rayleigh-Jeans calculated the expectation value using integrals

$$\overline{\mathcal{E}} = \frac{\int \mathcal{E}\, P(\mathcal{E})d\mathcal{E}}{\int P(\mathcal{E})d\mathcal{E}} = \frac{\int \mathcal{E}e^{\frac{-\mathcal{E}}{KT}}d\mathcal{E}}{\int e^{\frac{-\mathcal{E}}{KT}}d\mathcal{E}} = \frac{K^2T^2}{KT} = KT$$

This notion of energy being continuous resulted could only explain low frequencies, but for UV light frequencies and above, it was unsuccesful. It became known as the UV catastrophe. In 1900, Max Planck mathematically came up with a method so as to fit the graph; he realized that there has to be discrete energy levels. So instead of an integral we have:

$$\overline{\mathcal{E}} = \frac{\sum \mathcal{E}\, P(\mathcal{E})}{\sum P(\mathcal{E})} = \frac{h\nu}{e^{h\nu/KT} - 1}$$
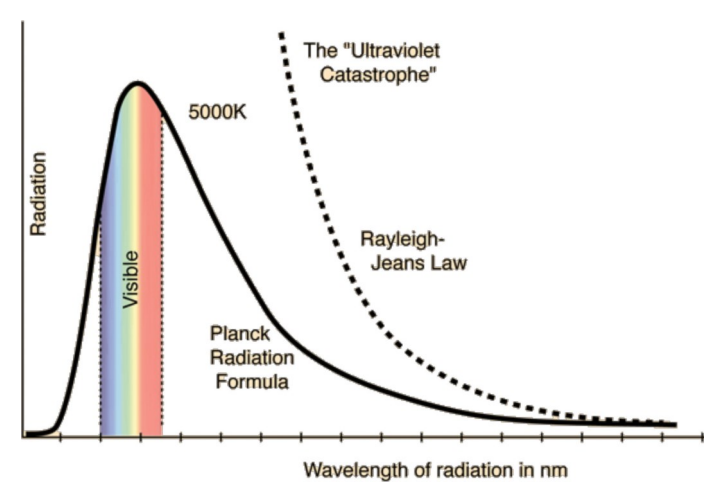
This successfully explained the graph and started the concept of "quantization" of energy. Energy cannot be continuous, rather it has discrete levels called "quanta". In 1905, Einstein explained the photoelectric effect using the idea of quantization of energy. 1926, Schrödinger used (h) planck's constant and replaced x , p and E with their respective operators:

$$p \to -i\hbar\nabla \quad E \to i\hbar\frac{\partial}{\partial t}$$

So the becomes

$$H = \frac{p^2}{2m} + V = E \text{ classical} \qquad i\hbar\frac{\partial}{\partial t}\Psi = \frac{-i\hbar^2}{2m}\nabla\Psi \text{ Hamiltonian}$$

Special Relativity

In 1905, Einstein's two postulates of special relativity started a new set of relativistic equations. The postulate that the speed of light is the same in vacuum for all observers in all inertial (non-accelerating) reference frame led to to the derivation of time dilation and length contraction , so

$$dt = \gamma dt_p \qquad p = m\frac{dr}{dt/\gamma} = \gamma mv$$

$$F = \frac{dp}{dt} \quad \Delta K = W = \int_{K_i}^{K_f}Fdx \quad K = (1-\gamma)mc^2 \quad mc^2 = E_r \quad E = K + mc^2 = \gamma mc^2$$

Then

$$E^2 = (pc)^2 + (mc^2)^2$$

The total energy is Er + K. By squaring E and P and subtracting , we can eliminate v . The result, after some algebra is the desired relativistic energy equation of

$$E^2 = (pc)^2 + (mc^2)^2$$

Relativistic Quantum Mechanics

$$\left(i\hbar\frac{\partial}{\partial t}\right)^2 = (-i\hbar\nabla c)^2 + (mc^2)^2$$

$$-\hbar^2\frac{\partial^2}{\partial t^2} + \hbar^2 c^2\nabla^2 = (mc^2)^2$$

$$-\frac{1}{c^2}\frac{\partial^2\Psi}{\partial t^2} + \nabla^2\Psi = \left(\frac{mc}{\hbar}\right)^2\Psi$$

Now that both quantum mechanics and special have been explained, let's the attempts of uniting them. In 1926, Klein and Gordon took inspiration from Schrodinger's wave. Whereas the latter used the hamiltonian of a classical energy, the former decided to use relativitic energy that is

Basically, they used $(\Box + \mu^2)\psi = 0$ x, p, and E operators and applied them to relativistic energy, so

$$\Box = \partial^\mu\partial_\mu = \eta^{\mu\nu}\partial_\nu\partial_\mu = \frac{1}{c^2}\frac{\partial^2}{\partial t^2} - \nabla^2$$

relativity look at

$$\eta_{ab} := \begin{bmatrix} 1 & 0 & 0 & 0 \\ 0 & -1 & 0 & 0 \\ 0 & 0 & -1 & 0 \\ 0 & 0 & 0 & -1 \end{bmatrix} = diag(1,-1,-1,-1)$$

$$(x^a) = (x^0, x^1, x^2, x^3) = (x^t, x^x, x^y, x^z)$$

$$\mu = \frac{mc}{\hbar} \qquad \left(\frac{E}{c}\right)^2 - p^2 = (mc)^2$$

$$p = (p^0, p^1, p^2, p^3) = \left(\frac{E}{c}, p_x, p_y, p_z\right)$$

The Dirac Equation

Schrodinger's equation's little success led physicists like Klein and Gordon to use relativistic energy as opposed to classical energy. The Shcrodinger equation could only explain the light hydrogen atom and approximate the helium one. The Klein-Godron was supposed to be a better explanation since it incorporates relativistic energy; however, it couldn't even explain the hydrogen atom. It had a negative probability density and was of the second order time equation. That's when the genious Dirac set to solve the issue by using relativistic energy and writing the equation as a first order time and space equation. Therefore,

$$\sqrt{p_0{}^2 - p_1{}^2 - p_2{}^2 - p_3{}^2} = Ap_0 + Bp_1 + Cp_2 + Dp_3$$

$$p_0{}^2 - p_1{}^2 - p_2{}^2 - p_3{}^2 = (Ap_0 + Bp_1 + Cp_2 + Dp_3)^2$$

For this to be true, $(\gamma^0)^2 = A^2 = 1,$ $(\gamma^1)^2 = B^2 = -1,$
$(\gamma^2)^2 = C^2 = -1,$ $(\gamma^3)^2 = D^2 = -1$

AB+BA=0, AC+CA=0, AD+DA=0,
BC+CB=0, BD+DB=0, CD+DC=0

Mathematically, $\{\gamma^\mu, \gamma^\nu\} = 2g^{\mu\nu}$ $\gamma^0 = \begin{pmatrix} 1 & 0 \\ 0 & -1 \end{pmatrix}$ $\gamma^i = \begin{pmatrix} 0 & \sigma^i \\ \sigma^i & 0 \end{pmatrix}$

Then $p^\mu p_\mu - (mc)^2 = (\gamma^k p_k + mc)(\gamma^\nu p_\nu - mc)$ $(\gamma^\nu p_\nu - mc) = 0$

$$(i\hbar\gamma^\mu\partial_\mu\psi - mc\,\psi) = 0 \qquad \text{(Dirac-Equation)}$$

For px=py=pz=0 $\frac{\partial\psi}{\partial x} = \frac{\partial\psi}{\partial y} = \frac{\partial\psi}{\partial z} = 0$ $(i\hbar\gamma^0\partial_0\psi - mc\,\psi) = 0$ $\frac{i\hbar}{c}\gamma^0\frac{\partial\psi}{\partial t} = mc\psi$

$$\psi = \begin{pmatrix} \psi_1 \\ \psi_2 \\ \psi_3 \\ \psi_4 \end{pmatrix} = \begin{pmatrix} \psi_a \\ \psi_b \end{pmatrix}$$

$$\psi_1 = e^{-i\left(\frac{mc^2}{\hbar}\right)t}\begin{pmatrix}1\\0\\0\\0\end{pmatrix} \qquad \psi_2 = e^{-i\left(\frac{mc^2}{\hbar}\right)t}\begin{pmatrix}0\\1\\0\\0\end{pmatrix}$$

$$\begin{pmatrix} 1 & 0 \\ 0 & -1 \end{pmatrix}\begin{pmatrix} \frac{\partial\psi_a}{\partial t} \\ \frac{\partial\psi_b}{\partial t} \end{pmatrix} = -i\frac{mc^2}{\hbar}\begin{pmatrix} \psi_a \\ \psi_b \end{pmatrix}$$

$$\psi_3 = e^{+i\left(\frac{mc^2}{\hbar}\right)t}\begin{pmatrix}0\\0\\1\\0\end{pmatrix} \qquad \psi_4 = e^{+i\left(\frac{mc^2}{\hbar}\right)t}\begin{pmatrix}0\\0\\0\\1\end{pmatrix}$$

$$e^{-i\left(\frac{E}{\hbar}\right)t}$$

Conclusion

A few years later, quantum field theory was developed. It showed that the Klein-Gordon equation is not a complete mistake, but rather it works for spinless partricles(bosons with s=0). It also showed the Dirac equation worked for fermions whose spin is ½. It even went to explain particles with s=1, this equation is called "Proca Equation". Dirac's work is just as revolutionary as Newton's gravity, Einstein's relativity, and Maxwell's equations in electromagnetism. Dirac's equation anticipated the existence of anti-particles.

References

[1] David J. Griffiths "Introduction to Elementary Particles, 2nd Edition", 2008.

[2] Ray D'inverno and James Vickers "Introducing Einstein's Relativity, Second Edition", 2022.

[3] Anton Z. Capri "Relativistic Quantum Mechanics and Introduction to Quantum Field Theory", 2002.

[4] Richard L. Liboff "Introductory Quantum Mechanics", 1980.

FİZİK BÖLÜMÜ

İÇ ÇARPIM UZAYLARININ VE ORTOGONAL DÖNÜŞÜMLERİN CLIFFORD CEBİRLERİ İLE

GENELLEŞTİRİLMESİ

Mehmet Sinan TANRIVERDİ 18022060

Danışman: Prof. Dr. Reyhan KAYA

ÖZET

İç çarpım uzayları ve ortogonal dönüşümler özel rölativite teorisinin matematiksel temelini oluşturur. Tezde özel rölativite teorisi için gerekli tensörlerin, standart vektör cebiri ve Dirac - Pauli cebirinin Clifford cebirleri ile genellenmesi incelenmiş ve Clifford cebiri muadilleriyle kıyaslanmıştır.

İÇ ÇARPIM UZAYLARI VE ORTOGONAL DÖNÜŞÜMLERİN

CLIFFORD CEBİRLERİ İLE GENELLEŞTİRİLMESİ

Bir Clifford Cebirinin Tanımlanması

Bir Clifford cebiri geometrik yorum göz önüne alındığında, baz vektörlerinin karelerinin alacağı değer ile tanımlanır. Ortonormal bazlı Cl(p, q, z) karesi pozitif bire eşit p tane, negatif bire eşit q tane ve sıfıra eşit z tane baz vektörüne sahiptir. Ortogonal vektörler antikomütatiftir.

Vektörlerin Geometrik Çarpımı

İki vektörün geometrik çarpımı, iç çarpımları ile Grassmann çarpımlarının lineer kombinasyonu olarak tanımlanır. Grassmann çarpımı bir çeşit dış çarpımdır.

$$uv = u \cdot v + u \wedge v$$

Grassmann çarpımı sonucunda ortaya çıkan matemasiksel objeler multivektör olarak adlandırılır. Vektörler eksenlerin yönünü tarif ederken multivektörler düzlemler ve hacimler gibi daha yüksek boyutlu büyüklüklerin oryantasyonunu tarif eder. Çarpımın ilk terimi simetrik ikinci terimi ise antisimetriktir.

Öklid Uzayı - Cl(3, 0, 0)

Öklid uzayını tanımlayan Clifford cebiri Cl(3, 0, 0) geometrik olarak üç boyutlu bir sistemi tarif etse de cebirsel olarak sekiz boyutlu bir sistemdir. Üç eksene ilişkili üç baz vektörü, yani kademe 1 baz elemanı, üç düzlemle ilişkili üç baz bivektörü yani kademe 2 baz elemanı, bir skaler birim yani kademe 0 baz elemanı ve bir trivektör toplamda sekiz tane baz elemanı ile tanımlanır. Bir Clifford cebirinde bulunan en yüksek kademeli baz elemanı söz konusu cebirin psödoskaler birimidir.

$$(\sigma_i)^2 = 1, \ (\sigma_i\sigma_j)^2 = -1, \ (\sigma_p)^2 = (\sigma_1\sigma_2\sigma_3)^2, \ \frac{1}{2}\{\sigma_i, \sigma_j\} = g_{ij} = diag(1,1,1)$$

Minkowski Uzayı - Cl(1, 3, 0)

Minkowski uzayını tanımlayan Clifford cebiri Cl(1, 3, 0) biri zamansal diğer üçü uzaysal dört boyutlu bir uzayı tarif eder. Cebir içinde dört eksenle ilişkili dört baz vektörü, üçü zamansal, üçü uzaysal olmak üzere altı tane baz bivektörü, biri zamansal diğer üçü uzaysal dört tane baz trivektör, bir skaler birim ve psödoskaler kuadrivektör toplamda on altı baz elemanı bulunur.

$$(\gamma_0)^2 = 1, \ (\gamma_i)^2 = -1, \ (\gamma_0\gamma_i)^2 = 1, \ (\gamma_{ij})^2 = -1, \ (\gamma_0\gamma_i\gamma_j)^2 = 1, \ (\gamma_i\gamma_j\gamma_k)^2 = -1$$

$$(\gamma_p)^2 = (\gamma_0\gamma_1\gamma_2\gamma_3)^2 = 1, \ \frac{1}{2}\{\gamma_\mu, \gamma_\nu\} = g_{\mu\nu} = diag(1,-1,-1,-1)$$

Öklid Uzayında Ortogonal Dönüşümler

Yansıma

Öklid uzayında keyfi bir vektörü herhangi bir eksene göre yansıtmak için yansıtma eksenini tanımlayan keyfi bir vektör kullanılarak iki taraflı bir dönüşüm yapılır.

$$v' = -nvn^{-1}$$

Rotasyon

Düzlemleri tanımlayan bivektörlerin karesi negatif bir değer aldığından exponansiyel fonksiyonda kompleks birim yerine kullanılabilir. Bu özellik exponansiyel fonksiyonun Taylor açılımı kullanılarak gösterilebilir.

$$e^{\sigma_i\sigma_j\phi} = \sum_n^\infty \frac{(\sigma_i\sigma_j\phi)^n}{n!} = 1 + \sigma_i\sigma_j\phi - \frac{\phi^2}{2!} - \sigma_i\sigma_j\frac{\phi^3}{3!}\ldots = R_{ij}$$

Vektörlerin rotasyonu çift taraflı bir dönüşümle gerçekleştirilir

$$v' = R_{ij}vR_{ij}^\dagger, \ R_{ij}^\dagger = e^{-\sigma_i\sigma_j\phi}$$

Lorentz Dönüşümleri

Minkowski uzayında gerçekleştirilen ortogonal dönüşümlere Lorentz dönüşümü denir. Uzaysal düzlemlerde rotasyon kuralı Öklid uzayındaki rotasyon kuralı uzay ile uzay-zaman mütekabiliyetinden dolayı aynıdır, zamansal düzlemlerde rotasyon Öklid uzayında farklı hızlarda harekete karşılık geldiğinden uzaysal düzlemlerde rotasyondan farklı bir anlam taşır. Zamansal düzlemlerde rotasyon uzaysal düzlemlerde roasyondan farklı olarak hiperbolik trigonometrik fonksiyonlarla ifade edilir fakat zamansal bivektörlerin karesi pozitif bir değer üreteceğinden yine exponansiyel fonksiyonlar kullanılarak ifade edilebilir.

$$e^{\gamma_0\gamma_i\phi} = \sum_n^\infty \frac{(\gamma_0\gamma_i\phi)^n}{n!} = 1 + \gamma_0\gamma_i\phi + \frac{\phi^2}{2!}\ldots = R_{0i}$$

$$R_{\mu\nu}XR_{\mu\nu}^\dagger = R_{\mu\nu}(x^\mu\gamma_\mu + x^\nu\gamma_\nu)R_{\mu\nu}^\dagger + R_{\mu\nu}R_{\mu\nu}^\dagger(x^\sigma\gamma_\sigma + x^\rho\gamma_\rho)$$

Spinörlerin Rotasyonu

Spinörler vektörleri çarpanlarına ayırarak elde edilir. Clifford cebirinde spinörler minimal sol idealler olarak tanımlanır.

$$v^i\sigma_i = \begin{pmatrix} v^3 & v^1 - iv^2 \\ v^1 + iv^2 & -v^3 \end{pmatrix} = \begin{pmatrix} \psi_1 & 0 \\ \psi_2 & 0 \end{pmatrix} \begin{pmatrix} \psi_2 & 0 \\ \psi_1 & 0 \end{pmatrix}^\dagger$$

Bir vektöre rotasyon dönüşümü uygulandığında spinörlerin her biri tek bir rotor tarafından döndürüleceği için vektörün döndüğü açının yarısı kadar dönerler. Yani spinörlerin dönüşümü vektörlerin aksine tek taraflı olarak yapılır

$$RvR^\dagger = \begin{pmatrix} e^{i\theta} & 0 \\ 0 & e^{-i\theta} \end{pmatrix} \begin{pmatrix} \psi^1 & 0 \\ \psi^2 & 0 \end{pmatrix} \begin{pmatrix} \psi^2 & 0 \\ \psi^1 & 0 \end{pmatrix}^\dagger \begin{pmatrix} e^{-i\theta} & 0 \\ 0 & e^{i\theta} \end{pmatrix} \rightarrow \psi' = R\psi$$

Dirac Denkleminin Rotasyonel Simetrisi

Dirac denklemi rotasyonel simetriye sahiptir yani rotasyon dönüşümleri uygulandığında formu değişmez. Minkowski uzayında rotasyonel simetriye sahip denklemlere Lorentz kovaryant denir.
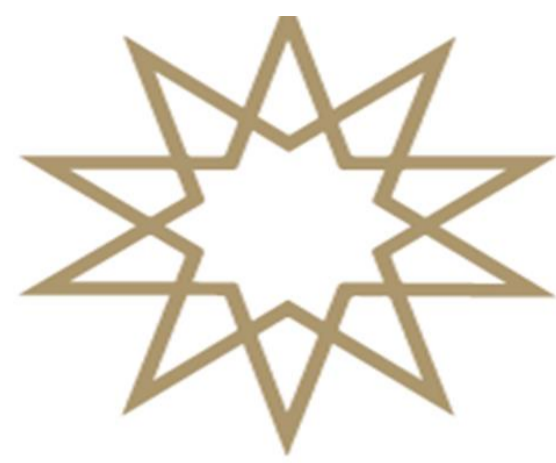
$$(i\hbar\gamma^\mu\partial_\mu - mc)\psi = (i\hbar\gamma^\mu\partial_\mu - mc)R^{-1}\psi' = (i\hbar R\gamma^\mu R^{-1}\partial_\mu - mc)\psi'$$

Sonuç

Clifford cebirlerinin Dirac ve Pauli cebirlerine göre en büyük avantajı tamamen reel sayılarla formüle edilebilmesidir. Bu özellik çok daha sade ve parite dönüşümlerinde daha tahmin edilebilir bir matematiksel dili mümkün kılar. Uzay ve uzay-zaman mütekabiliyeti ise bu iki cebir arasındaki bağlantıyı matrislerin kullanımına gerek kalmadan kurar. Sonuçta Clifford cebirleri Dirac ve Pauli cebirinden daha genel ve matematiğin diğer alanalarıyla daha entegre bir sistem olduğundan bu ikisi yerine kullanılabilir.

KAYNAKÇA

[1] C. McKenzie, "An Interpretation of Relativistic Spin EntanglementUsing Geometric Algebra", Electronic Theses and Dissertations, 5652, (2015).

[2] D. Hestenes, "Spacetime Physics with Geometric Algebra" Am. J.Phys. 71, 691–714 (2003).

[3] A. Lasenby, C. Doran, S. Gull, "Grassmann Calculus, Pseudoclassical Mechanics and Geometric Algebra", J. Math. Phys. 34, 3683, (1993).

YTU FEN EDEBİYAT FAKÜLTESİ

2023-2024 Spring Semester - Department of Physics

Faculty of Art and Science

Calculation of Eigenvalues and Eigenvectors Using 3-D Schrödinger Equation with GPU (CUDA) and LOBPCG Method

Mehmet AKSAN 18022072

Advisor: Prof. Dr. Bora IŞILDAK

ABSTRACT

Advancements in technology and the trending topics of today, such as artificial intelligence and machine learning, have made numerical computations much easier. Extremely complex problems that might take centuries to solve by hand can now be completed in minutes. Humanity can address the most important questions and compute complex formations that can't be solved with pen and paper through code written with specific compilers and software tools. Additionally, these computations not only provide mathematical results but also visual outputs, helping us understand the problem better. In this project, we will calculate the quantum states of a hydrogen atom for specific values using the 3-dimensional Schrödinger equation. During these calculations, we need powerful computers to maximize time efficiency. This is because we will transform the 3-dimensional system we use into a matrix and perform calculations within a 1728000*1728000 matrix, requiring powerful GPUs.The reason for using a GPU is that the matrix to be solved is very large, and manually solving larger matrices might take centuries. However, with powerful GPUs, these operations can be completed in minutes. Below, I will provide information comparing how long the operations take on different GPUs or CPUs.

SCHRODINGER EQUATION

The Schrödinger equation, on the other hand, describes how a wave function, which encapsulates the quantum properties of an isolated physical system, evolves over time. In quantum mechanical description, the system can exist in different states. Each different state has different energy, momentum, etc. When you take the norm of the wave function of a given state, this gives you the probability of the system being in that state. To apply the Schrödinger equation, we need to write the Hamiltonian of the system by considering the kinetic and potential energies of the particles constituting our system. [1]

$$\frac{-\hbar^2}{2m}\left[\frac{\partial^2\Psi}{\partial x^2}+\frac{\partial^2\Psi}{\partial y^2}+\frac{\partial^2\Psi}{\partial z^2}\right]+U(x,y,z)\Psi(x,y,z)=E\Psi(x,y,z)$$

Figure 1: The 3-dimension Time-independent Schrödinger Equation

THE HAMILTONIAN

Every measurable parameter in a physical system is associated with a quantum operator. The operator responsible for the system's energy is called the Hamiltonian operator. In classical mechanics, we express energy as the sum of kinetic and potential energy values. In quantum mechanics, it is an operator corresponding to the total energy of the system, including both kinetic and potential energy.

EIGENVALUES AND EIGENFUNCTIONS

For a physical system, the wave function contains measurable information about that system. To obtain specific values for physical parameters such as energy, quantum mechanical operators associated with that parameter are used on the wave function. For each eigenvalue, there exists an eigenfunction. Solving the Schrödinger equation for a particular energy not only provides us with the eigenvalues but also allows us to find the specific function that defines that energy state.[2]

$$\underset{\text{operator}}{Q_{op}}\psi_i = q_i\underset{\text{eigenvalue}}{\psi_i}\overset{\text{eigenfunction}}{} \qquad H_{op}\psi_i = E_i\psi_i$$

MATERIALS AND METHODS

1. LOBPCG

Locally Optimal Block Preconditioned Conjugate Gradient (LOBPCG) is a matrix-free method for finding the largest (or smallest) eigenvalues and the corresponding eigenvectors of a symmetric generalized eigenvalue problem.

2. PyTorch

PyTorch is a fully featured framework for building deep learning models, which is a type of machine learning that's commonly used in applications like image recognition and language processing. PyTorch is distinctive for its excellent support for GPUs and its use of reverse-mode auto-differentiation, which enables computation graphs to be modified on the fly. This makes it a popular choice for fast experimentation and prototyping

3. CUDA

Compute Unified Device Architecture (CUDA) is a proprietary parallel computing platform and application programming interface (API) that allows software to use certain types of graphics processing units (GPUs) for accelerated general-purpose processing, an approach called general-purpose computing on GPUs.

2-DIMENSION SOLUTION

We use this code to ensure that our code runs through CUDA, the artificial intelligence-enabled part of the GPU [3].

```python
device = torch.device('cuda' if torch.cuda.is_available() else 'cpu')
```

In this example, the potential energy function represents a Gaussian distribution. It is defined using a two-dimensional Gaussian function.

```python
def get_potential(x, y):
    return np.exp(-(x-0.3)**2/(2*0.1**2))*np.exp(-(y-0.3)**2/(2*0.1**2))
V = get_potential(X,Y)
```

Compute the eigenvalues and eigenvectors:

```python
eigenvalues, eigenvectors = lobpcg(H, k=10, largest=False)
```

```python
plt.figure(figsize=(6,6))
plt.pcolormesh(X, Y, get_e(1)**2, cmap='nipy_spectral')
plt.axis('off')
plt.show()
```
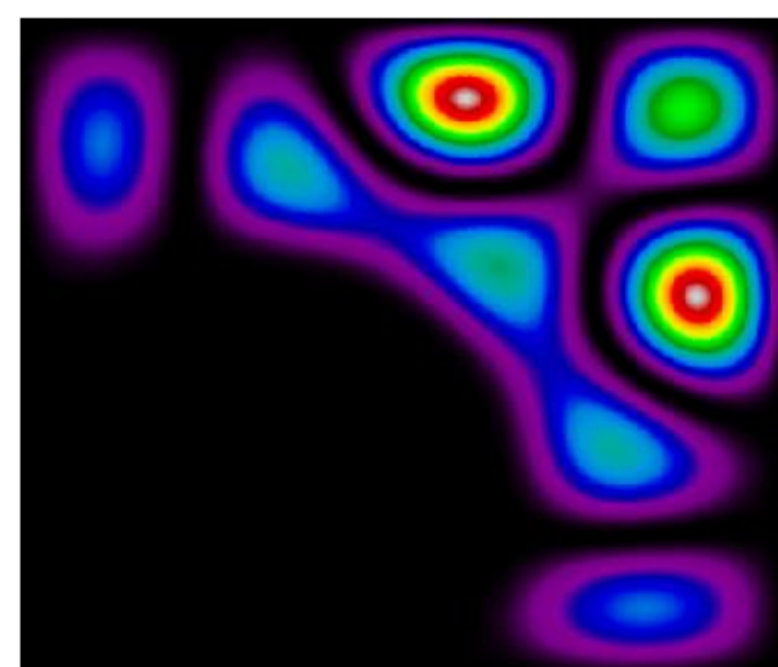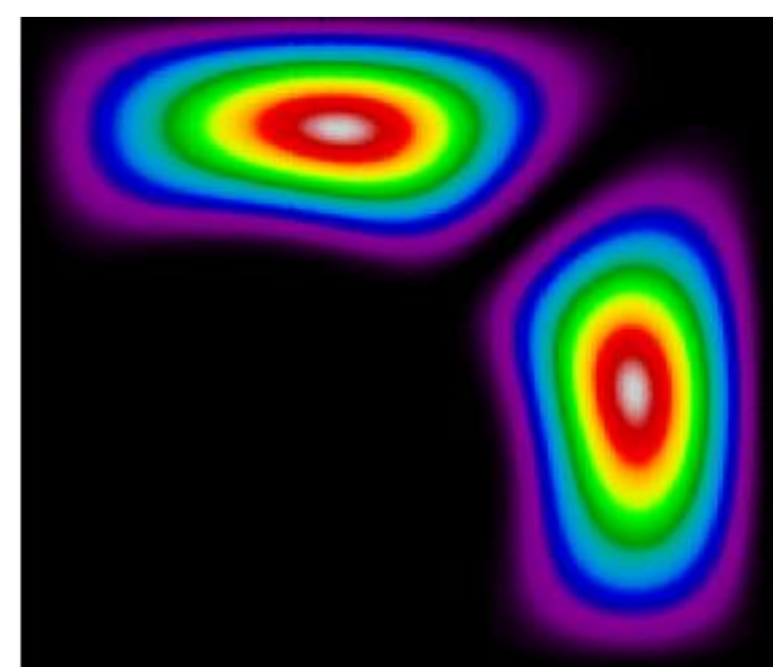

Figure 3 : Visualisation for get_e(1)**2

Figure 3 : Visualisation for get_e(7)**2

3-DIMENSION SOLUTION

The hydrogen atom potential ($\hbar$=1) can be expressed as

and thus

$$V(r) = -\frac{e^2}{4\pi\epsilon_0 r} = -\frac{1}{ma_0 r}$$

$$m\Delta x^2 V = -\frac{\Delta x^2}{a_0 r} = -\frac{(\Delta x/a_0)^2}{(r/a_0)}$$

Since N=120 here, let us assume that a grid with 120 points is formed on each axis and each axis takes values in units of a0 from -25 to 25.

```python
N = 120
X, Y, Z = np.mgrid[-25:25:N*1j, -25:25:N*1j, -25:25:N*1j]
dx = np.diff(X[:,0,0])[0]
```

Function to get hydrogen wave function potential

```python
def get_potential(x, y, z):
    return - dx**2 / np.sqrt(x**2 + y**2 + z**2 + 1e-10)
V = get_potential(X,Y,Z)
```

the process here is the same, but this time we'll perform the calculation for k=20

Function to get eigenvector:
```python
eigenvalues, eigenvectors = lobpcg(H, k=20, largest=False)
```

Compute vertices and faces corresponding to iso-surface of eigenfunction so we can show it off in 3D:

```python
def get_e(n):
    return eigenvectors.T[n].reshape((N,N,N)).cpu().numpy()
```

```python
verts, faces, _, _ = measure.marching_cubes(get_e(19)**2, 1e-6, spacing=(0.1, 0.1, 0.1))
intensity = np.linalg.norm(verts, axis=1)
```
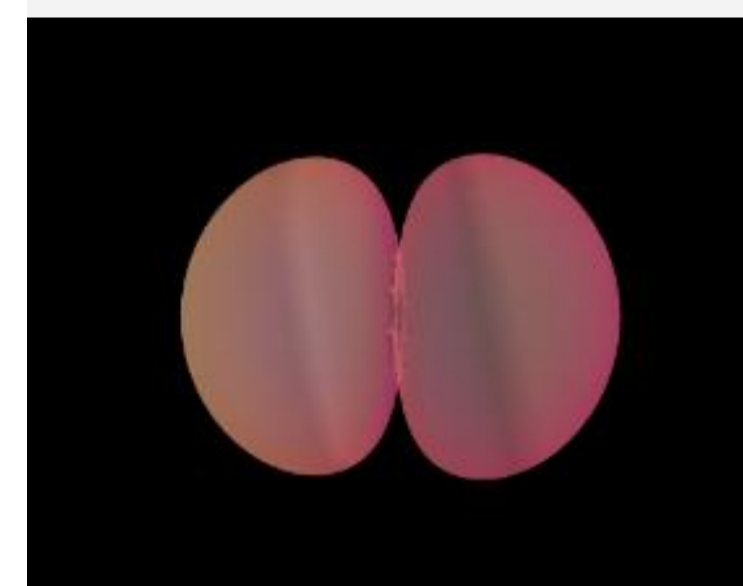

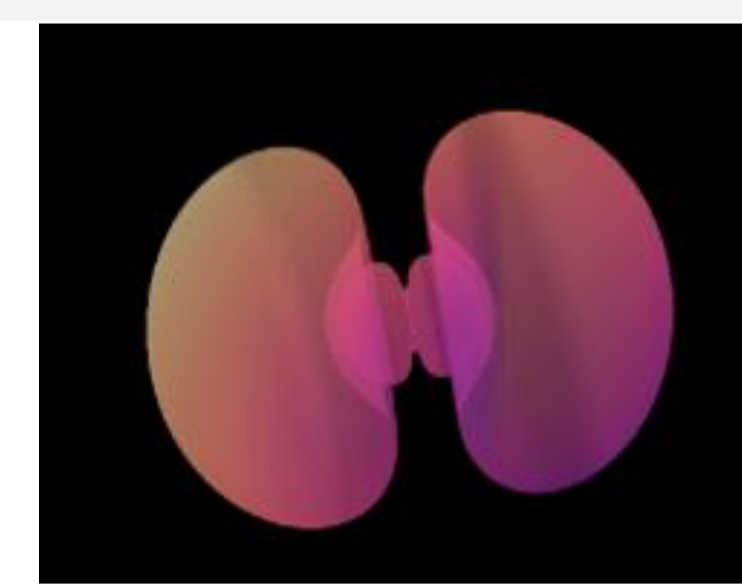Figure 5 : Visualisation for get_e(1)**2
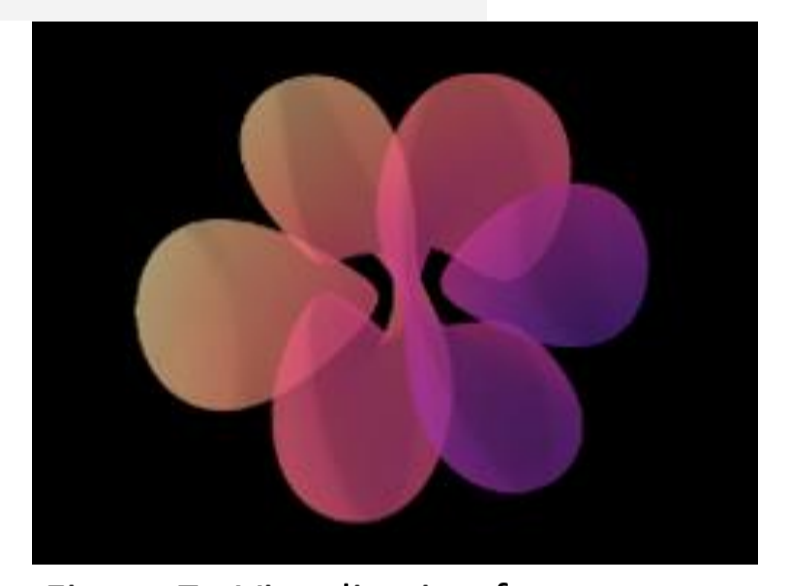

Figure 6 : Visualisation for get_e(7)**2

Figure 7 : Visualisation for get_e(17)**2

$$E = \frac{\hbar^2}{m\Delta x^2 a^2}$$

```python
hbar = 1.055e-34
a = 5.29e-11
m = 9.11e-31
J_to_eV = 6.242e18 # convert from Joules to eV
conversion = hbar**2 / m / dx**2 / a**2 * J_to_eV
```
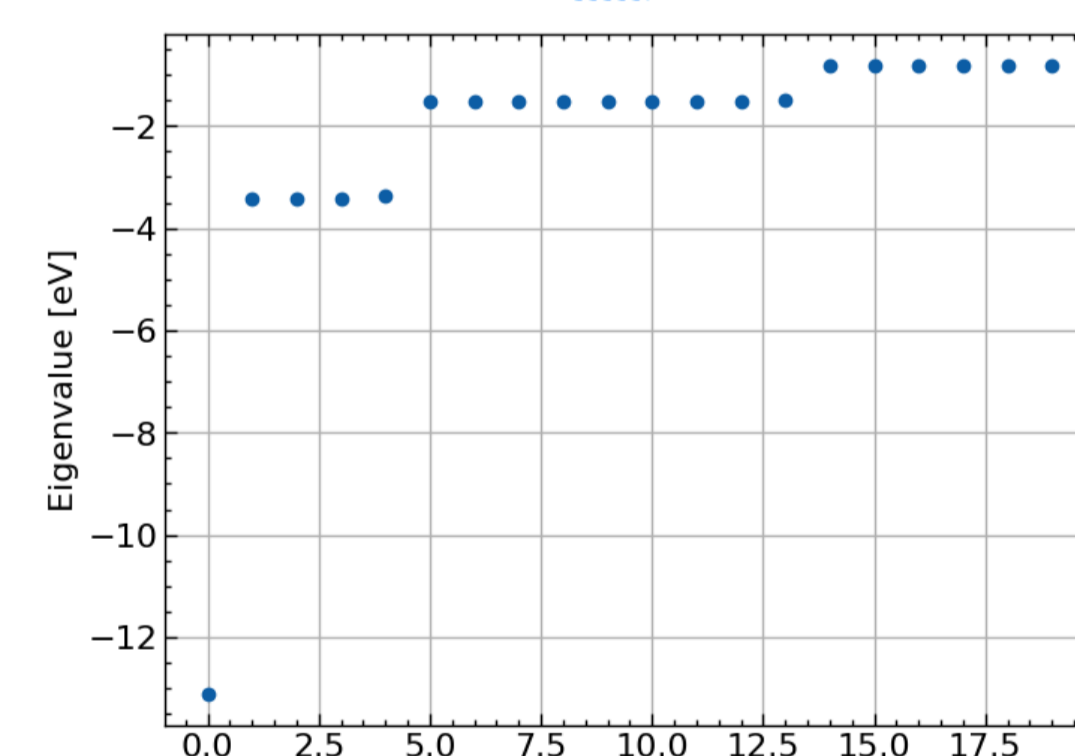

Figure 8 : eigenvalues value to the home value and obtain its energy

CONCLUSION and DISCUSSIONS

Our aim in this study was to show that for potentials with very large values, the work to be done on the GPU provides a very high level of time saving. With our GPU RTX 5000, the solution time of the 3D system had an average solution time of 5 minutes 55 seconds, while with our CPU Intel Xeon Gold 6240, this process took 20 minutes 42 seconds. This means that in such numerical studies, the artificial intelligence-supported CUDA section provided by the graphics card will take centuries in the process of these processes manually, while thanks to the GPU, we reach the result we want at the end of a 5 minute 55 second process. As another comparison, the latest model GPUs can perform these operations in even shorter times with today's developing technology and the importance given to artificial intelligence. For example, before using RTX 5000, it took me an average of 50 minutes to calculate the 3D solution on my own graphics card, GTX 1650 Ti. With RTX 5000, which gives superior performance than GTX 1650 Ti, this process takes 5 minutes. In other words, a 1000% performance increase is detected. And naturally, the better GPU offers a faster solution.

KAYNAKÇA

[1] (Whittaker, Edmund T. (1989). A history of the theories of aether & electricity. 2: The modern theories, 1900 – 1926 (Repr ed.). New York: Dover Publ. ISBN 978-0-486-26126-3.)

[2] Gilbert Strang. "6: Eigenvalues and Eigenvectors". Introduction to Linear Algebra (PDF) (5 ed.). Wellesley-Cambridge Press.

[3] https://github.com/lukepolson/youtube_channel/blob/main/Python%20GPU/schrodinger.ipynb

YTU FACULTY OF ARTS AND SCIENCES

2023-2024 SEMESTER / PHYSICS DEPARTMENT

Investigation of Optical and Photodegradation Properties of Cobalt doped TiO_2 Thin Films

Berke TUNCAY 19022056

Supervisor : Prof.Dr. Zeynep GÜVEN ÖZDEMİR

ABSTRACT

This study investigates the optical properties of Co-doped TiO_2 (titanium dioxide) thin films. Co doping is investigated for its potential to enhance the optical and photocatalytic performance of TiO_2. The films were prepared with specific Co doping levels and coated with ruthenium dye to assess their photodegradation properties. The findings suggest that Co-doped TiO_2 thin films could significantly advance technologies in solar cells, photocatalytic applications, and biomedical implants.

INTRODUCTION

The optical and photocatalytic properties of titanium dioxide (TiO_2) thin films have been extensively studied in the literature, demonstrating their eco-friendly nature and high performance characteristics. This study focuses on Co-doped TiO_2 thin films and explores their potential to enhance optical (3) and photocatalytic capabilities. Through precise Co doping and ruthenium dye coating, photodegradation properties were investigated along with key optical parameters. Successful results hold promise for advancements in solar cells, photocatalysis (1,2) and environmentally friendly technologies, with potential applications in biomedical implants (4,5). This research highlights the significant potential of co-doped TiO_2 thin films and provides new insights for future technological innovations in various fields.

PREPARATION of Co-DOPED TiO_2 THIN FILM SAMPLES

The initial step involves preparing the glass substrates for film coating. The substrates have been washed with distilled water and then placed in an ultrasonic cleaner for 15 minutes (see Figure 1a). Then , they were washed with isopropyl alcohol, returned to the ultrasonic cleaner for another 15 minutes, and then left to dry.
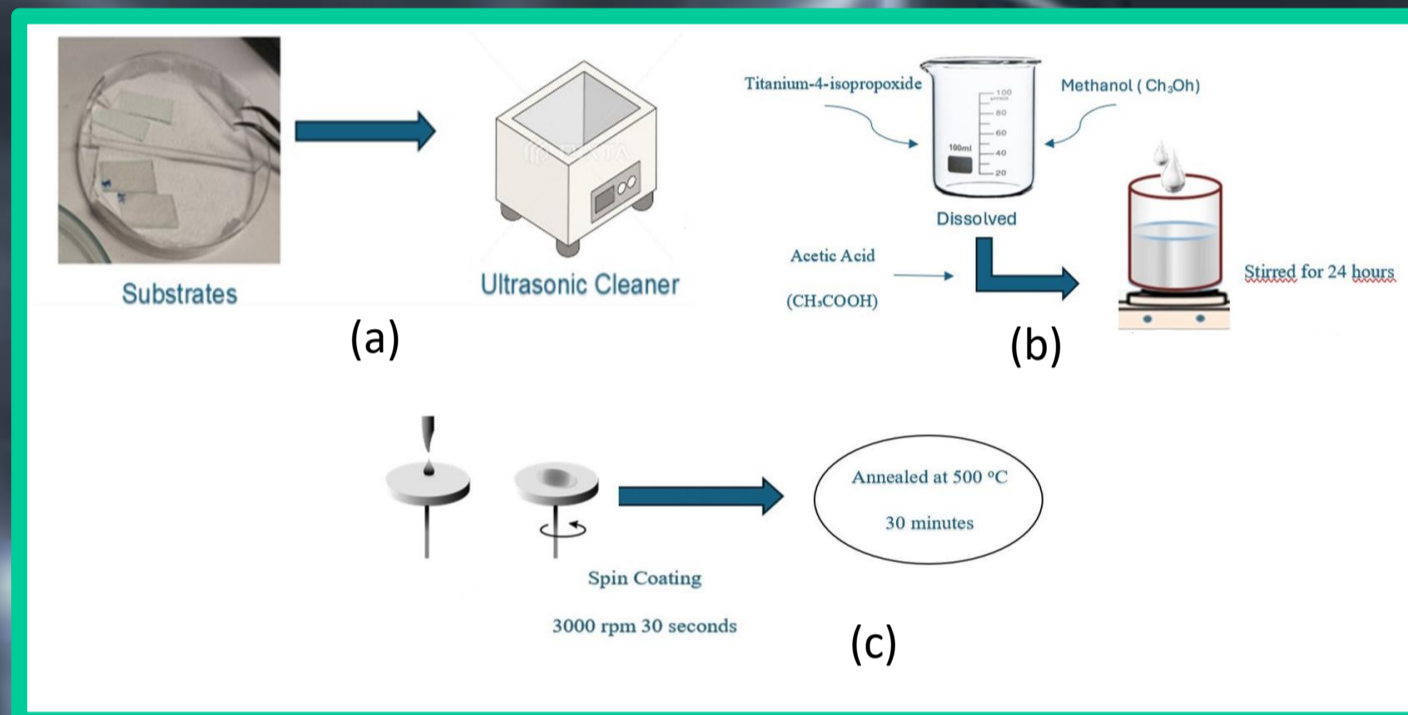

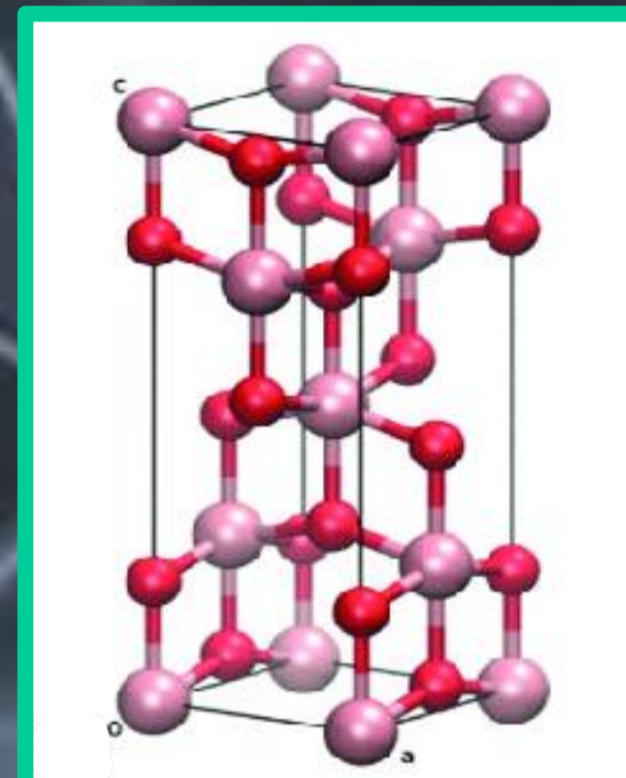Figure 1 Preparation of thin films

Figure 2 Crystal Structure of Anatase TiO_2

In the second step, 3.5 mL of Titanium-4-isopropoxide (TTIP) has been dissolved in 31.5 mL of methanol. Then, 350 µL of 1% acetic acid has been added to 35 mL of the solution and stirred on a magnetic stirrer for 24 hours to obtain a homogeneous mixture (see Figure 1b).
In the final step, a 0.2 M solution has been prepared by dissolving 0.137 g of $CoCl_2$-$6H_2O$ in 3 mL of methanol. These were coated on pure, 1%, 2%, 3%, 4%, and 5% substrates using the spin coating process at 3000 rpm for 30 seconds. The substrates have been then annealed at 500 ºC for 30 minutes (see Figure 1c).Anatase phase crystal structure of TiO_2 has been demonstrated at Figure 2.

The surface morphology of the pure TiO_2 film was viewed by using Scanning Electron Microscope (SEM) The SEM image of the pure TiO_2 thin film was obtained by Jeol JEM SEM. The SEM micrograph of the pure TiO_2 thin film was shown in Figure 3.

As shown in Figure 3, the pure TiO_2 thin film has a relatively tightly packed granular structure in the form of pebbles, uniformly distributed on the film surface.
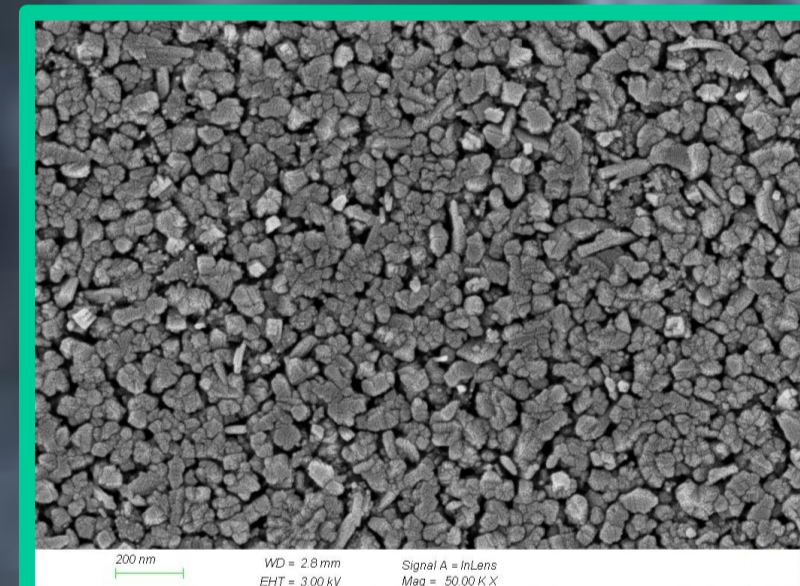

Figure 3 The SEM image of the pure TiO_2 thin film

METHOD

UV-Vis spectroscopy analysis of the samples has been performed at room temperature by measuring of absorbance and transmittance in the wavelength range from 350 to 1100 nm. In order to identify the impact of Co contribution to TiO_2 on the band gap, the direct allowed transition energy bandgap values of the pure TiO_2 and the Co doped TiO_2 have been determined by utilising Tauc's Plot method . A direct calculation of the optical bandgap (Eg) has been performed using (see Eq. 1) .

$$(\alpha h\nu)^2 = A[E - E_g] \qquad (1)$$
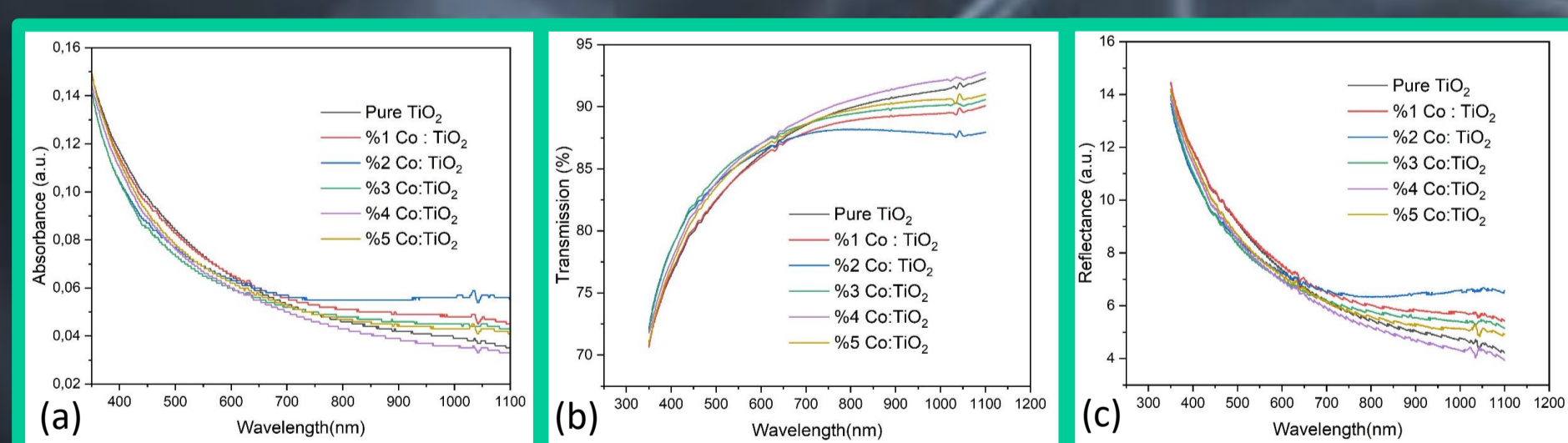
RESULTS and DISCUSSIONS

Figure 4 UV-Vis light absorption (a) , transmission (b) and (c) reflection spectrum

As depicted in Figure 4, the pure TiO_2 film displays characteristic absorption in the UV region, with a significant decrease in optical absorption as the wavelength of light increases towards the near IR region of the electromagnetic spectrum. This same trend is observed in the Co doped TiO_2 thin films. Nonetheless, the absorption values of the Co doped TiO_2 thin films are lower than those of the pure TiO_2 between the wavelengths of 350 nm and 550 nm. The data regarding the band gap, presented in (see Figure 5), has been similarly obtained.

The substitution of cobalt for titanium in the TiO_2 lattice can significantly influence the material's band structure and optical properties. This substitution alters the lattice's stoichiometry and introduces localized electronic changes. As a result, the band gap may be modified, impacting the material's optical behavior.
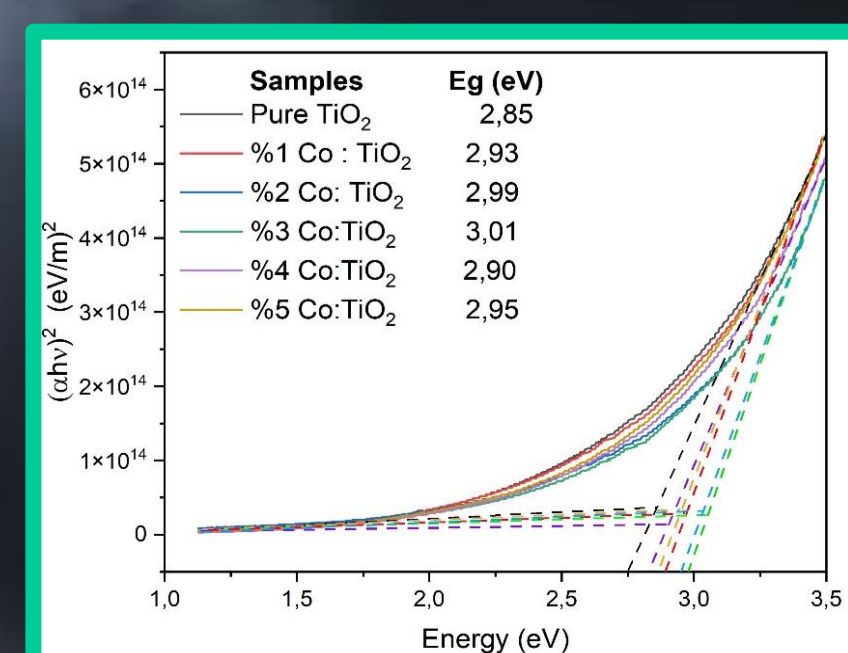

Samples	Eg (eV)
Pure TiO_2	2,85
%1 Co : TiO_2	2,93
%2 Co: TiO_2	2,99
%3 Co: TiO_2	3,01
%4 Co: TiO_2	2,90
%5 Co: TiO_2	2,95

Figure 5 A comparison of the $(\alpha h\nu)^2$ with the energy band gaps of the samples.

One of the objective of this study is to investigate the impact of Co doping on the refractive index (n) (Eq. 3) and extinction coefficient (k) (Eq. 4) of pure and Co doped TiO_2 thin films. But first, the reflectance needs to be calculated (Eq.4).

$$R = 1-A-T \quad (2) \qquad k = \frac{\alpha \lambda}{4\pi} \quad (4) \qquad n = \frac{1+R+\sqrt{R}}{1-R} \quad (3)$$

The refractive index (n) (see Figure 6) of the samples has been determined using reflectance values (R), as described in (Eq. 3) (6).
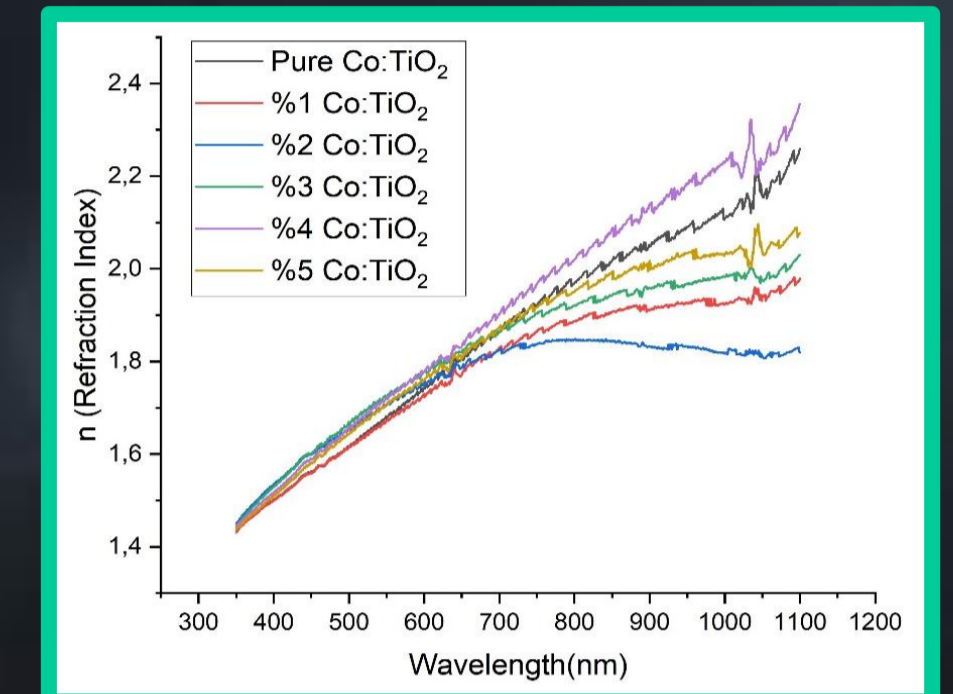
In the initial part of our research, we identified the broadest optical band gap as 3.01 eV in Co:TiO_2 thin films with 3% cobalt doping.

Figure 6 Variation of refractive index with wavelength

For the purpose of studying photodegradation, this sample was exposed to 412 nm wavelength light, corresponding to its band gap energy, for intervals ranging from 20 minutes to 1 hour.

To compare the effects, photodegradation tests were conducted on three different samples: a glass substrate coated with ruthenium dye as a thin film (labeled RD), a glass substrate with a 3% Co:TiO_2 thin film (labeled 3% Co:TiO_2), and a glass substrate coated with ruthenium dye on top of a 3% Co:TiO2 thin film (labeled 3% Co:TiO_2/RD). Following this, the absorbance and transmittance spectra of the samples, which were aged under 412 nm light for periods of 20, 30, 40, and 60 minutes, were recorded across the wavelength range of 350-1100 nm using a UV-Vis spectrometer. The results, including the absorbance spectra of the aged samples compared to the non-aged ones, are depicted in the panels of Figure 7 .
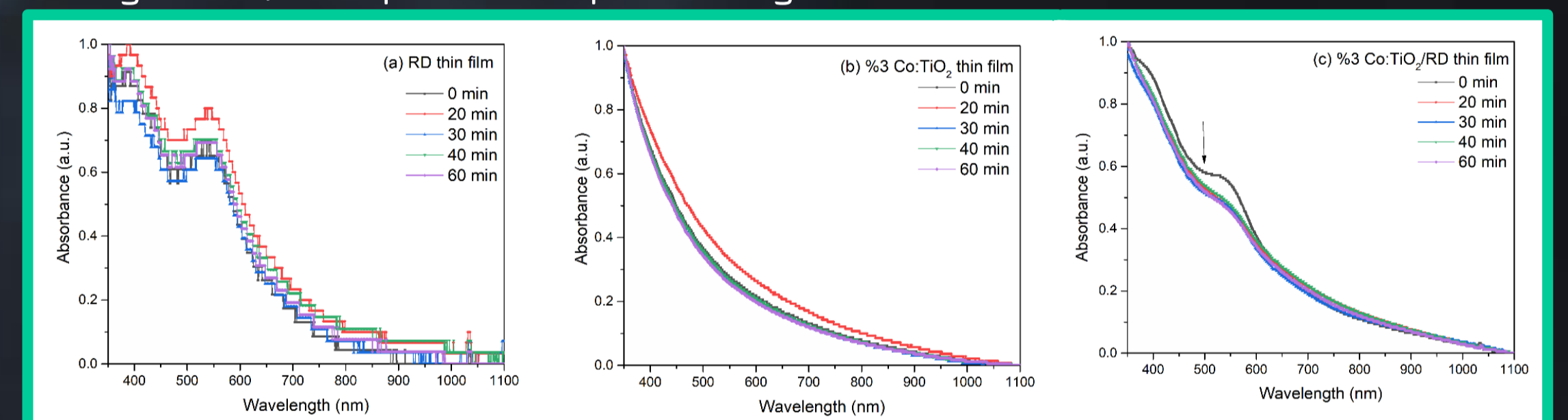

Figure 7 Changes in absorbance spectrum of samples under 412 nm light illumination at different time periods

As illustrated in Figure 7(a), before the illumination with 412 nm light, the ruthenium dye-coated glass exhibits two distinct absorption peaks in the absorbance spectrum. The first peak is centered at 390 nm, while the second is centered at 540 nm. The absorption bands observed at 390 nm and 540 nm can be attributed to a metal-to-ligand charge transfer [40],(41). Conversely, it has been established that the center of the absorbance peaks remained unaltered in the absorbance spectrum obtained following 20 minutes of illumination with 412 nm light. Nevertheless, the absorbance intensity for both peaks exhibited an increase (see Figure 7(a)). This indicates that the electrons in the film are more readily excited following exposure to 412 nm light. Upon examination of the absorbance spectrum of 3% Co:TiO_2 coated thin films on glass (illustrated in Figure 7(b)), it can be observed that there was a slight increase in absorbance across the entire wavelength range after 20 minutes of light exposure. The transmittance spectrum of the three samples aged with 412 nm light for 20, 30, 40, and 60 minute along with non-aged samples are presented in the Figure 8 .
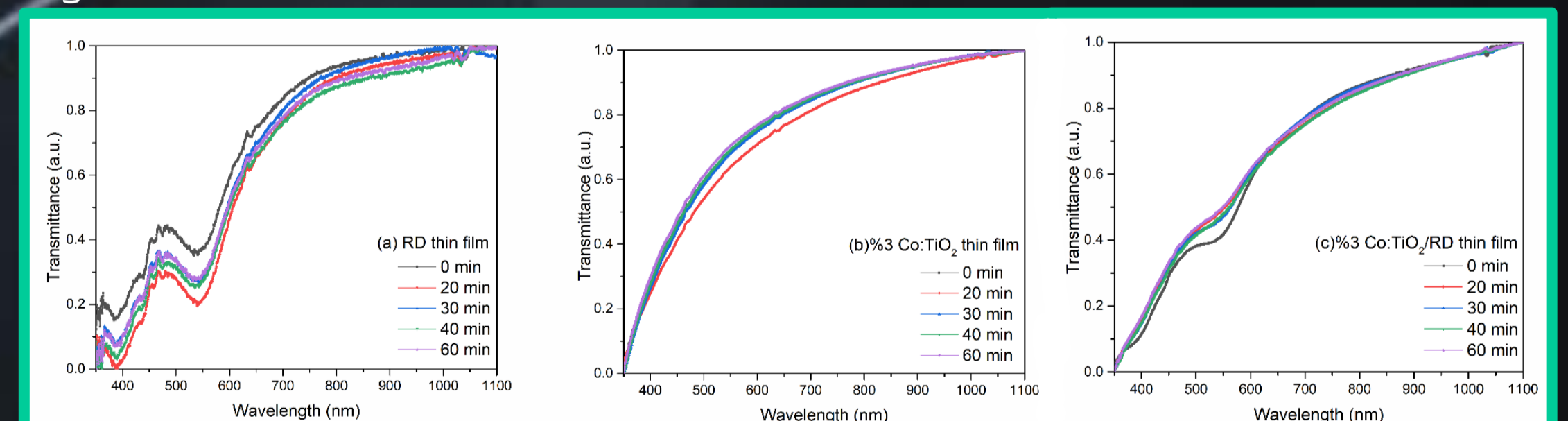

Figure 8 Changes of transmittance spectrum of the samples under 412 nm light illumination at different time periods

CONCLUSION

Cobalt doped TiO_2 thin films have successfully synthesized by sol gel method using TTIP and cobalt chloride (1%, 2%, 3%, 4% and 5%) as precursors. The resulting products have been characterized by UV-vis spectroscopy. As concentration was changed absorption, transmission and reflection were shifted. Same as band gap was also decreased as percentage of doping element cobalt is changed. All thin films showed an increase in transmittance when transitioning from the UV region to the NIR region. From above results it was observed that doping of cobalt plays important role in improvements of photodegredation. The purpose of optimizing study of photodegradation, thin films was exposed to 412 nm wavelength light, corresponding to its band gap energy, for intervals ranging from 20 minutes to 1 hour. It has been established that the center of the absorbance peaks remained unaltered in the absorbance spectrum and slight increased in absorbance obtained following 20 minutes of illumination with 412 nm light.

REFERENCES

[1] A. Velasco-Hernández, R. A. Esparza-Muñoz, F. J. de Moure-Flores, J. Santos-Cruz, and S. A. Mayén-Hernández, "Synthesis and Characterization of Graphene Oxide-TiO2 Thin Films by Sol-Gel for Photocatalytic Applications," Materials Science in Semiconductor Processing, vol. 114, 105082, August 2020 .
[2] Song, H., You, S., Chen, T. et al. Controlled preparation of TiO2 hollow microspheres constructed by crosslinked nanochains with high photocatalytic activity. J Mater Sci: Mater Electron 26, 8442–8450 (2015).
[3] Structural, electronic and optical characteristics of TiO2 and Cu-TiO2 thin films produced by solgel spin coating, Ceramics International, 49(22), Part B, 36265-36275, (2023).
[4] F.H. Jones, Surf. Sci. Rep. 42 (2001) 75.
[5] Ahn TK, Lee DH, Kim TS, Jang GC, Choi S, Oh JB, Ye G, Lee S. Modification of Titanium Implant and Titanium Dioxide for Bone Tissue Engineering. Adv Exp Med Biol. 2018;1077:355-368
[6] Thombare J. V. et al, The effects of electron irradiation on the optical properties of the organic semiconductor polypyrrole, J. Semicond. 34 093001(2013).

YTU FEN EDEBİYAT FAKÜLTESİ

2023-2024 Spring Semester Physics Department

Revealing the Higgs: Enhanced Classification of Particle Decays with Advanced Machine Learning Algorithms

Sezer Mezgil 19022006

Supervisor: Prof. Dr. Bora Işıldak

Summary

This study employs a machine learning dataset from the ATLAS experiment at CERN's Large Hadron Collider (LHC) to distinguish between background and signal events, focusing on the Higgs boson decaying into two tau particles (H → ττ). The dataset, derived from ATLAS open data, consists of simulated proton-proton collision events and is framed as a binary classification problem. Various algorithms were tested, including linear and radial support vector machines (SVM), logistic regression, k-nearest neighbors (KNN), XGBoost, and AdaBoost. XGBoost proved to be the most effective, achieving the highest Area Under the Curve (AUC) score of $0.84 \pm 1.9 \times 10^{-3}$, indicating superior accuracy and stability. AdaBoost and radial SVM followed with AUC scores of $0.82 \pm 2.5 \times 10^{-3}$ and $0.81 \pm 2.7 \times 10^{-3}$, respectively. The models were evaluated using Receiver Operating Characteristic (ROC) curves, cross-validation, and Confusion Matrices (CM). The XGBoost classifier showed the highest true positive rate and the lowest false positive rate, demonstrating its capability to accurately identify signal events while minimizing errors, underscoring its reliability and precision.

Data Analysis & Data Preprocessing Methods

In the initial phase of the study, an extensive exploratory data analysis (EDA) was conducted to gain a thorough understanding of the data structure and the relationships between different features. This process involved examining the distributions of numeric features for both signal and background events using density plots and histograms. Through this analysis, key features such as DER_mass_MMC and DER_deltar_tau_lep were identified as significant indicators, showing clear distinctions between signal and background events. These visualizations were crucial in pinpointing which features would be most beneficial for the subsequent classification models.

Preprocessing steps were essential to ensure the data was optimally prepared for machine learning algorithms. One critical step was checking for multicollinearity among the features, which can negatively impact model performance by introducing redundancy. This was achieved by computing a correlation matrix with a threshold of 0.75 to flag highly correlated features. Features exhibiting high multicollinearity were either removed or combined to streamline the dataset. Additionally, a StandardScaler was applied to standardize the features, ensuring they had a mean of 0 and a standard deviation of 1. This normalization process was vital for stabilizing the learning process, enhancing the convergence of the machine learning algorithms, and ultimately improving the predictive accuracy and robustness of the models.
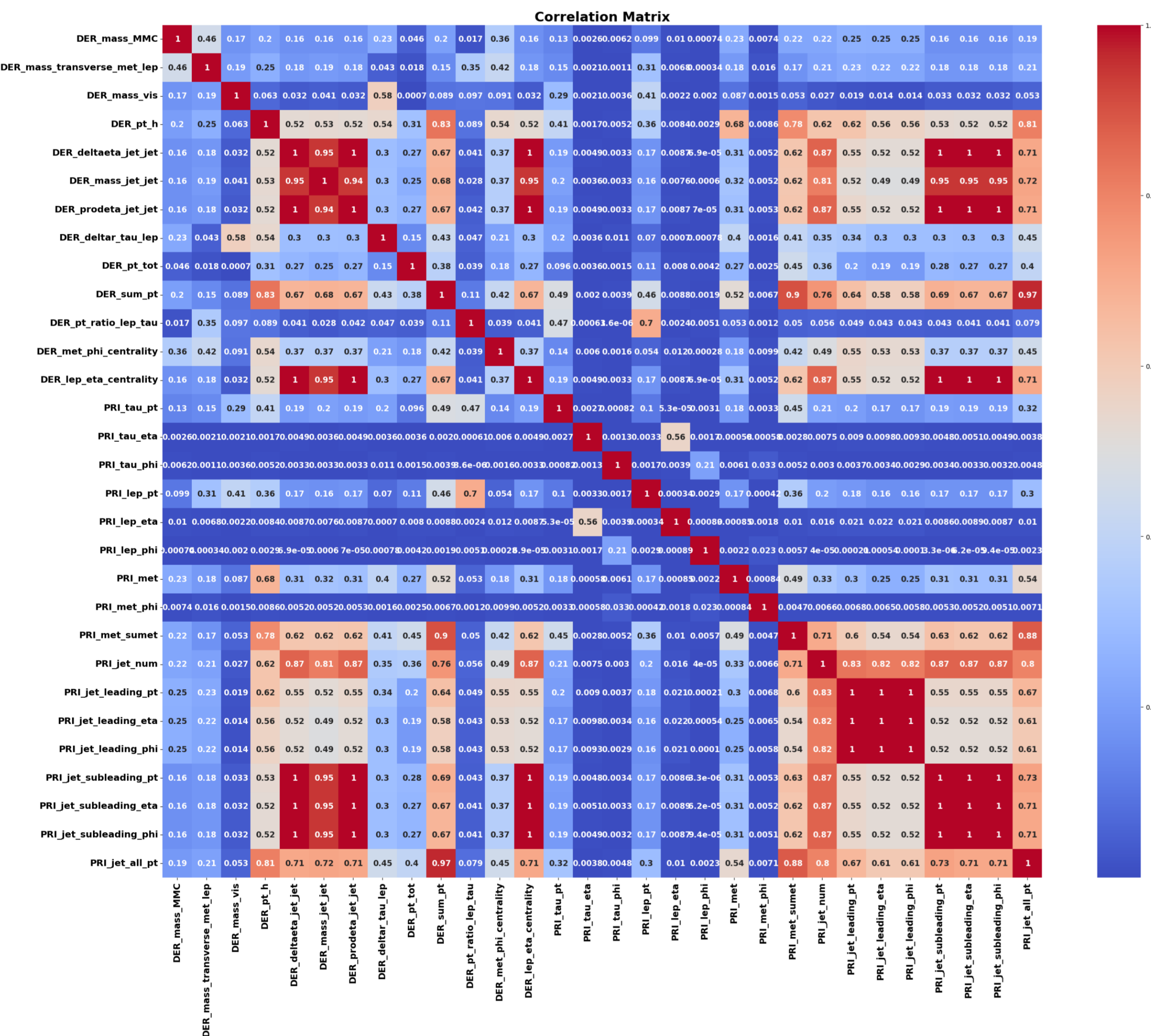

Fig1. Correlation Matrix for the multicollinearity

Multicollinearity was checked from the confusion matrix and those with correlations greater than 0.75 were discarded and we were left with the following features:

Table 1. The features of the vectors that were selected for training the model.

DER_mass_MMC, DER_mass_transverse_met_lep, DER_mass_vis, DER_deltar_tau_lep, DER_pt_tot, DER_pt_ratio_lep_tau, DER_met_phi_centrality, PRI_tau_pt, PRI_tau_eta, PRI_tau_phi, PRI_lep_pt, PRI_lep_eta, PRI_lep_phi, PRI_met, PRI_met_phi

Machine Learning Model Output

Several machine learning algorithms, including linear and radial support vector machines (SVM), logistic regression, k-nearest neighbors (KNN), XGBoost, and AdaBoost, were employed to differentiate between signal and background events. Hyperparameter tuning was conducted for each model to optimize performance. Their effectiveness was evaluated using classification reports, ROC curves, and AUC scores. The XGBoost classifier outperformed the others, achieving the highest AUC score of $0.84 \pm 1.9 \times 10^{-3}$. This superior performance highlights XGBoost's accuracy, consistency, and stability, making it the most effective model in this study.
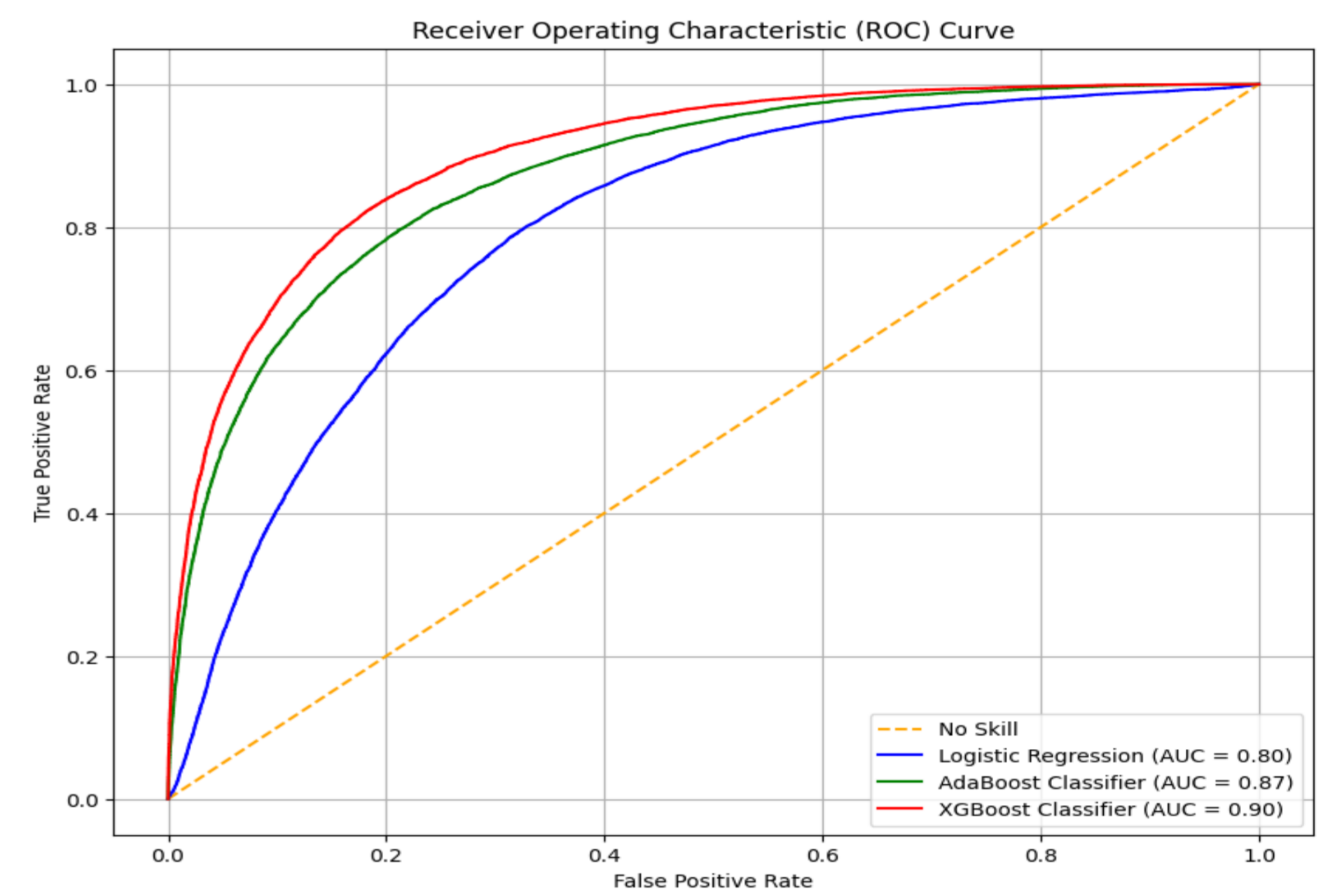

Fig2. ROC Curve for Logistic Regression, AdaBoost and XGBoost Classifier

The calibration plot for the XGBoost classifier aligns closely with the diagonal line, indicating accurate predicted probabilities that match actual outcomes, confirming the model's reliability.
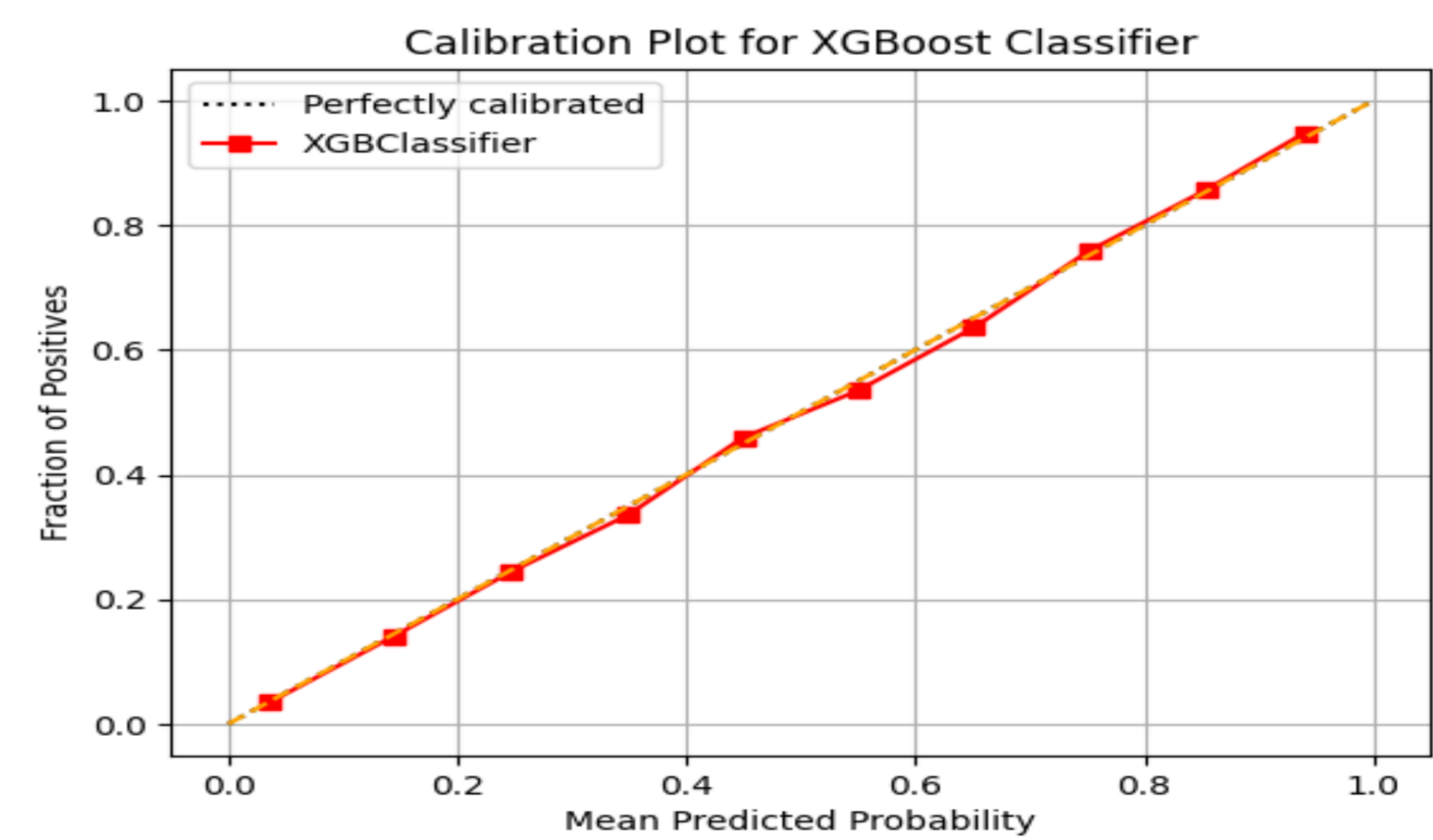

Fig2. Calibration Plot for XGBoost Classifier

The feature importance plot for the XGBoost classifier identifies DER_mass_MMC, DER_deltar_tau_lep, DER_mass_transverse_met_lep, DER_pt_tot, and PRI_met as the top features. DER_mass_MMC is the most influential, indicating its critical role in distinguishing signal and background events. This helps in understanding the key features driving the model's predictions.
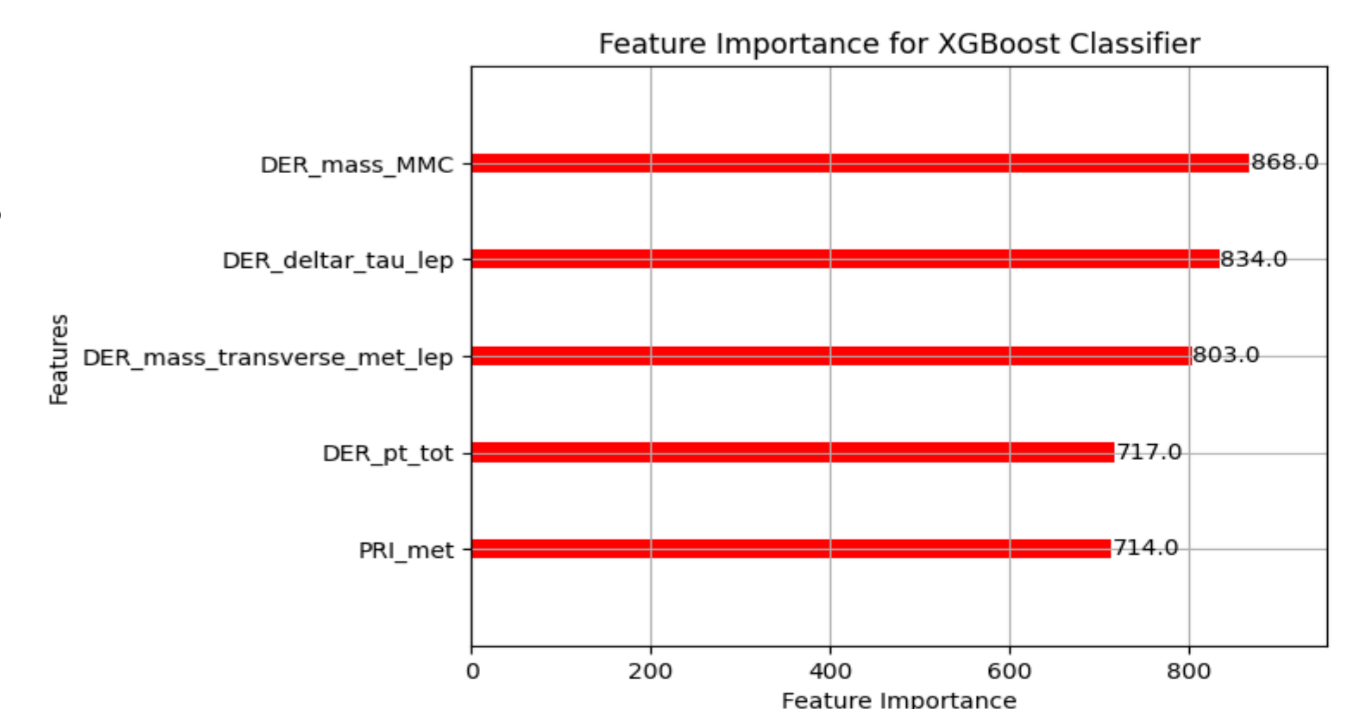

Fig3. Feature Importance Plot for XGBoost Classifier

KAYNAKÇA

[1] Bat, A., (2023), An Educational Approach to Higgs Boson Hunting Using Machine Learning Classification Algorithms on ATLAS Open Data, doi.org/10.28979/jarnas.1242840

[2] ATLAS Collaboration. (2014). Dataset from the ATLAS Higgs Boson Machine Learning Challenge 2014. January 2022 tarihinde opendata. Open Data. Retrieved January 16, 2023, from http://opendata.cern.ch/record/328.

[3] Chen, T., & Guestrin, C. (2016). XGBoost: A Scalable Tree Boosting System. In Proceedings of the 22nd ACM SIGKDD. International Conference on Knowledge Discovery and Data Mining, (pp. 785–794). New York, NY, USA: ACM. https://doi.org/10.1145/2939672.2939785

2023-2024 Bahar Yarıyılı FİZİK BÖLÜMÜ

Quantum Measures and Quantum Darwinism: A Study on Quantumness and Classicality

Akif Koç 19022604

Danışman: Prof. Dr. Kutsal Bozkurt

ABSTRACT

This paper explores the theory of Quantum Darwinism, which Wojciech H. Zurek put forth to explain how quantum phenomena give rise to classical reality. To improve our comprehension of the quantum-to-classical transition, ideas from Quantum Information Theory and Open Quantum Systems are investigated in conjunction with Quantum Darwinism. This work discusses how classical objectivity emerges from the quantum by examining quantum measures such as Von Neumann entropy and Quantum Mutual Information and the dynamics of open quantum systems. The results imply that non-classical properties persist even though Quantum Darwinism is essential to the emergence of classical reality, pointing out the need for additional testing with quantum metrics such as quantum discord.

INTRODUCTION

Quantum mechanics, governing microscopic scales, often clashes with classical macroscopic understanding. This study explores Quantum Darwinism, a framework explaining the emergence of classical reality from quantum phenomena, proposed by Wojciech H. Zurek. Along with Quantum Darwinism, we aim to get acquainted with concepts of Quantum Information Theory and Open Quantum Systems.

Quantum mechanics introduces unique concepts like superposition and entanglement, challenging our classical view. Quantum Darwinism suggests the environment plays a key role by proliferating information about specific "pointer states," allowing multiple observers to access consistent information, leading to objective classical reality.

This research examines open quantum systems, quantum measures, focusing on how quantum measures gives information about the system. By studying information redundancy in the environment, it reveals how certain states become classical through robust observability. These findings enhance our understanding of the quantum-to-classical transition.

Framework

Vector and Density Matrix Representation
Quantum State Representation
State Vector (Ket): A pure quantum state is represented by a vector $|\psi\rangle$ in a Hilbert space.
$$|\psi\rangle = \alpha|0\rangle + \beta|1\rangle$$
where α and β are complex numbers with $|\alpha|^2 + |\beta|^2 = 1$.
Density Matrix: A more general representation, suitable for both pure and mixed states, is the density matrix ρ. For a pure state $|\psi\rangle$:
$$\rho = |\psi\rangle\langle\psi|$$
For a mixed state, represented as a statistical ensemble of pure states $\{p_i, |\psi_i\rangle\}$:
$$\rho = \sum_i p_i |\psi_i\rangle\langle\psi_i|$$

Quantum Measures
Von Neumann Entropy
The von Neumann entropy $S(\rho)$ quantifies the uncertainty or mixedness of a quantum state.
$$S(\rho) = -\text{Tr}(\rho\log\rho)$$

Quantum Mutual Information
Quantum mutual information $I(A:B)$ measures the total correlations between two subsystems A and B.
$$I(A:B) = S(\rho_A) + S(\rho_B) - S(\rho_{AB})$$
where $\rho_A = \text{Tr}_B(\rho_{AB})$ and $\rho_B = \text{Tr}_A(\rho_{AB})$ are the reduced density matrices. $\text{Tr}_A(\rho_{AB})$ is called the partial trace of A over system AB, is a useful tool to bipart a composite system.

Quantumness and Classicality
Quantum Coherence
Quantum coherence refers to the superposition of states and is essential for quantum phenomena like interference. It is a measure of off-diagonal elements of the density matrix in a given basis:
$$C(\rho) = \sum_{i \neq j} |\rho_{ij}|$$

Quantum Entanglement
Quantum entanglement is a form of non-classical correlation between subsystems that cannot be described by local hidden variables. Entanglement entropy, defined as the von Neumann entropy of the reduced density matrix of a subsystem.

Classicality and Decoherence
Classicality emerges through the process of decoherence, where quantum superpositions are effectively reduced to classical mixtures due to interactions with the environment. Suppression of off-diagonal elements in the density matrix in the preferred basis (pointer states).

Quantum Darwinism
Quantum Darwinism describes how classical objectivity emerges from the quantum substrate by proliferating redundant information about certain states into the environment. It is measured through redundancy of information, quantified by mutual information between the system and multiple environmental fragments.

Analytical System Model

Dynamics for system over continuous time t:

Figure 1.

$$|\Psi\rangle = e^{-iNJ_z t}\alpha\,|00\rangle_{S_1 S_2} \bigotimes_{k=1}^{N}\frac{1}{\sqrt{2}}\left(e^{-i2J_{SE}t}\,|0\rangle_k + e^{i2J_{SE}t}\,|1\rangle_k\right)$$

$$+ e^{iNJ_z t}\left[\beta\cos(Jt) - i\gamma\sin(Jt)\right]|01\rangle_{S_1 S_2}\bigotimes_{k=1}^{N}\frac{1}{\sqrt{2}}\left(|0\rangle_k + |1\rangle_k\right)$$

$$+ e^{iNJ_z t}\left[\gamma\cos(Jt) - i\beta\sin(Jt)\right]|10\rangle_{S_1 S_2}\bigotimes_{k=1}^{N}\frac{1}{\sqrt{2}}\left(|0\rangle_k + |1\rangle_k\right)$$

$$+ e^{-iNJ_z t}\delta\,|11\rangle_{S_1 S_2}\bigotimes_{k=1}^{N}\frac{1}{\sqrt{2}}\left(e^{i2J_{SE}t}\,|0\rangle_k + e^{-i2J_{SE}t}\,|1\rangle_k\right)$$
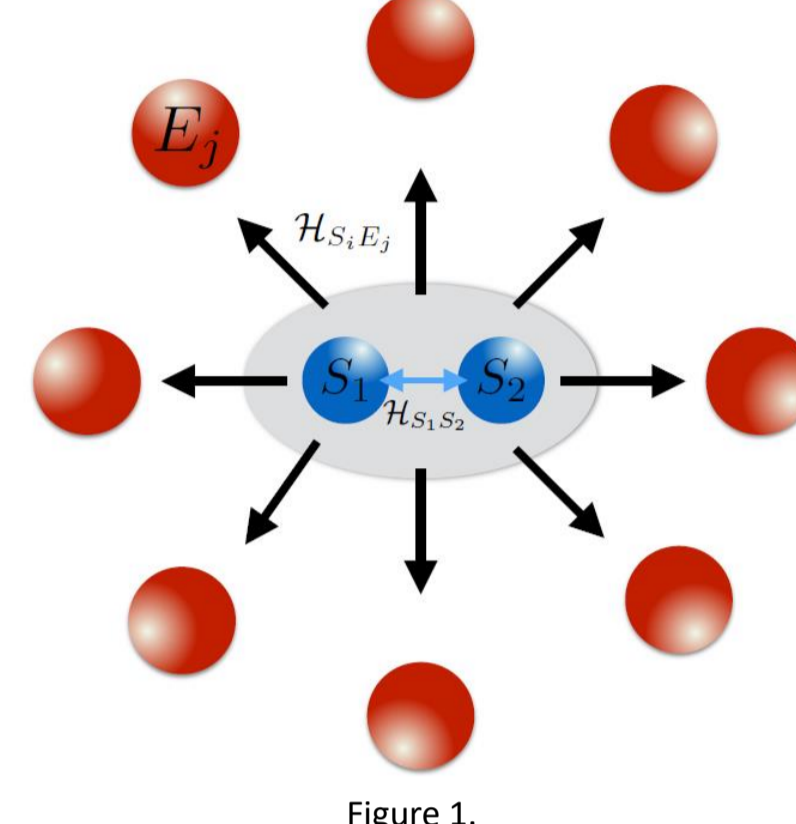
System Dynamics in Mathematica

```
In[7]:= (*tensor product for n-qubit environment*)
    tp[expr_, k_] := If[k == 1, expr, Flatten[KroneckerProduct @@ Table[expr, k]]]
In[8]:= (*dynamics of the whole S-E state after time t*)
    Φ[n_, J_, Jse_, t_] :=
    Exp[-i * n * Jz * t] * α * Flatten[KroneckerProduct[ψ00, tp[1/Sqrt[2] * (Exp[-i * 2 * Jse * t] * ψ0 + Exp[i * 2 * Jse * t] * ψ1), n]]] +
    Exp[i * n * Jz * t] * (β * Cos[J * t] - i * γ * Sin[J * t]) * Flatten[KroneckerProduct[ψ01, tp[Φ₁, n]]] +
    Exp[i * n * Jz * t] * (γ * Cos[J * t] - i * β * Sin[J * t]) * Flatten[KroneckerProduct[ψ10, tp[Φ₁, n]]] +
    Exp[-i * n * Jz * t] * δ *
        Flatten[KroneckerProduct[ψ11, tp[1/Sqrt[2] * (Exp[i * 2 * Jse * t] * ψ0 + Exp[-i * 2 * Jse * t] * ψ1),
        n]]] /. :α->Cos[θ₁]*Cos[θ₂], .β->Cos[θ₁]*Sin[θ₂], .γ->Sin[θ₁]*Cos[θ₂], .δ->Sin[θ₁]*Sin[θ₂], .θ₁->π/6, .θ₂->π/6, .Jz->0;
In[10]:= (*Density matrix and reduced densiyt matrices for system and system-environment*)
    ρ[n_, t_] := KroneckerProduct[Φ[n, 10, 1, t], Conjugate[Φ[n, 10, 1, t]]];
    rdm[n_, t_] := TraceSystem[ρ[n, t], Range[3, n + 2]];
    rdm3[n_, t_] := TraceSystem[ρ[n, t], Range[4, n + 2]];
In[14]:= (*von Neumann Entropy, mutual information between system-environment and system qubits*)
    S[M_] := Block[{ev}, ev = Chop[Abs[Eigenvalues[M]]] /. 0->Nothing; Σ(k=1)^Length[ev] -ev[[k]] * Log[2, ev[[k]]]];
    miSE[n_, t_] := Module[{rhoSE, rhoS, rhoE}, rhoSE = rdm3[n, t]; rhoS = rdm[n, t]; rhoE = TraceSystem[rdm3[n, t], {1, 2}];
        S[rhoS] + S[rhoE] - S[rhoSE]]
    mi[n_, t_] := Module[{rhoS, rho1, rho2}, rhoS = rdm[n, t]; rho1 = TraceSystem[rhoS, {2}]; rho2 = TraceSystem[rhoS, {1}];
        S[rho1] + S[rho2] - S[rhoS] // FullSimplify // N]
In[19]:= coh[M_] := (Total[Abs[Flatten[M]]] - 1)/2 // FullSimplify // N(*coherence*)

In[21]:= (*Entropy and Mutual Information plots*)
    Plot[{S[rdm[6, t]], miSE[6, t]}, {t, 0, π / 2}, AxesLabel → {"t", "I,S"}, PlotLegends → "Expressions"]
In[22]:= (*coherence plots for system and environment qubits*)
    Plot[{coh[rdm[6, t]], coh[TraceSystem[rdm3[6, t], {1, 2}]]},
        {t, 0, π / 2}, AxesLabel → {"t", "C"}, PlotRange → {All, {0, All}}]
```
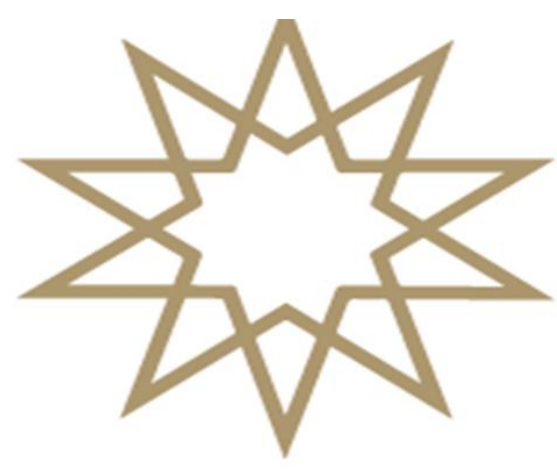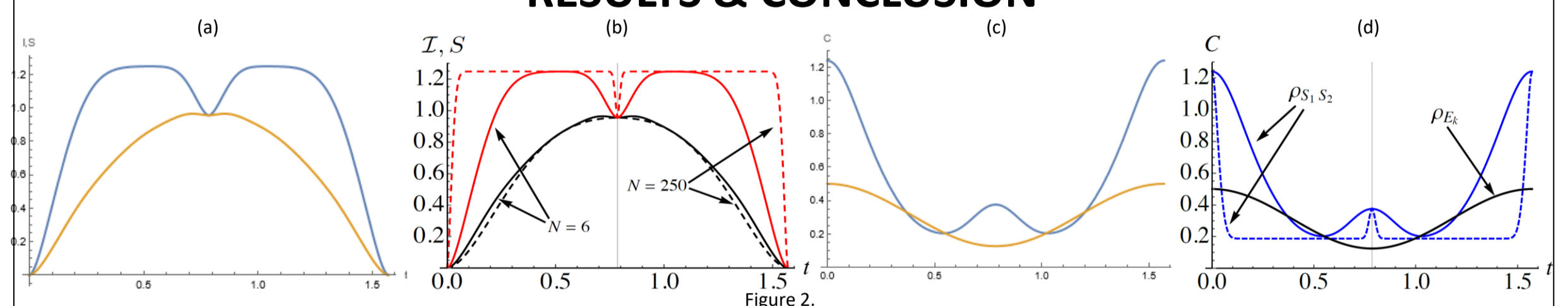
RESULTS & CONCLUSION

Figure 2.

Figure 2(a) and 2(c) are from our computations with N = 6 environment qubits. Figure 2(b) and 2(d) are from the article "Quantum Darwinism in a Composite System: Objectivity versus Classicality" by Çakmak et al., with N = 6 and N = 250 qubits. We were not able to compute for N = 250 environment qubits. Both results show that $I(\rho_{S_1 S_2 : E_k}) = S(\rho_{S_1 S_2})$ at time $t = \pi/4$, this implies quantum darwinism. However, coherence plots show that non-classical properties are present in the system even with darwinistic behviour. Another possible deduction can be made from Figure 2 is, mutual information is inversely related with coherence of environmental qubit. Quantum measures like quantum discord is needed to further assess quantumness, classicality, and objectivity.

REFERENCES

[1] Watrous, J. (2018). The Theory of Quantum Information. Cambridge University Press. ISBN: 978-1-107-18056-7.
[2] Zurek, W. H. (2003). Decoherence, einselection, and the quantum origins of the classical. Reviews of Modern Physics, 75(3), 715-775.
[3] Çakmak, B., Müstecaplıoğlu, Ö. E., Paternostro, M., Vacchini, B., & Campbell, S. (2021). *Quantum Darwinism in a Composite System: Objectivity versus Classicality*. Entropy, 23(8), 995. https://doi.org/10.3390/e23080995.

YTU FEN EDEBİYAT FAKÜLTESİ

2023-2024 SPRİNG SEMESTER PHYSİCS DEPARTMENT

Synthesizing and Analyzing Blue Light in Quantum Nanotubes

Çisem Küçükyörük 18022034

Danışman:Prof.Dr.Orhan Özdemir

SUMMARY

The ability of carbon quantum dots (CQDs) and boron nitride quantum dots (BNQDs) to emit blue light is examined in this thesis. Both CQDs and BNQDs show high blue light emission under UV light, according to photoluminescence (PL) tests. Intensity-wavelength graphs reveal that both nanomaterials achieve peak emission values within the characteristic blue light wavelength range of 450-495 nm. Additionally, green light emission was observed under certain conditions, with maximum values in the 495-570 nm range. These findings suggest that quantum dots have the potential to emit light across a broad spectrum of colors. Overall, CQDs and BNQDs are identified as strong candidates for blue light applications due to their high photoluminescence efficiency and chemical stability. Future research should focus on optimizing synthesis methods for these materials and conducting more detailed studies on their biocompatibility profiles.

Unique Optical and Electronic Properties of Carbon and Boron Nitride Quantum Dots for Blue Light Emission

Carbon quantum dots (CQDs) and boron nitride quantum dots (BNQDs) are preferred due to their unique optical and electronic properties. CQDs are ideal for optoelectronic and biosensor applications due to their excellent photoluminescence properties, stability, and biocompatibility. BNQDs, on the other hand, exhibit high chemical stability and thermal resistance, making them suitable for environmental and biomedical applications.
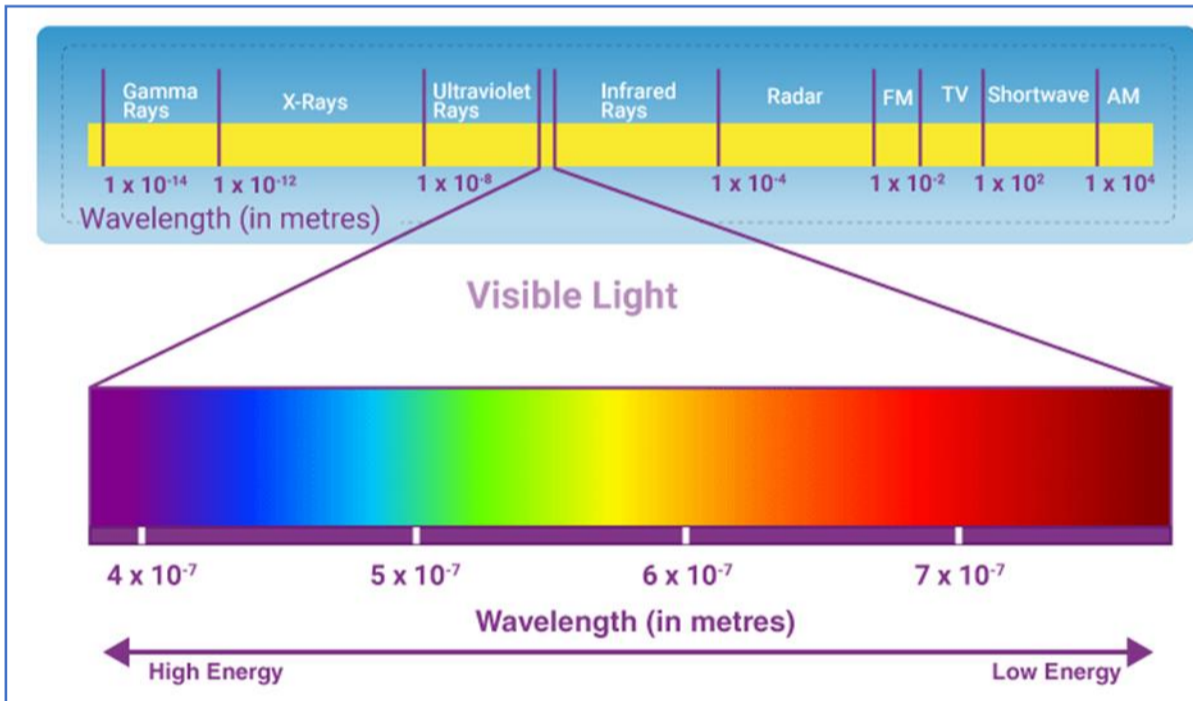
The production of blue light is achieved by exciting quantum dots. When these dots are excited at a specific wavelength, they emit photons due to changes in energy levels. The photoluminescence properties of CQDs and BNQDs are based on the principle of electrons emitting light from different energy levels.

In our study, we determined that the quantum dots synthesized using the hydrothermal method have a strong blue light emission capacity.

Experiment

In this study, boron nanotubes (BNTs) were prepared using simple chemical synthesis methods. Under experimental conditions, a specific amount of boron compound and solvent was mixed in a reaction vessel. The mixture was heated to specific temperatures for set durations, then cooled and centrifuged. The obtained BNTs were purified by filtration. The Raman spectra of the obtained samples were analyzed to confirm the presence of the nanostructure. The Raman spectrum showed the D band (1365 cm-1) and G band (1440 cm-1), verifying the existence of the nanostructure.

To examine the photoluminescence (PL) properties, CQD, CNT, and BNT samples were prepared and excited at different wavelengths (e.g., 280 nm, 365 nm). The PL spectra for each sample were recorded, and the changes in PL emission depending on the excitation wavelength were analyzed. Intensity-wavelength measurements were conducted using a spectrometer, which provided intensity-wavelength graphs for CQD, CNT, and BNT samples. The relationship between intensity and wavelength for each sample was analyzed to detail the photoluminescence properties. These analyses revealed that when excited with a UV light source, the samples exhibited emissions not only in the blue region but also in the green and red regions. These findings highlight the potential of nanotubes for multicolor light-emitting applications in optoelectronic devices and imaging systems.

Equipment Used

The experimental studies utilized the spectrometer devices shown in the images. The spectrometer allowed for detailed analysis of the photoluminescence (PL) and intensity-wavelength measurements, as seen in the display of analysis results on the screen. These spectrometers enabled a comprehensive analysis of the optical properties of the samples. Consequently, the light-emitting capabilities of the nanomaterials across different wavelengths were successfully analyzed, demonstrating their potential for various advanced applications,
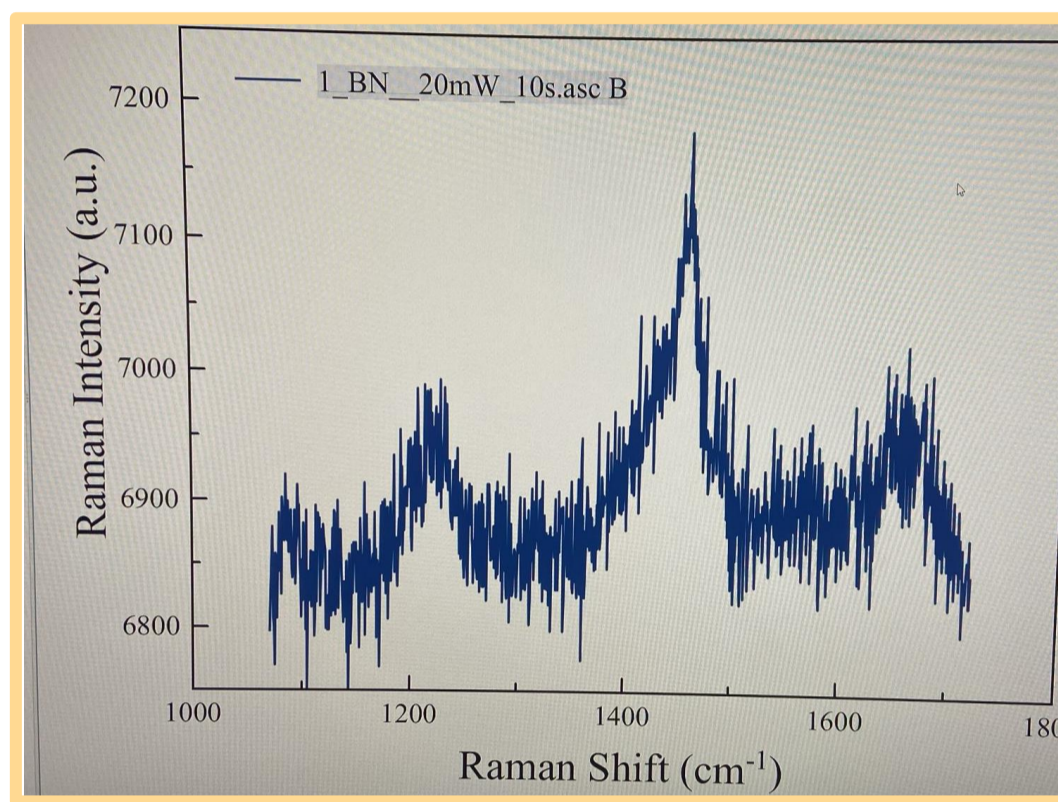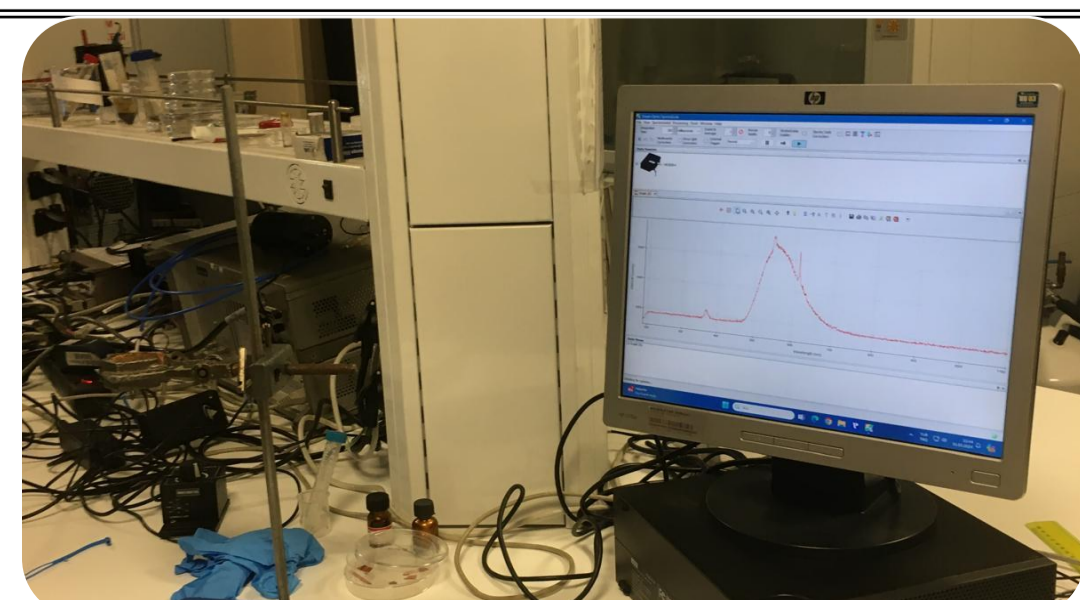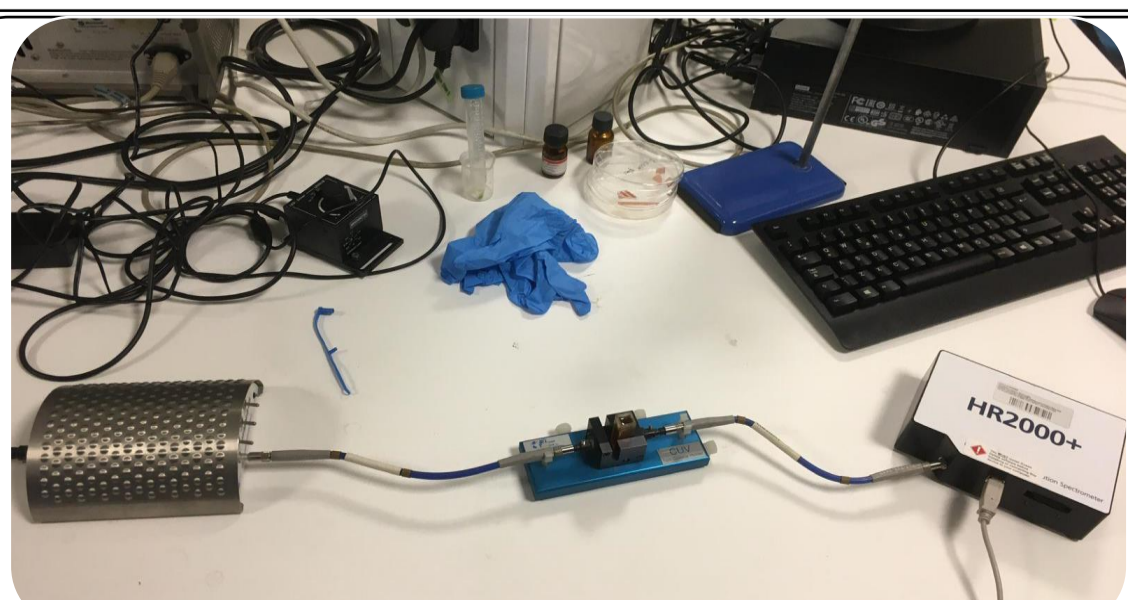
A specific amount of boron compound and solvent was mixed in a reaction vessel.
The mixture was heated at specific temperatures and durations.
After the reaction was complete, the samples were cooled and centrifuged.
The obtained BNTs were purified by filtration.
Raman spectrum over the sol is illustrated in Figure 2 and proves the existence of the nano structure.
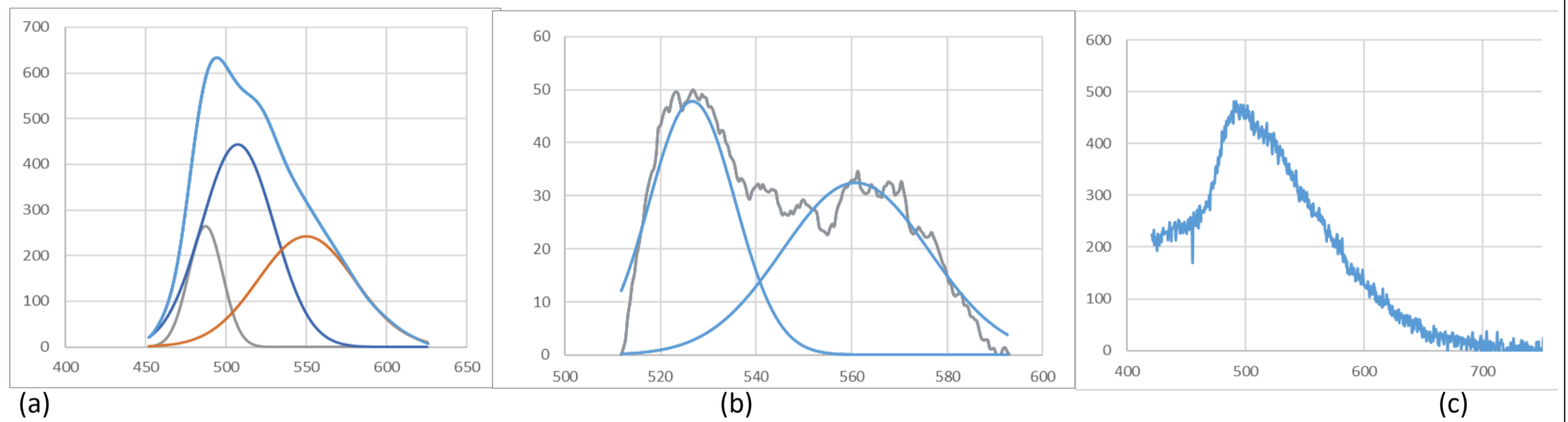

Figure X. PL spectrum of (a) carbon nanotup film, (b) BN nanotup, excited with 365 nm UV light source. Note that not only the blue color but also green and red color exits in the spectrum, depicted in Figure X-c.

The photoluminescence (PL) spectra of carbon nanotube and boron nitride nanotube (BN nanotube) films, excited with 365 nm UV light, show that these materials can emit light across a broad wavelength range. The carbon nanotube spectrum displays emissions in the blue (450-500 nm), green (500-550 nm), and red (600-650 nm) regions, while the BN nanotube spectrum shows strong emissions in the blue (450-480 nm) and green (520-580 nm) regions. Both materials exhibit multicolor emissions when excited with UV light, demonstrating their capability to emit light in various colors. These findings highlight the potential applications of nanotubes in optoelectronic devices, imaging systems, and multicolor light-emitting applications, suggesting that further detailed studies of their photoluminescence properties could lead to significant advancements.

Results and Discussion

This study investigates the blue light emission capabilities of carbon quantum dots (CQDs) and boron nitride quantum dots (BNQDs), emphasizing their potential for various technological applications. Photoluminescence (PL) measurements confirmed that both CQDs and BNQDs emit strong blue light within the 450-495 nm range, and green light under specific conditions (495-570 nm).

Additionally, carbon nanotube and boron nitride nanotube films emit light across a broad spectrum when excited with 365 nm UV light. Carbon nanotubes show emissions in the blue (450-500 nm), green (500-550 nm), and red (600-650 nm) regions, while boron nitride nanotubes display strong emissions in the blue (450-480 nm) and green (520-580 nm) regions. These materials demonstrate multicolor emissions, highlighting their potential in optoelectronic devices, imaging systems, and multicolor light-emitting applications. Detailed studies could lead to significant advancements, showing great promise for advanced technological applications due to their ability to emit light across a wide spectrum of colors.

REFERENCES

(1)Bingül, S., Önal, Y., & Gökbulut, İ. (2023). Geleceğin Malzemesi Olarak Karbon Kuantum Noktacık Ve Uygulama Alanları. Avrupa Bilim ve Teknoloji Dergisi, (50), 23-29. DOI: 10.31590/ejosat.1175104.

(2)Durmuşoğlu, E. G. "Teknik Yazı: Kuantum Nokta." TMMOB Metalurji ve Malzeme Mühendisleri Odası.

(3)Bin, Z., ve diğerleri. (2015). "Air Stable Organic Salt As an n-Type Dopant for Efficient and Stable Organic Light-Emitting Diodes." ACS Applied Materials & Interfaces. DOI: 10.1021/acsami.5b00839.

(4)Sarkar, S., Banerjee, D., Ghorai, U.K., ve Das, N.S. (2016). "Size dependent photoluminescence property of hydrothermally synthesized crystalline carbon quantum dots." Journal of Luminescence,

YTÜ FEN EDEBİYAT FAKÜLTESİ

PHYSICS DEPARTMENT

THE ROLE OF SOLAR ENERGY IN ELECTRICITY GENERATION

İPEK DİVAN 16022011

Advisor: Doç. Dr. Fatma Pınar CHOI

ABSTRACT This thesis explores the importance and potential of solar energy as a critical component in addressing global energy needs. It examines the technological advancements, economic benefits, and environmental impacts of solar energy, emphasizing its ability to reduce reliance on fossil fuels and lower greenhouse gas emissions. The thesis provides an in-depth analysis of photovoltaic (PV) technology, including the physics behind solar cells and the various generations of solar cells. It also covers recent innovations in solar energy technology, energy storage solutions, and the economic and social challenges associated with solar energy deployment.

INTRODUCTION

Global energy demand is continuously increasing every year due to population growth and economic development. Global energy consumption was significantly increased by 69.22% due to an increasing world population by 47.67% from 1990 to 2020.[1] Because of the increasing global energy needs and the rising demands for electricity, traditional fossil fuel sources are highlighted for their various limitations, including environmental impacts, greenhouse gas emissions, resource depletion, geopolitical challenges, health impacts, climate change effects, and economic considerations. The thesis statement sets the stage for a comprehensive exploration of solar energy as a viable alternative to address these issues.

A solar cell, also referred to as a photovoltaic cell or PV cell, is an electrical device that utilizes the photovoltaic effect to convert light energy into electrical energy. A solar cell is essentially a p-n junction diode. Solar cells are a type of photoelectric cell, which refers to a device that undergoes changes in its electrical properties, such as current, voltage, or resistance, when it is exposed to light.

An important metric of any photovoltaic cell is its efficiency. This is usually defined as the ratio of energy we get out of the cell to the energy put into it by sunlight. We can calculate it using many of the parameters above, by remarking that the input power is the ideal Isc x Voc multiplied by the fill factor. If we know our input power density (or irradiance) of the sun, Ps, we can then calculate solar cell efficiency, which is the division of the two shown in (1).

$$\eta = \frac{I_{sc}V_{oc}FF}{P_s} \quad (1)$$

Solar energy is primarily captured using two methods: Photovoltaics (PV) and Concentrated Solar Power (CSP). PV systems use semiconductor materials to convert sunlight directly into electricity, while CSP systems use mirrors or lenses to focus sunlight, creating heat that generates power.
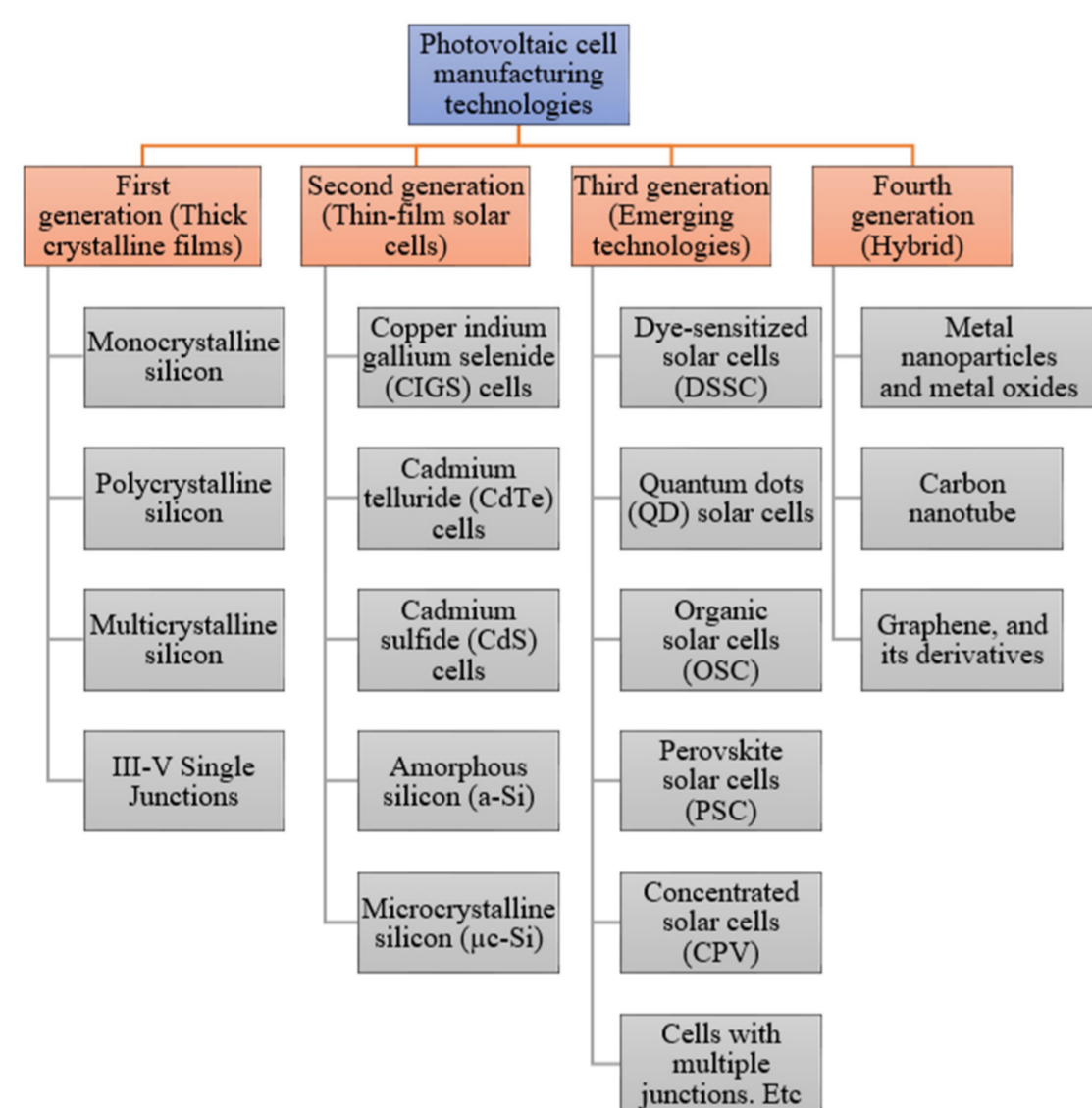

Figure 1: Solar cell generations and members [2]

There are several technologies involved with the manufacturing process of photovoltaic cells, using material modification with different photoelectric conversion efficiencies in the cell components. Due to the emergence of many non-conventional manufacturing methods for fabricating functioning solar cells, photovoltaic technologies can be divided into four major generations, which is shown in Figure 1. [3]

First Generation: This category includes photovoltaic cell technologies based on monocrystalline and polycrystalline silicon and gallium arsenide (GaAs)

Second Generation: This generation includes the development of first-generation photovoltaic cell technology, as well as the development of thin film photovoltaic cell technology from "microcrystalline silicon (μc-Si) and amorphous silicon (a-Si), copper indium gallium selenide (CIGS) and cadmium telluride/cadmium sulfide (CdTe/CdS) photovoltaic cells".

Third Generation: This generation counts photovoltaic technologies that are based on more recent chemical compounds. In addition, technologies using nanocrystalline "films," quantum dots, dye-sensitized solar cells, solar cells based on organic polymers, etc., also belong to this generation.[2]

Fourth Generation: This generation includes the low flexibility or low cost of thin film polymers along with the durability of "innovative inorganic nanostructures such as metal oxides and metal nanoparticles or organic-based nanomaterials such as graphene, carbon nanotubes and graphene derivatives" [3]

Photovoltaic (PV) systems are very adaptable and may be easily put on many surfaces, including residential rooftops and expansive solar farms, due to their scalability. Furthermore, these devices exhibit cheap operational and maintenance expenses due to their lack of moving components and minimum maintenance requirements. Furthermore, photovoltaic (PV) systems have the ability to directly convert sunlight into electricity, resulting in no emissions being released during its operation. This characteristic not only helps in reducing air pollution but also contributes to the mitigation of greenhouse gas emissions. Furthermore, improvements in photovoltaic (PV) technology have greatly enhanced their efficiency and reduced expenses, hence enhancing the accessibility and economic feasibility of solar energy. Ultimately, photovoltaic (PV) systems offer the advantage of energy self-sufficiency, diminishing the need for grid electricity and increasing energy stability for individuals.

Perovskite is much better at absorbing light than crystalline silicon and can even be tuned to use regions of the solar spectrum largely inaccessible to silicon photovoltaics, as shown in Figure 2.
Silicon remains the dominant material in the solar energy market because it is known and trusted, and perovskites alone are yet to meet the standards in performance set by this material.
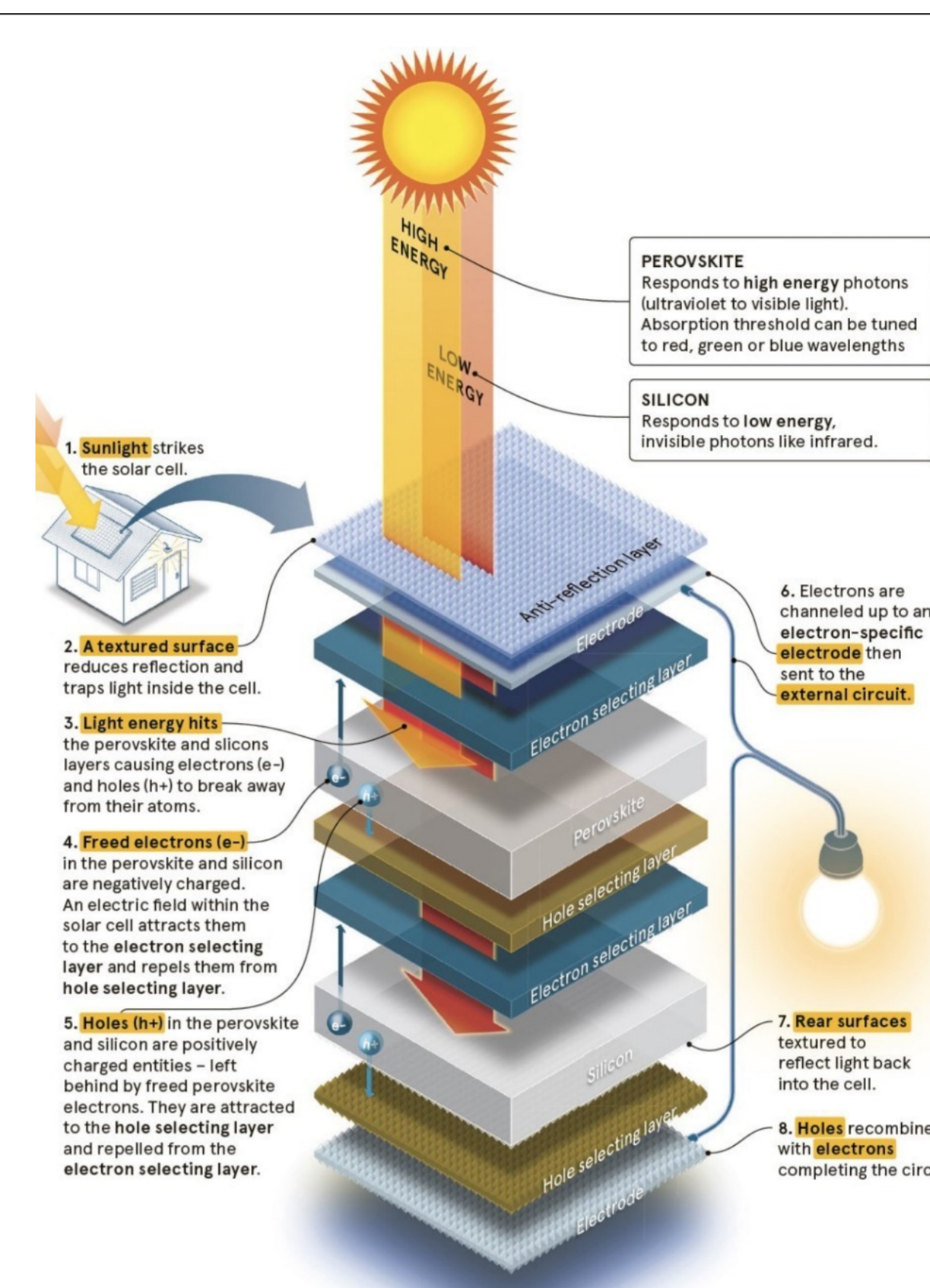

Figure 2: A silicon/perovskite solar cell [4]

Concentrated Solar Power (CSP) has numerous benefits within the field of renewable energy. First and foremost, Concentrated Solar Power (CSP) systems have the capability to produce energy even in the absence of sunlight by making use of thermal storage systems, as shown in Figure 3. These systems store heat that may be utilized during periods of cloudiness or at night. Furthermore, Concentrated Solar Power (CSP) plants have the capability to be seamlessly incorporated into current power plants, resulting in a hybrid approach that improves overall effectiveness and dependability. Furthermore, Concentrated Solar Power (CSP) technology typically requires a less land area per unit of power generated in comparison to photovoltaic systems, therefore making it a more efficient choice in terms of space utilization. CSP systems have the advantage of generating very low levels of greenhouse gas emissions while in operation, making a significant contribution to the reduction of environmental pollution and the global effort to combat climate change.
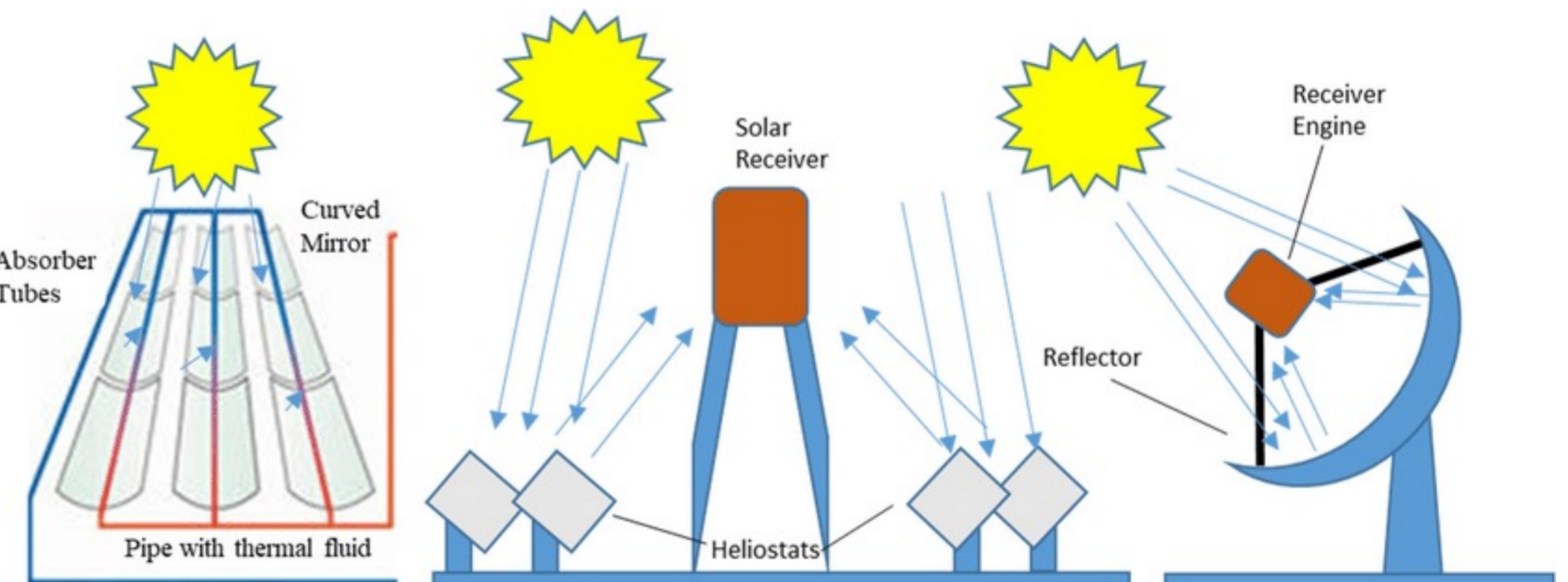

Figure 3:The main technologies of concentrated solar power systems [5]

In conclusion, solar energy represents a vital solution to the growing global demand for electricity and the urgent need to transition away from fossil fuels. The significant advancements in photovoltaic (PV) technology have enhanced the efficiency and reduced the costs of solar energy systems, making them increasingly viable and accessible. Additionally, concentrated solar power (CSP) offers unique advantages, such as the ability to generate electricity even during non-sunny periods through thermal storage. Both PV and CSP systems contribute to reducing greenhouse gas emissions and environmental pollution. The integration of solar energy into existing power grids, along with improvements in energy storage solutions, supports a stable and reliable energy supply. Despite the economic and social challenges, such as installation costs and land use considerations, the potential benefits of solar energy are immense. With continuous innovation, supportive policies, and strategic planning, solar energy can play a transformative role in achieving a sustainable and energy-secure future. This thesis underscores the critical importance of embracing solar energy to address the pressing challenges of energy security, environmental sustainability, and climate change.
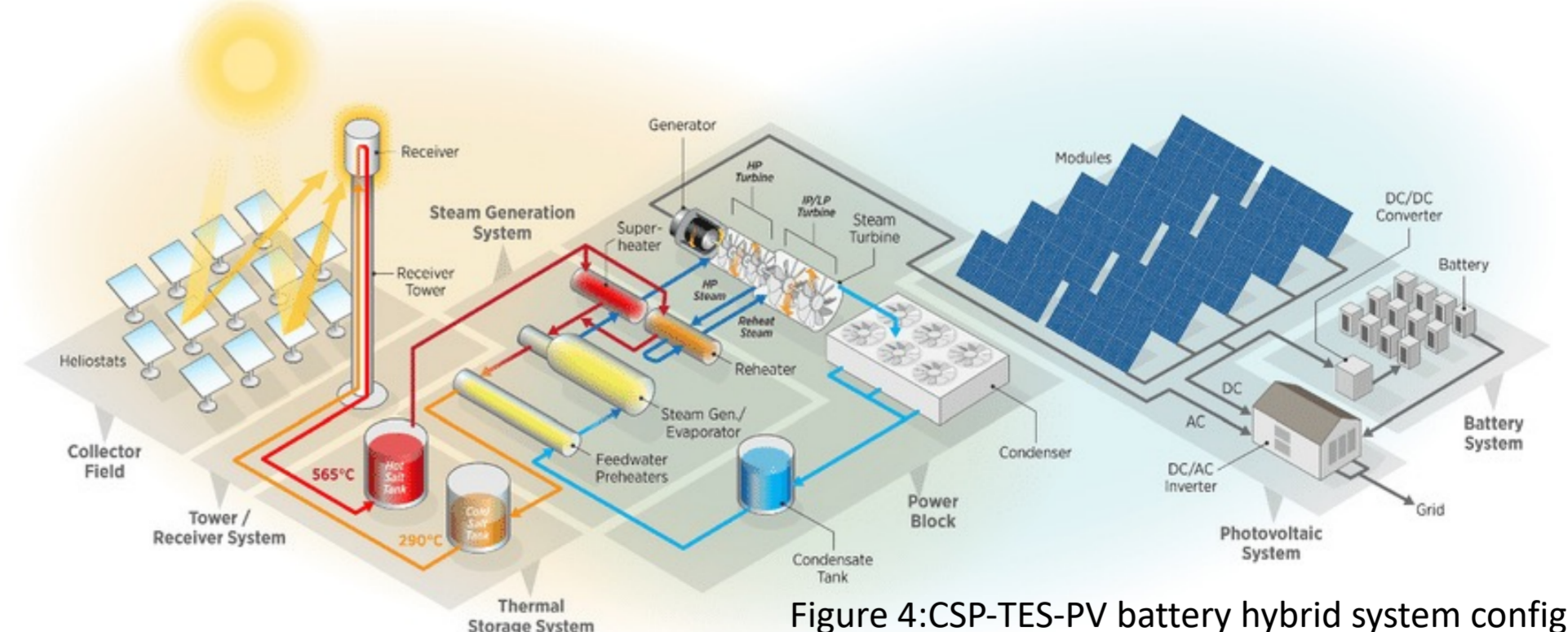

Figure 4:CSP-TES-PV battery hybrid system configuration [6]

REFERENCES

[1] Chanthakett, Apinya, et al. "Hydrogen production from municipal solid waste using gasification method." Hydrogen Energy Conversion and Management. Elsevier, 2024. 103-131.
[2] Pastuszak, Justyna, and Paweł Węgierek. "Photovoltaic cell generations and current research directions for their development." Materials 15.16 (2022): 5542.
[3] Almosni S., Delamarre A., Jehl Z., Suchet D., Cojocaru L., Giteau M., Behaghel B., Julian A., Ibrahim C., Tatry L., et al. Material challenges for solar cells in the twenty-first century: Directions in emerging technologies. *Sci. Technol. Adv. Mater.* 2018;19:336–369. doi: 10.1080/14686996.2018.1433439.
[4] Dodd, G.(2021,0525) Sydney Alumni Magazine, 14, 11
[5] Albarbar, Alhussein, and Abdullah Arar. "Performance assessment and improvement of central receivers used for solar thermal plants." Energies 12.16 (2019): 3079
[6] Hamilton, William T., et al. "Dispatch optimization of concentrating solar power with utility-scale photovoltaics." Optimization and Engineering 21.1 (2020): 335-369.

YTÜ FEN EDEBİYAT FAKÜLTESİ

2023-2024 Bahar Yarıyılı FİZİK BÖLÜMÜ

X8.2 Sınıfı Güneş Patlamasının Mars İyonosferi Üzerindeki Etkilerinin MAVEN Uydu Verileri ile İncelenmesi

Almina DOKUR, 18022025

Danışman: Doç. Dr. Zehra CAN

ÖZET Çalışmamızda, X8.2 sınıfındaki bir Güneş patlaması seçildi ve bu patlamanın Mars iyonosferi üzerindeki etkileri, MAVEN uydusu enstrümanları ile incelendi. 10 Eylül 2017 tarihli koronal kütle atılımı (CME) hem Dünya, hem de Mars yakınlarına bir jeomanyetik fırtına ulaşması nedeniyle özel bir Güneş olayıdır. Özellikle Mars iyonosferi üzerinde, SWEA ve SWIA parametreleri incelendi. Halka açık bilimsel veri kaynakları kullanılmıştır. Uzay hava etkilerinin sonuçları açık şekilde görülmüştür. CME'ye ait Güneş görüntü ve grafikleri, MAVEN uydusuna ait SWEA ve SWIA verileri, WSA-ENLIL simülasyonları ve diğer metodoloji teknikleriyle, MAVEN tarafından kaydedilmiş en güçlü CME olan, Eylül 2017 CME' sinin Mars iyonosferi çevresindeki etkisi tutarlı şekilde desteklendi.

GİRİŞ

Uzay havası, helisofer boyunca güneş parçacığı ve foton koşullarındaki kısa vadeli değişiklik olarak ifade edilebilmektedir. Mars, uzay havası değişimlerine karşı Dünya' ya kıyasla daha duyarlıdır çünkü küresel bir dinamo manyetik alanına sahip değildir. Böylece kendini güneş rüzgar ve fırtınalarından korumakta zorlanmaktadır. Kızıl Gezegen'in uzay havasına verdiği tepki, gezegenimizin dışındaki heliosferde en iyi incelenmiş tepkidir. Mars'ta uzay havasının değişkenliğine dair birçok gözlem yapılmıştır. Bu gözlemlere örnek olarak, güneş fırtınalarına yanıt olarak manyetosferin sıkışması ve yeniden yapılandırılması, artan aurora olasılığı ve auroral elektron enerjileri, parlama ve enerjik parçacık olayları sırasında artan parçacık yağışı, iyonosferik yoğunlukları ve koronal kütle fırlatma olayları sırasında artan iyon kaçışı verilmektedir [1,3].
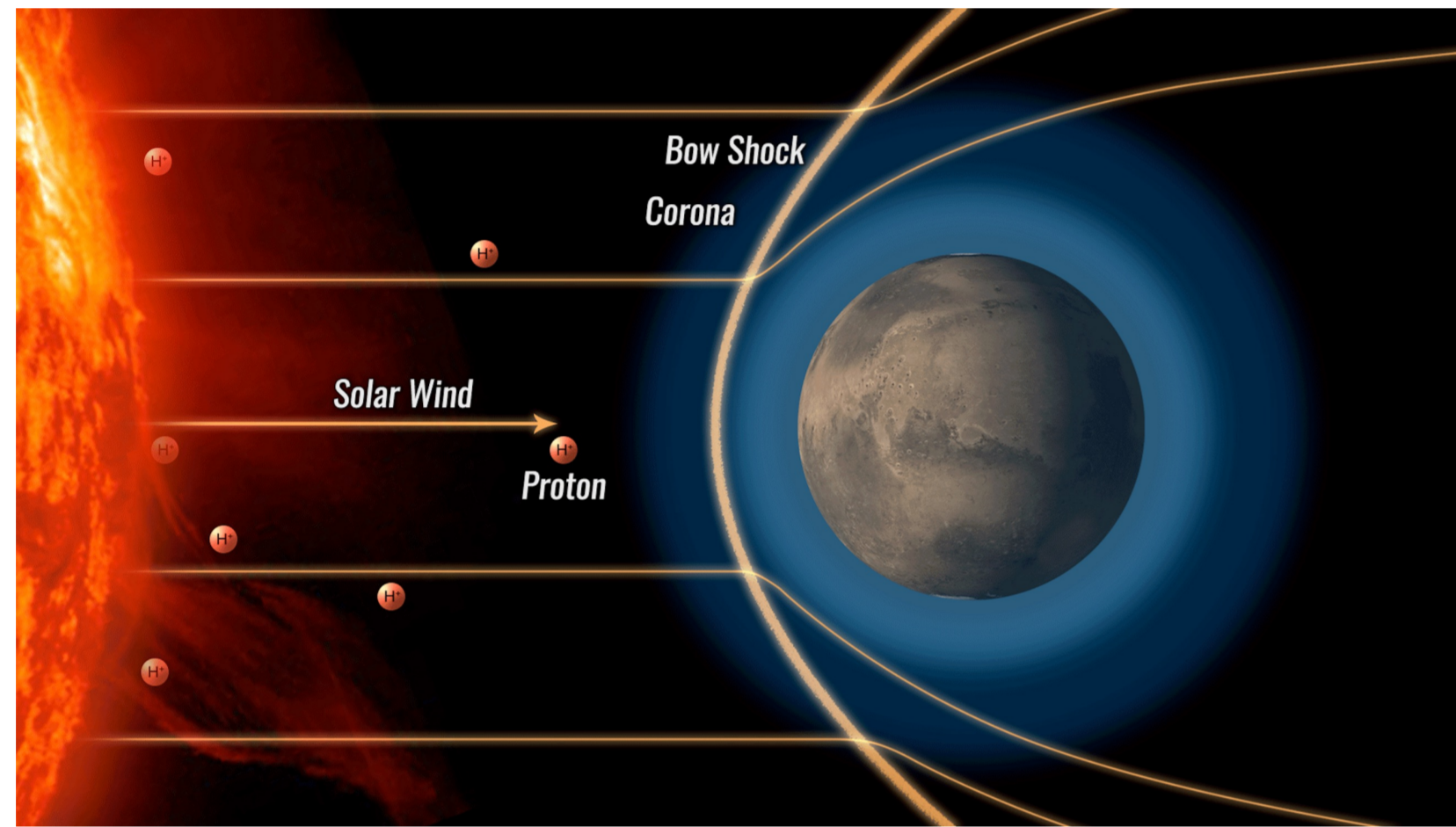
**Şekil 1.** Güneş rüzgarı ve Mars manyetosfer ile iyonosferinin gösterimi. *(science.nasa.gov)*

Mars Atmosferi ve Uçucu Evrim (MAVEN) uzay aracı, 16 Kasım 2014'ten bu yana , 150 km yükseklikte periapsis ve yaklaşık 6200 km yükseklikte apoapsis ile yaklaşık 4,5 saatlik bir yörüngede Mars'ın yörüngesinde döner ve güneş yumuşak X-ışınlarının ve EUV ışınımının değişkenliğini sürekli olarak gözlemlemektedir. MAVEN sürekli olarak yerel uzay havasını izlemektedir. MAVEN 'in cihaz takımından yapılan ilgili birçok gözlem arasında, Güneş Aşırı Ultraviyole Monitörü (EUVM) tarafından yapılan güneş ışınımı ölçümlerine dayanan güneş patlaması aktivitesi, Güneş enerjili parçacık (SEP) cihazından Güneş'te ve heliosferde yerel olarak hızlanan enerjik parçacıkların akışları, Güneş Rüzgarı İyon Analizörü (SWIA) tarafından güneş rüzgarı plazma parametreleri , Güneş Rüzgarı Elektron Analizörü (SWEA) ile elektronların ve iyonosferik fotoelektronların enerji ve açısal dağılımları ve Manyetometre (MAG) tarafından yapılan gezegenler arası manyetik alanın (IMF) vektör ölçümleri yer almaktadır [2].

10 EYLÜL 2017 CME'Sİ
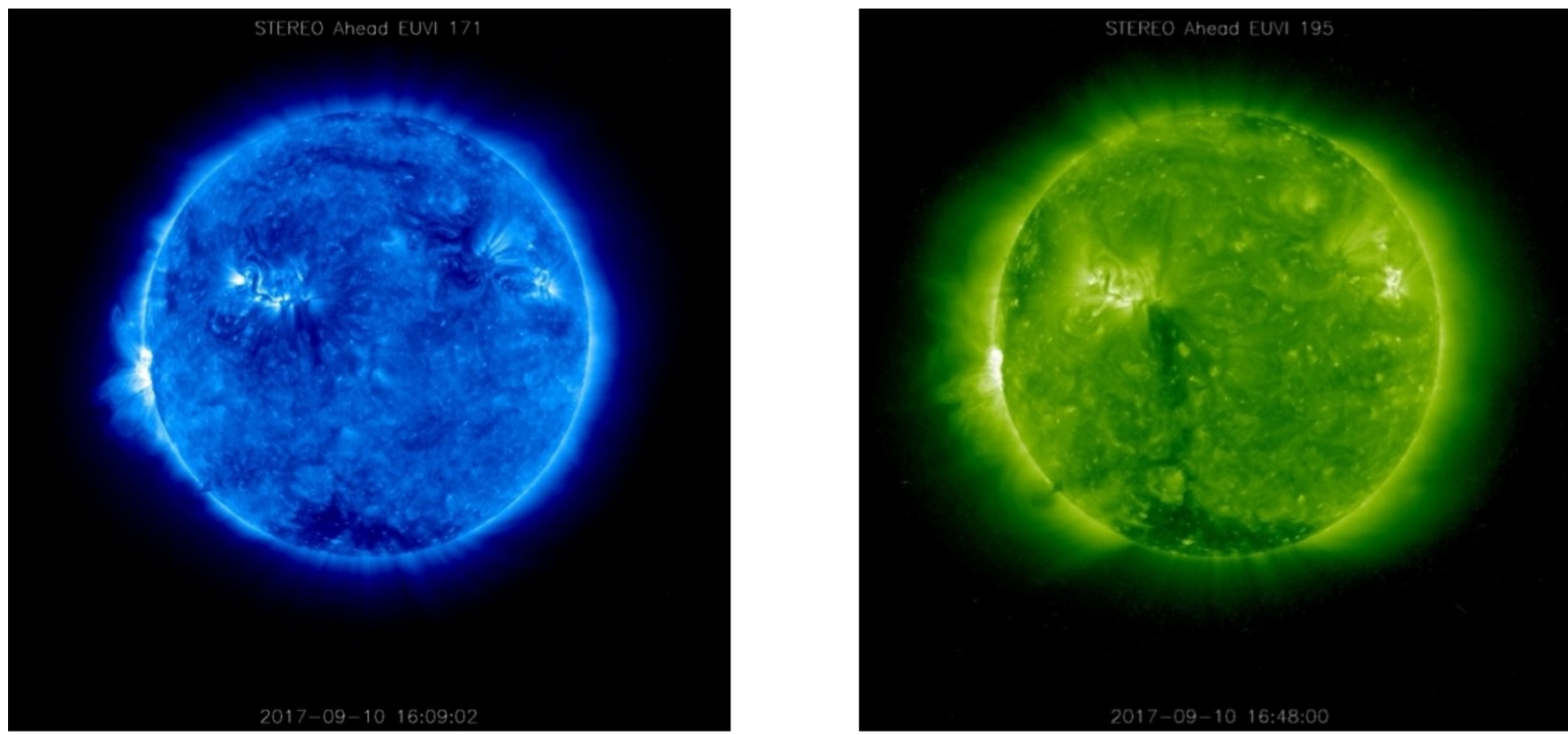
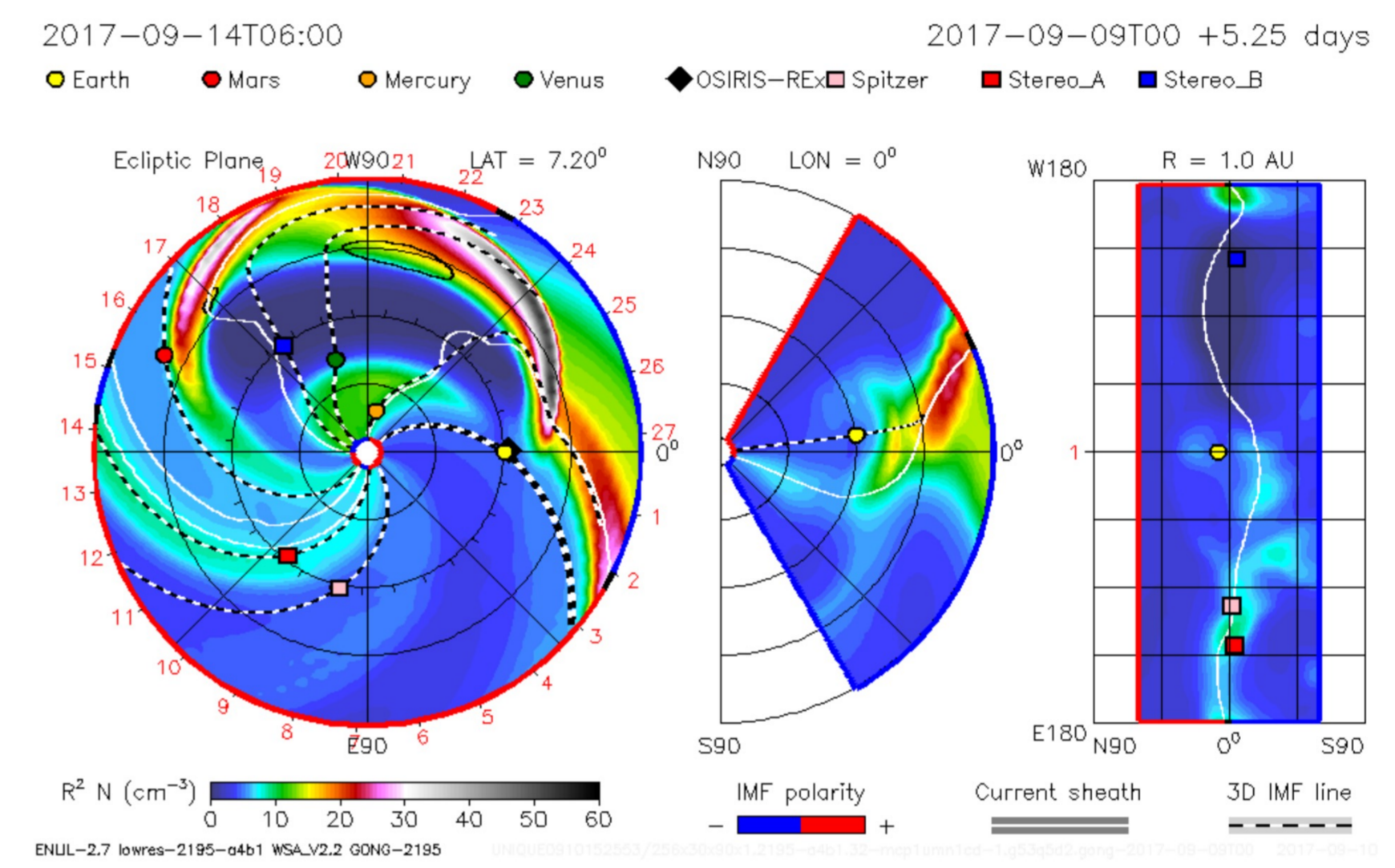**Şekil 2.** 10 Eylül 2017 CME'si (T16:09) sırasında alınmış STREO Güneş görüntüleri.

CDAW GÜNEŞ GÖRÜNTÜLERİ
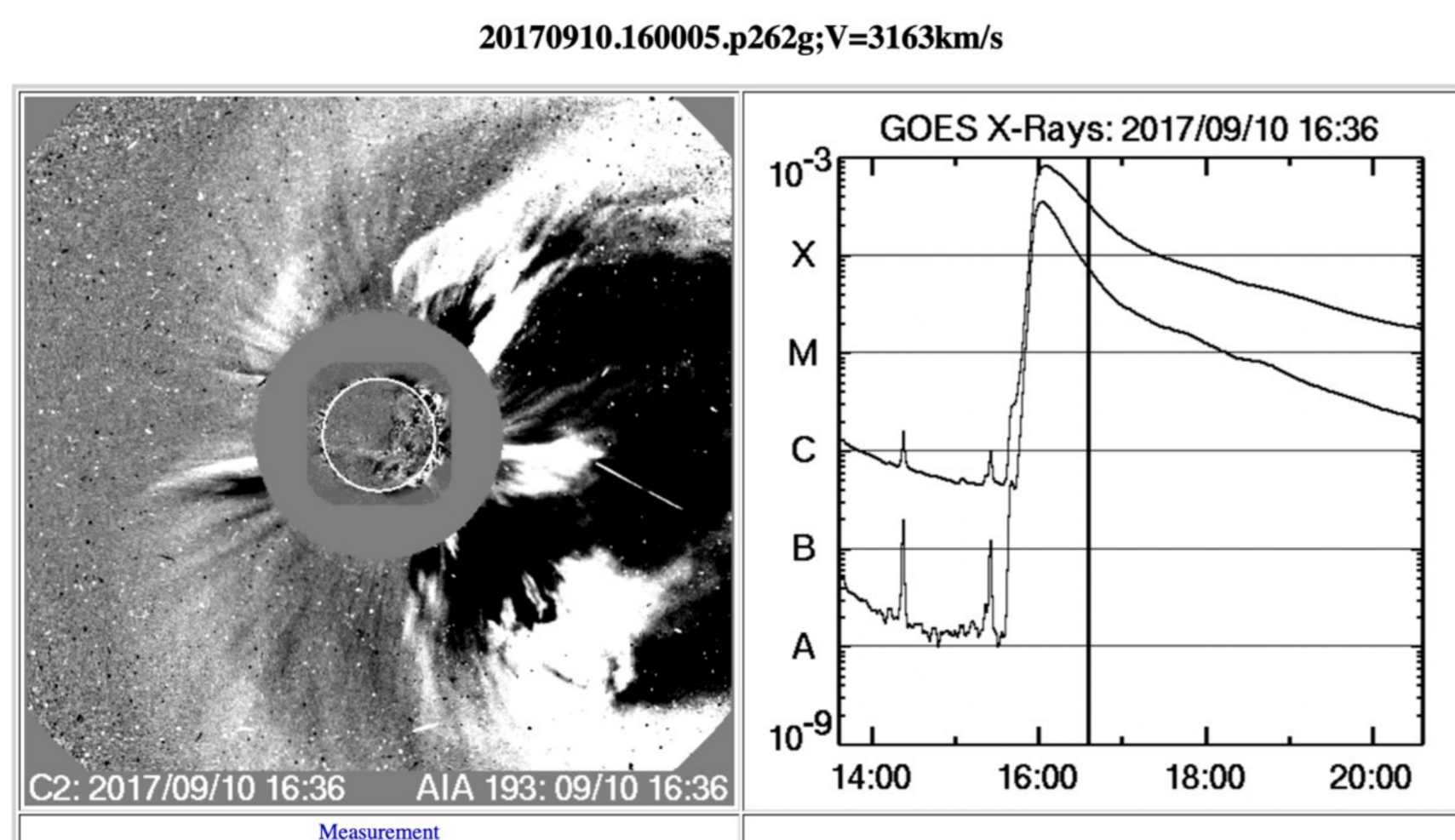
Şekil 3. CME atılım anının (10 Eylül 2017 ,16:36) Coordinated Data Analysis Workshops (CDAW) simülasyon ve X-Ray grafikleri.
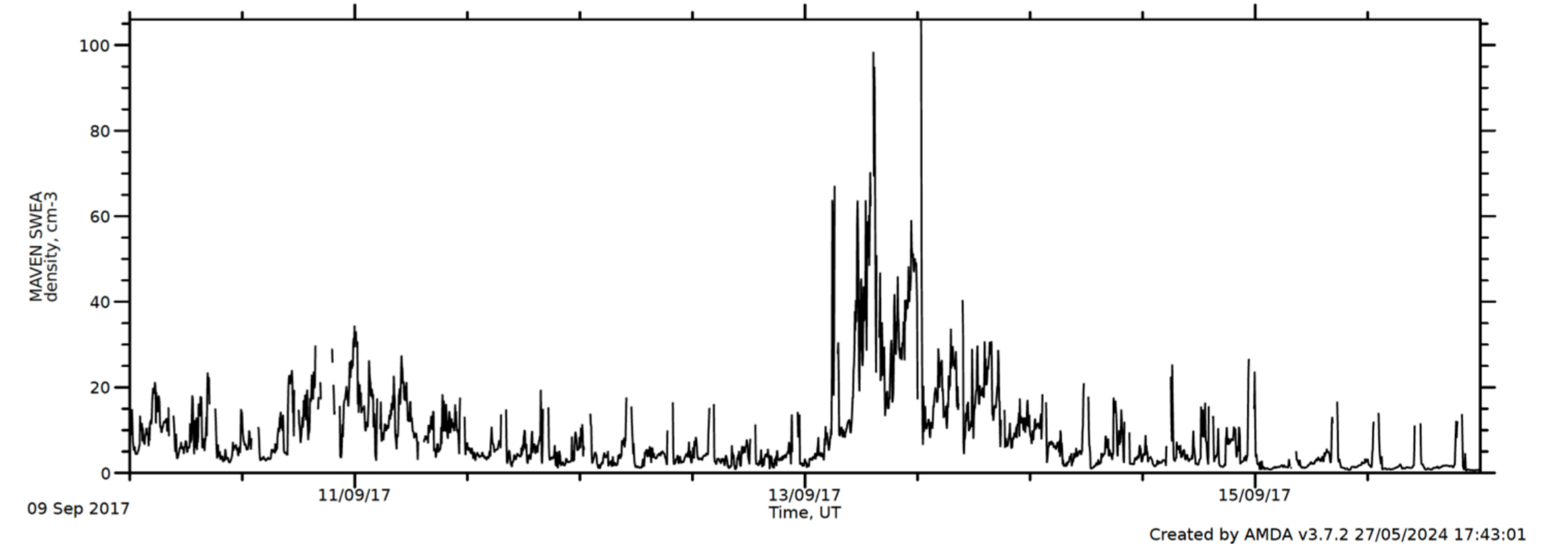
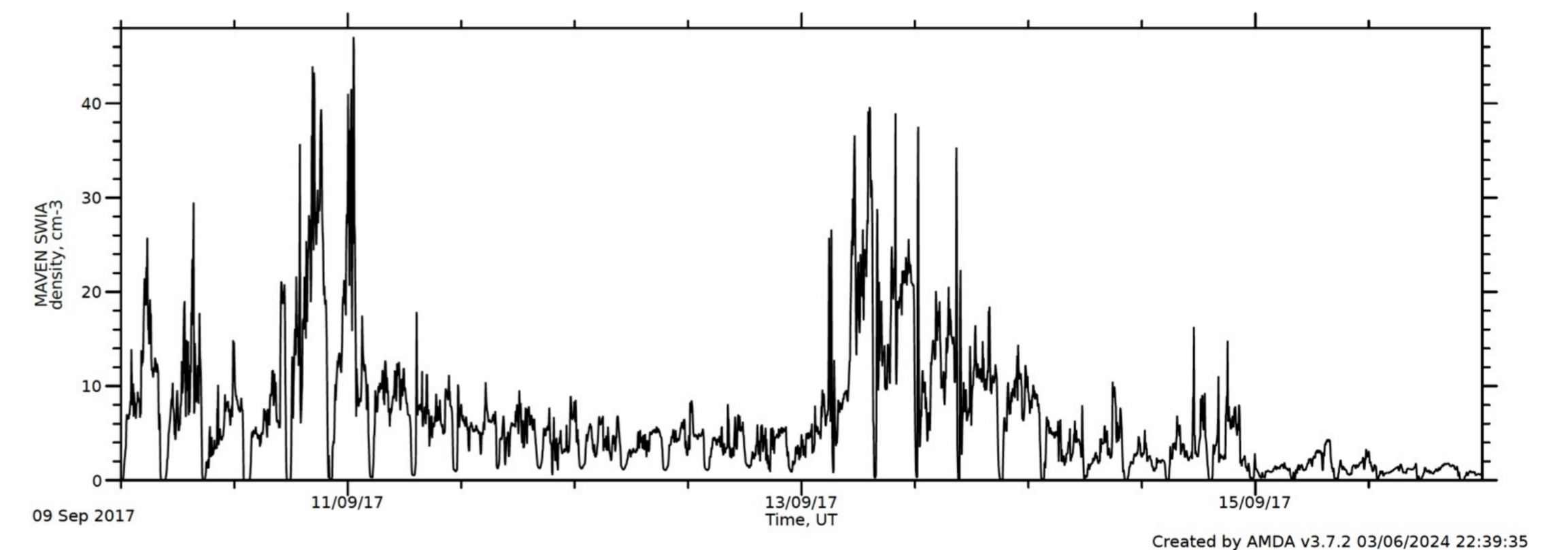## SONUÇ VE BULGULAR

WSA-ENLIL+Cone MODELİ

Şekil 4. Mars için şok varış zamanının gösterilmesi, 2017-09-14T10:00Z. (Wang-Sheeley-Arge (WSA)-Enlil görüntüsü)

MAVEN SWEA ve SWIA GRAFİKLERİ

Şekil 5. MAVEN uydusunun SWEA enstrümanının 2017-09-09 ile 2017-09-15 arasında, SWEA yoğunluk grafiği.

Şekil 6. MAVEN uydusunun SWIA enstrümanının 2017-09-09 ile 2017-09-15 arasında, SWIA yoğunluk grafiği.

10 Eylül 2017 tarihinde meydana gelen CME, 12 Eylül tarihinde Dünya'yı, 13 Eylül tarihinde ise Mars'ı etkilemesi açısından özel bir Güneş olayıdır. SWEA ve SWIA grafiklerinden anlaşıldığı üzere, Mars için, özellikle 13 Eylül ile 14 Eylül tarihlerinde, iki parametre için de göz ardı edilemez bir artış görülmüştür. MAVEN gibi uydulardan iyonsferdeki rahatsızlıkların araştırılması, Dünya'ya kıyasla çok daha ince bir yapısı olan Mars iyonosferini analiz etmek ve gelecekte yapılacak Mars misyonlarına katkı sağlamak için gereklidir.

KAYNAKÇA

[1] Brain, D.A., "The Response of the Martian Atmosphere to Space Weather," Space Weather of the Heliosphere: Processes and Forecasts, Proceedings IAU Symposium No. 335, 2017, C. Foullon & O.E. Malandraki, eds., doi:10.1017/S1743921317010924. [2]] Lee, C.O., et al., "MAVEN observations of the solar cycle 24 space weather conditions at Mars," Journal of Geophysical Research: Space Physics, vol. 122, 2017. doi:10.1002/2016JA023495. [3] Park, J., "Climatology of Martian ionospheric disturbances deduced from MAVEN data in 2014–2023," Journal of Geophysical Research: Space Physics, vol. 129, e2023JA031991, 2024. doi.org/10.1029/2023JA031991.

DEPARTMENT of PHYSICS

P-I-N TYPE PEROVSKITE SOLAR CELLS

Olcay Tekli 19022007
Prof. Dr. Serap Güneş

ABSTRACT

This study discusses the perovskite structure, its properties, the materials used in PSCs, and the production of PSCs. Additionally, a p-i-n type perovskite solar cell was fabricated using NiOx as the hole transport layer, PCBM as the electron transport layer, and methylammonium lead iodide ($CH_3NH_3PbI_3$) as the perovskite. The efficiency of the ITO/NiOx/ $CH_3NH_3PbI_3$/PCBM/Ag cell was found to be 16.5%, with a short circuit current density (Jsc) of 25 mA/cm², an open circuit voltage (Voc) of 1V, and a fill factor (FF) of 0.66

INTRODUCTION

Today, silicon solar cells dominate the PV market. Due to the high cost and difficult production processes of these cells, research on solar cells that will be alternatives to silicon-based solar cells continues. Emerging PV Technologies such as organic, dye sensitized, hybrid and perovskite solar cells have been investigated as alternatives. Recently, due to high power conversion efficiencies perovskite solar cells have been put forward. Also, they are lighter and less expensive than silicon-based solar cells. Recent studies have shown that organic-inorganic perovskite solar cells are promising in solar energy production. Over time, interest in perovskite solar cells increased, accelerating advancements. Using different perovskite structures, efficiencies continued to improve, and recent studies have reported efficiencies exceeding 25%.[1-3].

Figure 1. Perovskite solar cells after thermal evaporation

EXPERIMENTAL DETAILS

NiOx solution was prepared by dissolving 248 mg of nickel (II) acetate tetrahydrate in 10 ml of ethanol and 60 μl of a diethanolamine mixture. The resulting mixture was subsequently stirred for one hour at 70 °C. Before coating, the NiOx precursor was prepared at ambient atmosphere and filtered via a 0.45 μm PVDF filter. Perovskite solution was prepared by dissolving 645,4 mg of PbI2 and 222,5 mg of CH_3NH_3I in 1 ml GBL (γ-butyrolactone) at 60˚C for at least 12 hours. A 0.45 μm PVDF filter was employed to filter the precursor before the perovskite deposition process. 20 mg of PCBM material was introduced in 1 ml of a 1:1 volume ratio mixture of chlorobenzene and dichlorobenzene, and the mixture was stirred at 40˚C for several hours to yield the PCBM solution. The BCP solution was formed by dissolving 0,5 mg/ml of BCP powder in pure ethanol.

For device preparation, ITO substrate was cut down to 1,5 cm × 1,5 cm pieces and properly cleaned in acetone and isopropanol bath for 20 and 45 minutes, respectively. Drying the substrates with N2 gas is carried out before placing them on the hot plate at 120˚C for three minutes. The spin coating technique was applied while they had reached room temperature. All of the temperatures were monitored using an infrared thermometer. The perovskite solution was coated for 10 and 20 seconds at 2000 and 4000 rpm, respectively. While the second spinning step lasted for five seconds, 100 μl of toluene was dropped onto the rotating substrate. The resulting film was then heated up at 100°C for 20 minutes at ambient air. PCBM layer was obtained by coating the PCBM mixture at 1500 rpm for 15 seconds and 2000 rpm for 20 seconds, then thermal annealing followed at 90˚C for 2 min. The BCP layer, which is utilized as a buffer and hole-blocking layer was cast at 4000 rpm for 45 seconds. Finally, all of the obtained samples were transferred to a high vacuum thermal evaporation machine at 10-5 torr to get 110 nm of Ag electrodes. All production processes were carried out outside of a glove box with 40–60% humidity

Power conversion efficiency (PCE) of solar cells were calculated using the formula below.

$$\eta(\%) = \frac{J_{sc} * V_{oc} * FF}{P_{in}} X \, 100$$

Where J_{sc} is the short circuit current density, V_{oc} is the open circuit voltage and FF is the fill factor and the P_{in} is the intensity of incident light.
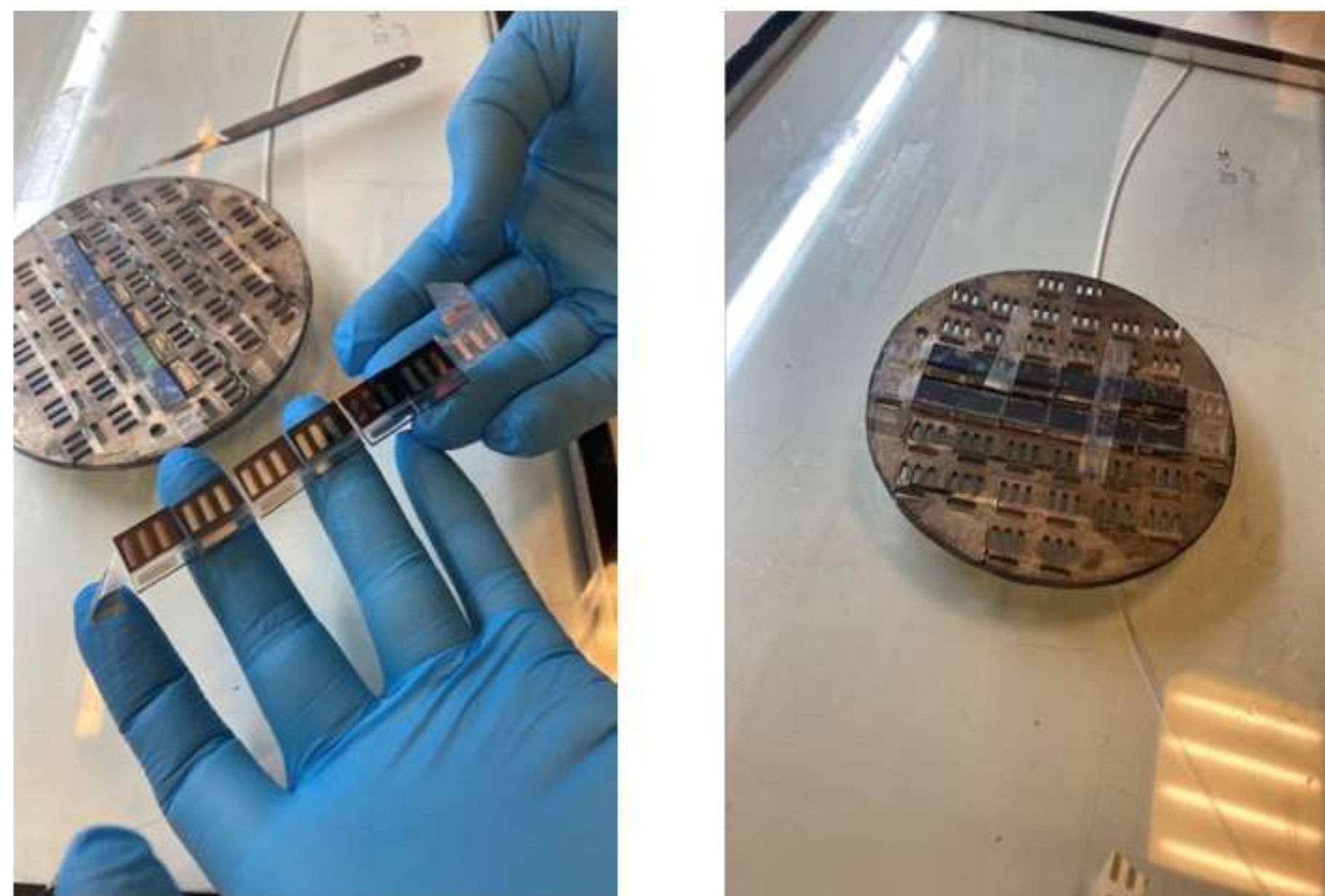

Figure 2. Solar simulator

As described in the experimental section we have fabricated p-i-n type perovskite solar cells using NiO_x as HTL, $CH_3NH_3PbI_3$ as perovskite layer and PCBM as ETL Ag was used as top metal contact. The main advantage of such a cell is their operational stability, low temperature processability and compatibility of them with silicon solar cells in the tandem form. Stability is also better controlled.

RESULTS

Figure 3 shows the current density-voltage (J-V) curve of herein investigated perovskite solar cells. As can be analyzed from the J-V curve such a cell produced a short circuit current density (Jsc) of 25 mA/cm2 and an open circuit voltage (Voc) of 1 V and a fill factor (FF) of 0.66 was calculated, which led to a power conversion efficiency of 16.5 %.

REFERENCES

1. Cao, F., Bian, L.,Li, L. (2024). «Perovskite solar cells with high-efficiency exceeding 25%: A review», Energy Materials and Devices, 2024, 2(1): 9370018. https://doi.org/10.26599/EMD.2024.9370018
2. Chen, J., Dong, H., Li, J., Zhu, X., Xu., J., Pan, F., Xu, R., Xi, J., Hou, X., Kar Eeri, N.G., Shuang-Peng, W., Wu, Z. (2022). «Solar cell efficiemcy exceeding 25 % 25% through Rb-Based Perovskitoid Scaffold Stabilizing the Buried Perovskite Surface», ACS Energy Lett. 2022, 7, 10, 3685–3694, https://doi.org/10.1021/acsenergylett.2c01661
3. Kim, G.H., Kim, D.S. (2021). «Development of perovskite solar cells with >25% conversion efficiency», Joule,5, 1033-1035, https://doi.org/10.1016/j.joule.2021.04.008

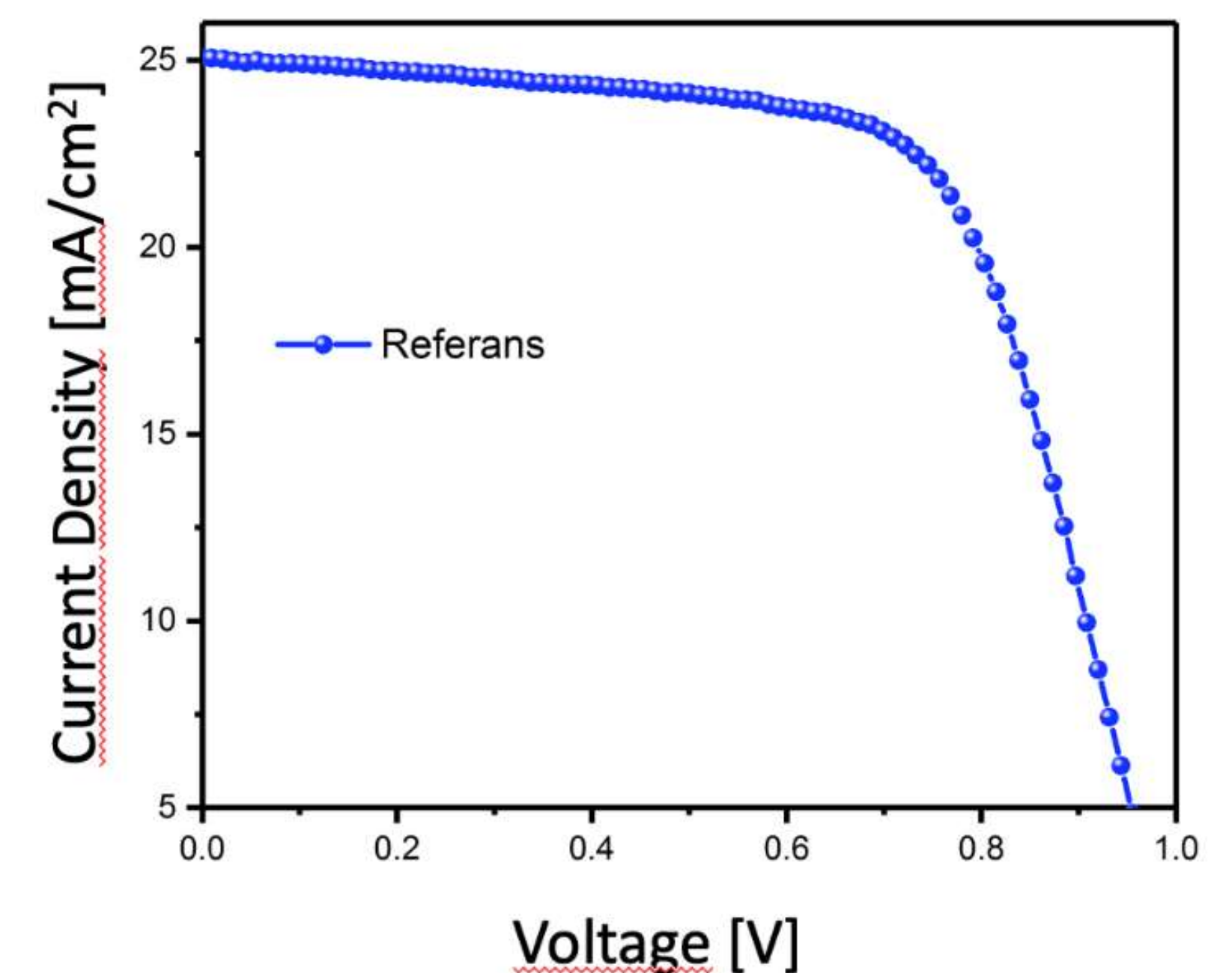Figure 3 shows the current density-voltage (J-V) graphs of p-i-n type perovskite solar cells

Figure 3. J-V characteristics of p-i-n type perovskite solar cell

One of the most important achievement in this study is that perovskite solar cells are fabricated under ambient conditions. They were taken into glovebox, which is shown in figure 4 for characterization under solar simulator.
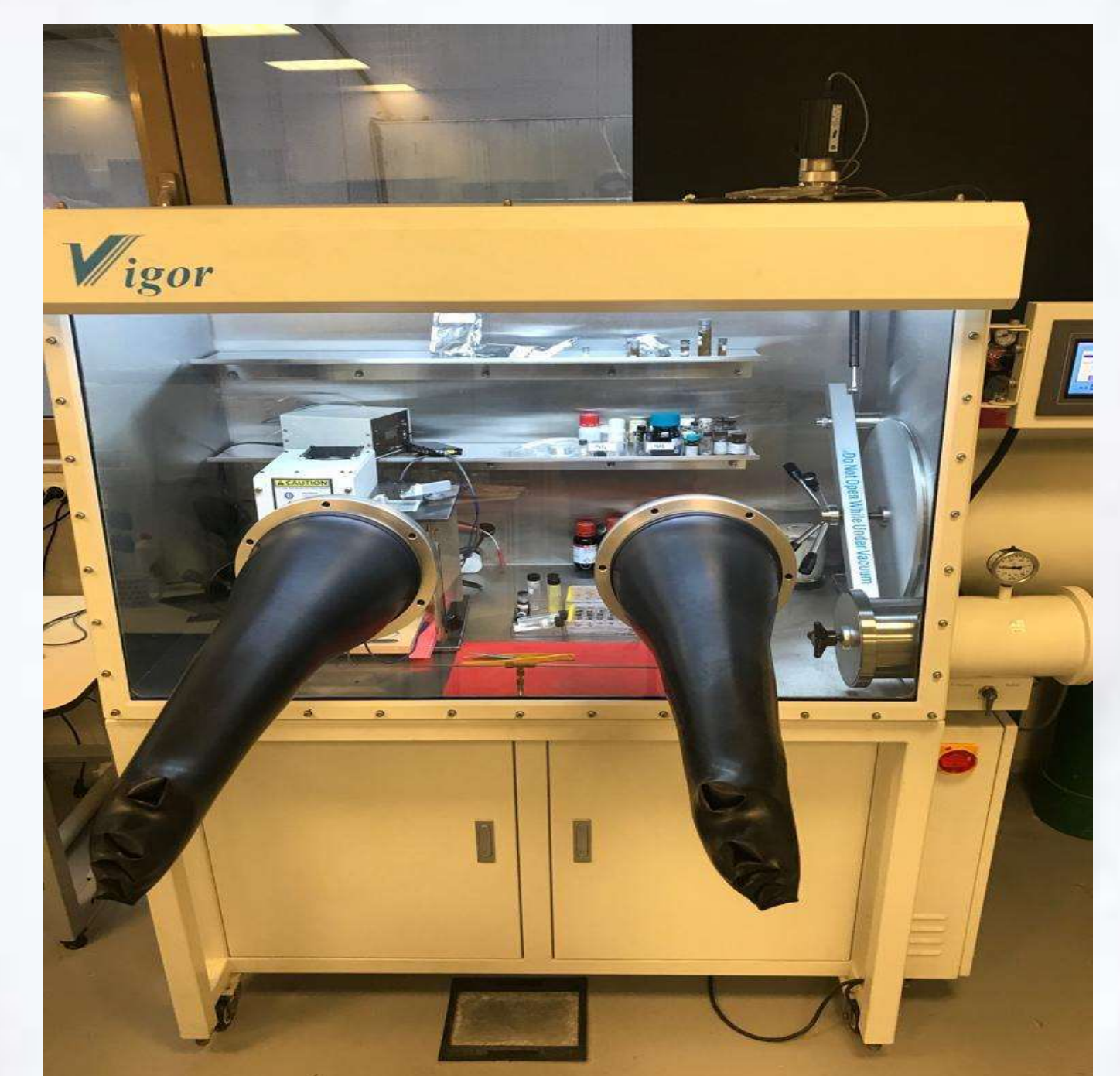

Figure 4. Glovebox

CONCLUSION

This study confirms that p-i-n perovskite solar cells may be a viable and efficient alternative to conventional solar cells especially for indoor applications. Future research should focus on improving the stability and scalability of these cells to facilitate their commercial application. Continued advancements in material selection and device architecture are anticipated to further enhance the efficiency and durability of perovskite solar cells, positioning them as a pivotal component in the pursuit of sustainable and clean energy solutions

Acknowledgement

YTÜ FEN EDEBİYAT FAKÜLTESİ

2023-2024 Bahar Yarıyılı Fizik BÖLÜMÜ

INCREASING THE EFFICIENCY OF ORGANIC PHOTOVOLTAIC CELLS WITH ACOUSTIC EFFECT

Ceren YAYGIN - 19022008

Prof. Dr. Serap Güneş

ABSTRACT

This study discusses the perovskite structure, its properties, the materials used in PSCs, and the production of PSCs. Additionally, a p-i-n type perovskite solar cell was fabricated using NiOx as the hole transport layer, PCBM as the electron transport layer, and methylammonium lead iodide (CH3NH3PbI3) as the perovskite. The efficiency of the ITO/NiOx/CH3NH3PbI3/PCBM/Ag cell was found to be 16.5%, with a short circuit current density (Jsc) of 25 mA/cm², an open circuit voltage (Voc) of 1V, and a fill factor (FF) of 0.66

INTRODUCTION

In this study, inverted type organic solar cells were fabricated and were divided into three groups. While one group was kept in a quiet environment, the effect of fixed frequencies was studied in the other two groups. Second group was also divided into two groups. The first group was exposed to a fixed frequency of 200 Hz, while the second group was exposed to a fixed frequency of 800 Hz. For the third group, the effect of music was examined. For this reason, the song "Get Back" by The Beatles was chosen. All samples were exposed to sound for 15 minutes. With this study, it is aimed to contribute to the integration of photovoltaic cells, which are increasingly being used and developed for a cleaner and more sustainable world, into new technologies by increasing their efficiency with simple and natural effects that can be frequently and easily encountered in the environmental environment.

EXPERIMENTAL DETAILS

Initially, all ITO-coated glass substrates were patterned by etching with an acid mixture of HCl:HNO3:H2O (4.6:0.4:5) for 40 min. After etching, glass substrates were cleaned in ultrasonic bath with acetone and isopropanol at each stage for 20 min, respectively. The mixture is stirred for 15 minutes and then 1 g of mixture is diluted with 10 g of ethanol. The diluted solution is spin cast on precleaned ITO substrates at 8000 rpm. Then the TiOx films were annealed at 450 oC for 30 minutes. 12 mg P3HT and 6.5 mg PCBM were blended in chlorobenzene. The solution was spin cast on TiOx coated substrates at 4000 rpm. And finally 100 nm Ag electrodes were thermally evaporated.

The current density-voltage curves of the devices were obtained using a computer-controlled Keithley 2400 source meter with a scan rate of 0.025 Vs-1 and 0.03 s delay time(Figure:8). Photocurrent density-voltage performances were recorded under 100mW/cm2 illumination (AM 1.5G), using a Abet solar simulator, which was calibrated using a silicon diode from Oriel.

Power conversion efficiency (PCE) of solar cells were calculated using the formula below.

$$\eta(\%) = \frac{J_{sc} * V_{oc} * FF}{P_{in}} X 100$$

Where Jsc is the short circuit current density, Voc is the open circuit voltage and FF is the fill factor and the Pin is the intensity of incident light.

Figure 1. Spin coater

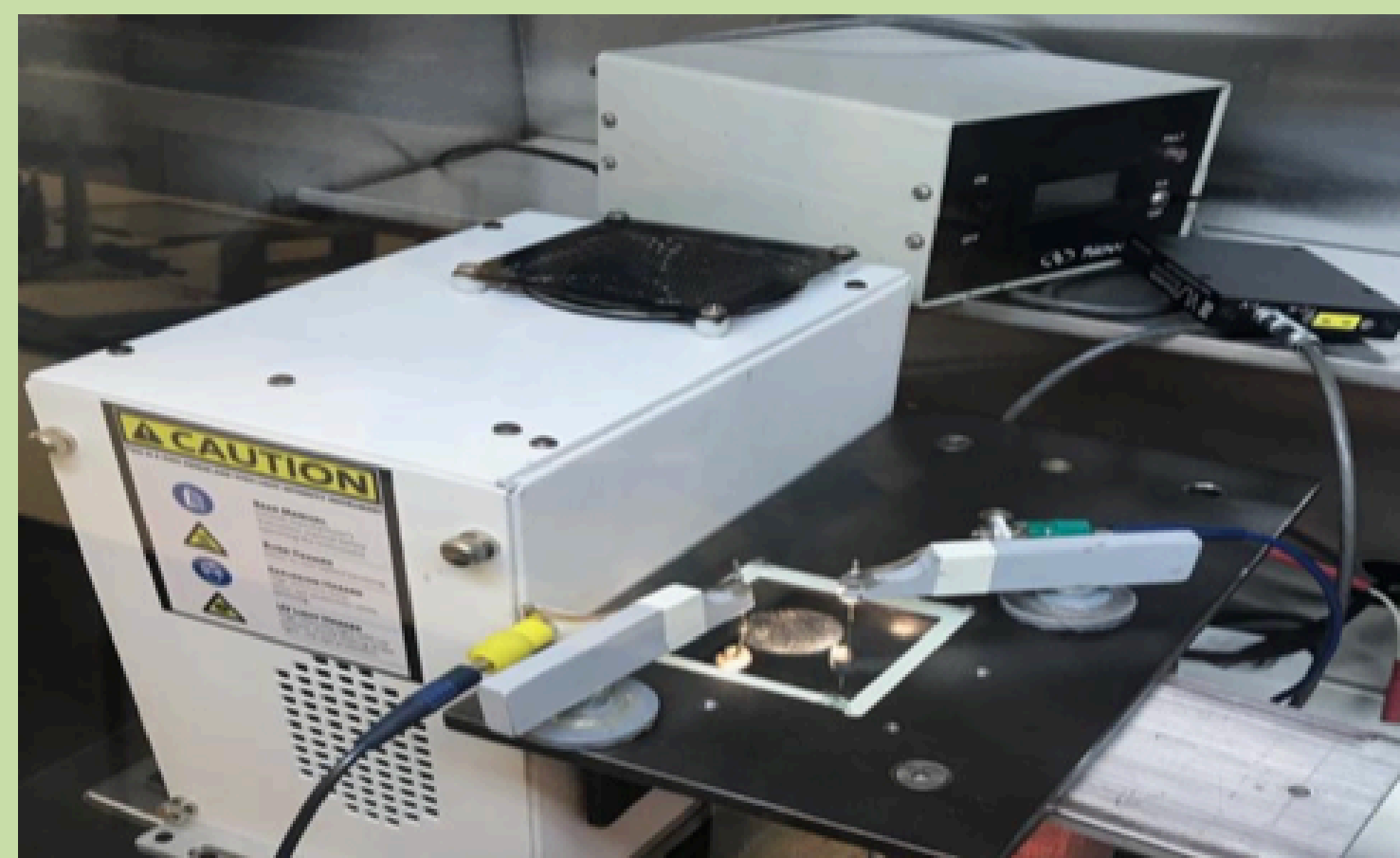|	Acoustic Effect	Group Number	Active Area (cm)	Efficiency (Before Acoustic Effect)	Efficiency (After Acoustic Effect)
Music - The Beatles "Get Back"	Different Frequencies	1	0.074	%0.35	%0.68
200 Hz	200 Hz Fixed Low-Mixed Frequency	2	0.066	%0.32	%0.48
800 Hz	800 Hz Fixed Bass Frequency	3	0.062	%0.37	%0.55

Figure 2. Summary of PV results

Figure 3. Solar simulator

RESULTS

Figure 4 shows the current density-voltage (J-V) curve of the cells exposed to Music-The Beatles. As can be analyzed from the J-V curve such a cell exhibited a PCE of 0.68 %. The efficiency of reference device was 0.35 %. There was an increase of 94 % in the performance after exposure to music
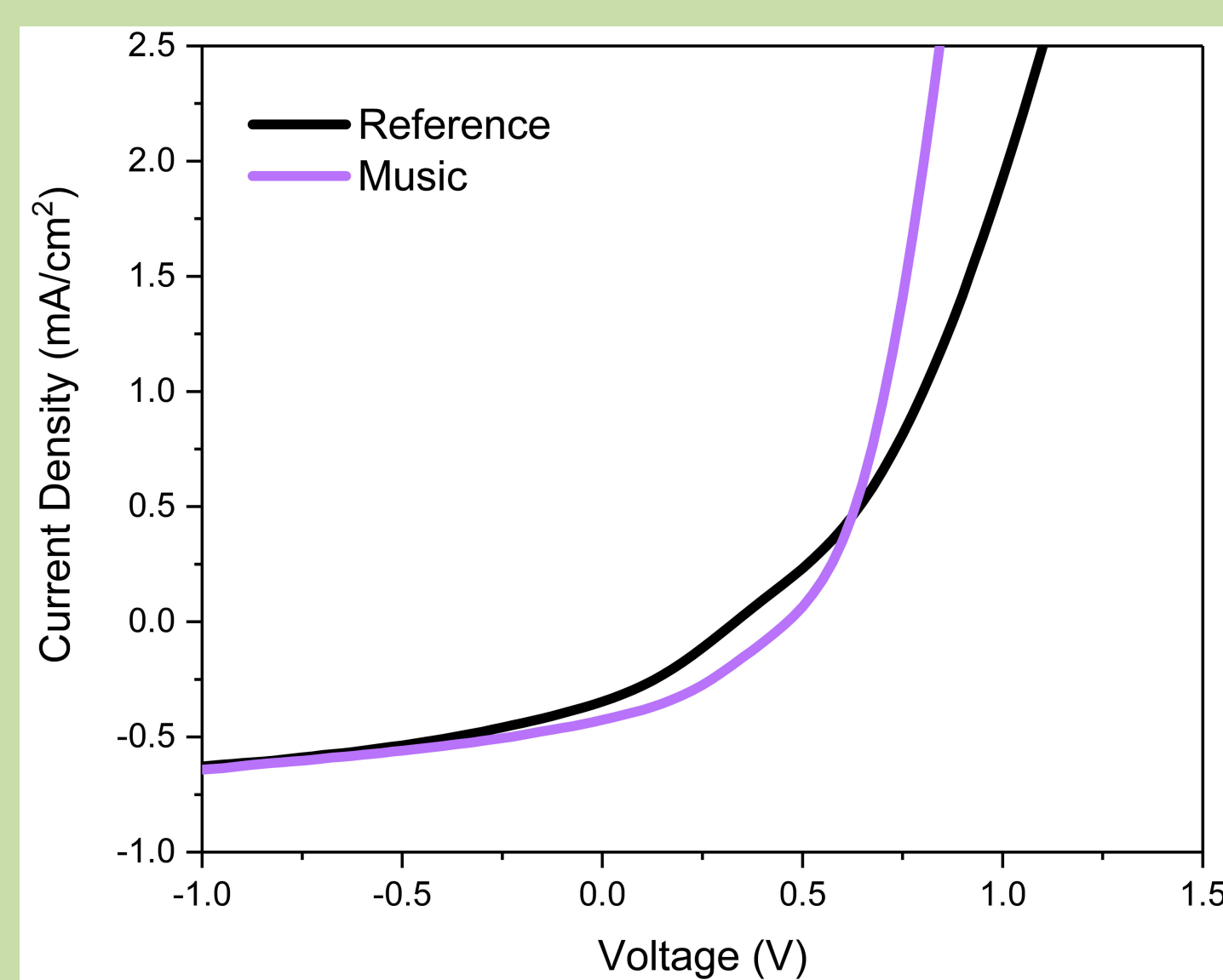

Figure 4. J-V curve of the reference and inverted type organic solar cells exposed to The Beatles

ACKNOWLEDGEMENT

REFERENCES

[1] Shoaee, S., Briscoe, J., Durrant, J.R., Dunn, D. (2014). «Acoustic Enhancement of Polymer/ZnO Nanorod Photovoltaic Device Performance», 10.1002/adma.201303304
[2] Chen, L. (2019). «Organic Solar Cells: Recent Progress and Challenges», ACS Energy Lett. 2019,4,10,2537–2539, https://doi.org/10.1021/acsenergylett.9b02071
[3] Wu, J., Gao, M., Chai, Y., Liu, P., Zhang, B., Liu, J., Ye, L. (2021). «Towards a bright future: The versatile applications of organic solar cells» , Materials Reports: Energy, 1, 100062

Figure 5 shows the current density-voltage (J-V) graph of the device exposed to 200 Hz. As can be seen such a cell exhibited a PCE of 0.48 % and there was an increase of 50 % in the performance upon exposure to 200 Hz.
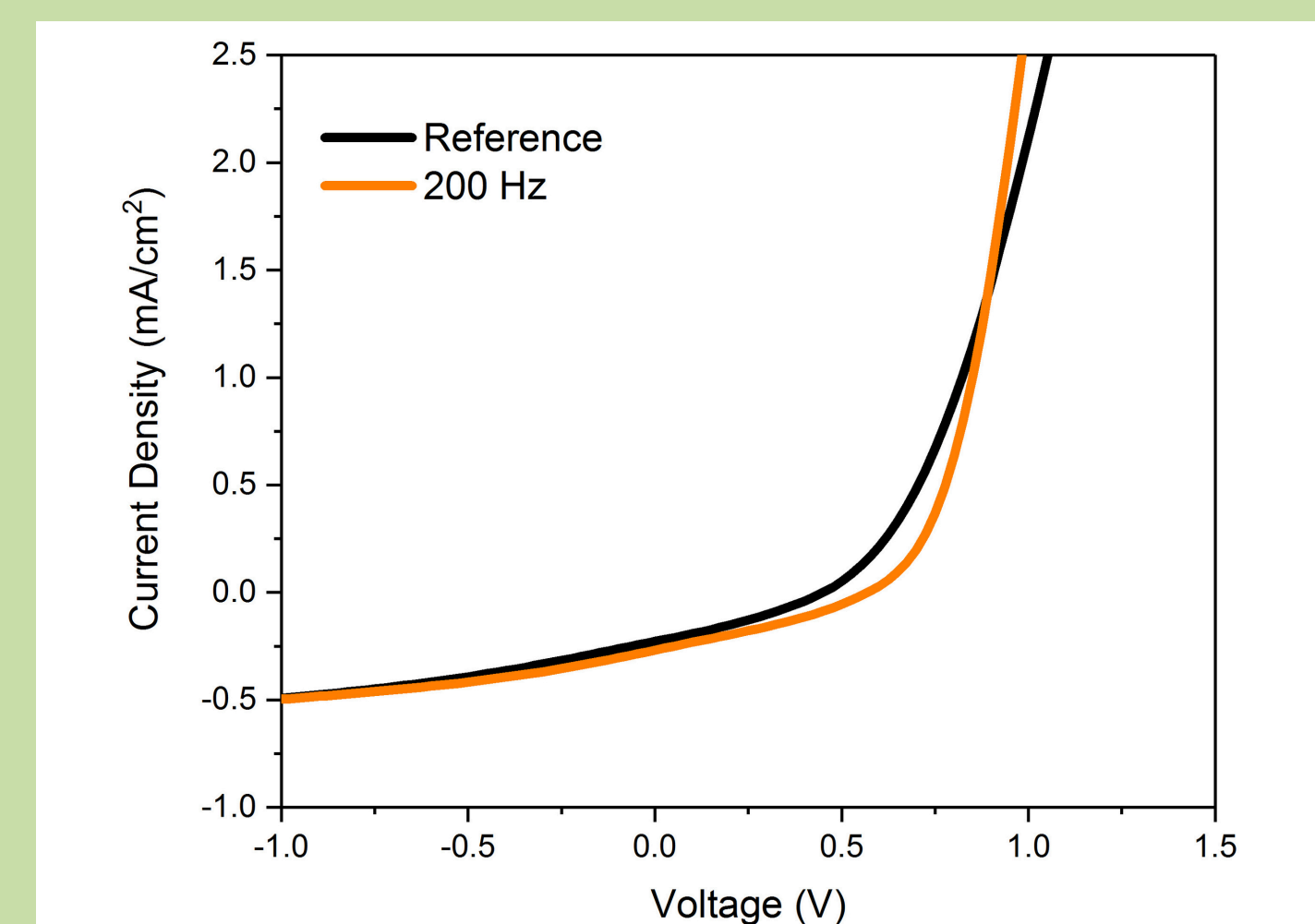

Figure 5. J-V curve of the device exposed to a fixed frequency of 200 Hz

Figure 6 shows the current density-voltage (J-V) graph of the device exposed to 800 Hz. As can be seen such a cell exhibited a PCE of 0.55 % and there was an increase of 49 % in the performance upon exposure to 800 Hz.
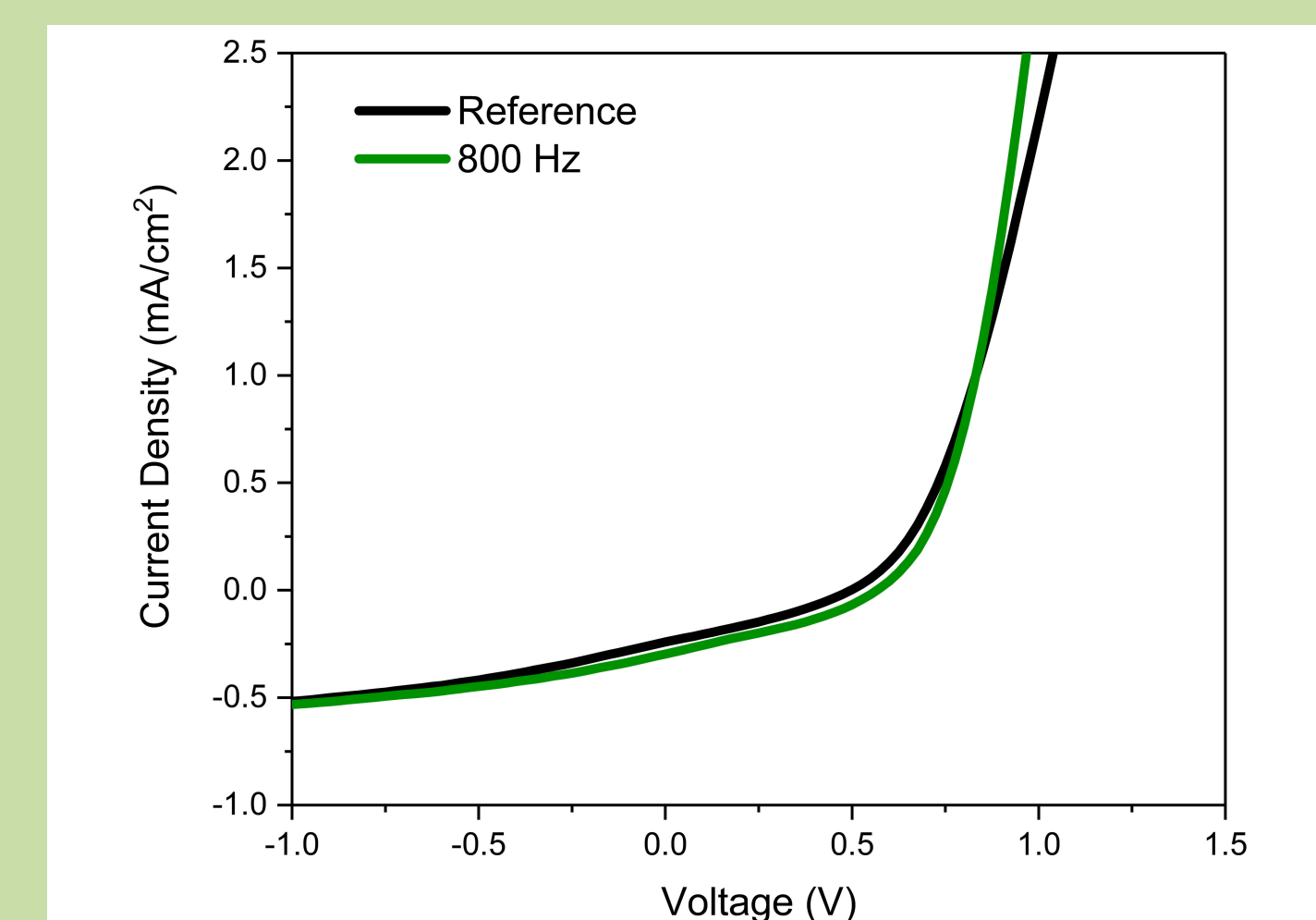

Figure 6. J-V characteristics of the devices exposed to a fixed frequency of 800 Hz.

CONCLUSION

The devices were analyzed under three conditions: bass frequency, mid-lower frequency, and music. Bass and lower-mid frequencies are given as fixed frequencies. The reason for choosing music is to analyze the effect of applying different frequencies simultaneously on the device. The fixed frequency of 800 Hz sent as bass frequency increased the efficiency of the device by 49%. This rate is quite high. It makes it possible to say that the efficiency of the device increases with the acoustic effect.

A fixed frequency of 200 Hz as a mid-lower frequency sent to the other device increased the efficiency of the cell by 50%. As can be seen, this is slightly higher than the bass frequency.

Music was played to the last device. Because music is formed by the simultaneous vibration of different frequencies. While choosing the music here, a classic rock song was requested. For this reason, The Beatles' "Get Back" was chosen. In future studies, the effects of music on device efficiency can be examined in more detail by diversifying music types.